SINGLE PLATFORM GEOLOCATION OF RADIO FREQUENCY EMITTERS

THESIS

Eric J. Bailey, Captain, USAF

AFIT-ENG-MS-15-M-028

DEPARTMENT OF THE AIR FORCE
AIR UNIVERSITY

AIR FORCE INSTITUTE OF TECHNOLOGY

Wright-Patterson Air Force Base, Ohio

AFIT-ENG-MS-15-M-028

SINGLE PLATFORM GEOLOCATION OF RADIO FREQUENCY EMITTERS

THESIS

Presented to the Faculty

Department of Electrical and Computer Engineering

Graduate School of Engineering and Management

Air Force Institute of Technology

Air University

Air Education and Training Command

in Partial Fulfillment of the Requirements for the

Degree of Master of Science in Electrical Engineering

Eric J. Bailey, B.S.A.E.

Captain, USAF

March 2015

AFIT-ENG-MS-15-M-028

SINGLE PLATFORM GEOLOCATION OF RADIO FREQUENCY EMITTERS

Eric J. Bailey, B.S.A.E.
Captain, USAF

Committee Membership:

Richard K. Martin, PhD
Chair

Marshall E. Haker, PhD
Member

Eric D. Swenson, PhD
Member

AFIT-ENG-MS-15-M-028

Abstract

The focus of this research is on single platform geolocation methods where the position of a single stationary radio frequency emitter is estimated from multiple simulated angle and frequency of arrival measurements taken from a single moving receiver platform. The analysis scenario considered consists of a single 6U CubeSat in low earth orbit receiving radio frequency signals from a stationary emitter located on the surface of the Earth. A multiple element receive antenna array and the multiple signal classification algorithm are used to estimate the angles of arrival of an impinging signal. The maximum likelihood estimator is used to estimate the frequency of arrival of the received signal. Four geolocation algorithms are developed and the accuracy performance is compared to the Cramer-Rao lower bounds through Monte Carlo simulations. Results from a system parameter sensitivity analysis show the combined angle and frequency of arrival geolocation maximum likelihood estimator consistently outperforms the other three geolocation algorithms.

Table of Contents

List of Figures

List of Tables

List of Notation

Notation	Definition
$[\bullet]^T$	matrix transpose
$[\bullet]^H$	matrix Hermitian (complex conjugate) transpose
$\det(\bullet)$	matrix determinate
$\|\bullet\|$	vector norm
$\mathrm{trace}\{\bullet\}$	matrix trace
$\mathrm{diag}\,[\bullet]$	diagonal matrix
$\mathbf{I}$	identity matrix
$\mathbf{0}$	zero matrix
$[\bullet]_{i,j}$	matrix element i, j
$[\bullet]_{R \times C}$	matrix size in number of rows R by columns C
$\sim$	distributed
$\overset{a}{\sim}$	asymptotically distributed
$\Pr\{\bullet\}$	probability
$E\,[\bullet]$	expected value
$\mathrm{var}\,(\bullet)$	variance
$\mathrm{cov}\,(\bullet)$	covariance
$\mathrm{CRLB}\,(\bullet)$	Cramer-Rao lower bound
$|\bullet|$	absolute value
$\mathrm{Re}\,\{\bullet\}$	real part
$\mathrm{Im}\,\{\bullet\}$	imaginary part
$\mathrm{atan2}\,(\bullet)$	arctangent function with two arguments
$\arg\min\,(\bullet)$	argument of the minimum
$\arg\max\,(\bullet)$	argument of the maximum

Notation	Definition
DFT $[\bullet]$	discrete Fourier transform
∇	gradient
$\dot{\bullet}$	derivative with respect to time
$\hat{\bullet}$	estimate
$\varnothing$	diameter

List of Acronyms

Acronym	Definition
6U	6 Unit
ADCS	Attitude Determination and Control System
AOA	Angle of Arrival
AWGN	Additive White Gaussian Noise
CDF	Cumulative Distribution Function
CRLB	Cramér-Rao Lower Bound
DCM	Direction Cosine Matrix
DFT	Discrete Fourier Transform
ECEF	Earth Centered Earth Fixed
EIRP	Effective Isotropic Radiated Power
EM	Electromagnetic
ENU	East North Up
FIM	Fisher Information Matrix
FOA	Frequency of Arrival
GNC	Guidance Navigation and Control
GPS	Global Positioning System
LEO	Low Earth Orbit
LOB	Line of Bearing
LS	Least Squares
LVLH	Local Vertical Local Horizontal
MCS	Monte Carlo Simulation
MLE	Maximum Likelihood Estimate
MUSIC	Multiple Signal Classification

Acronym	Definition
NLO	Non-Linear Optimization
PDF	Probability Density Function
RF	Radio Frequency
RMSE	Root Mean Square Error
SNR	Signal to Noise Ratio
SOI	Signal of Interest
STK	Systems Tool Kit
UCA	Uniform Circular Array
WGS	World Geodetic System

SINGLE PLATFORM GEOLOCATION OF RADIO FREQUENCY EMITTERS

I.   Introduction

Geolocation of Radio Frequency (RF) emitters involves estimating the position of an emitter from the received RF signals at one or more receivers. In the case of passive geolocation [1], only the phenomenology of the received signals (angle of arrival, time delay, Doppler frequency shift, etc.) is used to estimate the position of the RF emitter, rather than the emitter providing its position as a message contained in the RF signal. Geolocation methods involving multiple coordinated RF receivers include: Angle of Arrival (AOA) [2], time difference of arrival [3], frequency difference of arrival [1], and direct position determination [4]. Geolocation methods using a single moving receiver include AOA [3] and Frequency of Arrival (FOA) [5]. The focus of this thesis research is the single moving platform geolocation methods available to estimate the position of a single stationary RF emitter using multiple angle and frequency measurements from the received RF signals.

1.1   Problem Statement and Research Objective

The scenario considered in this research is to geolocate a single stationary RF emitter using the signals received by an antenna array on a single 6 Unit (6U) CubeSat [6] moving in Low Earth Orbit (LEO). The goal of this research is to develop, implement, analyze, and compare single platform geolocation algorithms. A simulation framework is developed to conduct a system parameter sensitivity analysis to assess parameter impact on the performance of the geolocation algorithms.

1

1.2   Underlying Assumptions

The following underlying assumptions apply to the scope of the research. The single moving 6U CubeSat consists of a calibrated multiple element antenna array, phase coherent RF receivers, and a guidance, navigation, and control subsystem to provide position, velocity, and attitude data to a dedicated payload processor. A 6U CubeSat is defined [6] with the exterior dimensions of 12 x 24 x 36 cm and a total mass less than 12 kg. The single terrestrial RF emitter is assumed to be stationary with no co-channel interference from multiple emitters. The following topics are beyond the scope of this thesis and are left as considerations for future research: implementation of specific antenna arrays, RF emitters, and RF receivers; filtering and pre-processing of the received RF signals; multiple emitter segregation through data association of the received RF signals; and the effect of co-channel interference on geolocation algorithm performance.

1.3   Thesis Organization

This thesis is organized as follows: Chapter II discusses existing angle of arrival geolocation algorithms and signal parameter estimation methods; Chapter III develops the geolocation algorithms and simulations used in this thesis; Chapter IV reports the results of a system parameter sensitivity analysis to assess the impact on the performance of the various geolocation algorithms; and Chapter V presents the overall conclusions of this research with recommendations for future work.

II. Background

This chapter is organized as follows: Section 2.1 describes the coordinate systems and reference frames used in this thesis; Section 2.2 details the Multiple Signal Classification (MUSIC) angle of arrival algorithm and associated theoretical performance; Section 2.3 summarizes two existing angle of arrival geolocation methods; Section 2.4 describes maximum likelihood estimation, Gauss-Newton iterations, and the Cramér-Rao lower bound; Section 2.5 details the maximum likelihood parameter estimation of a sinusoidal signal; and Section 2.6 describes a method to visualize the confidence of estimated parameters.

2.1   Coordinate Systems and Reference Frames

The following coordinate systems and reference frames are used throughout this thesis to define relative position and attitude geometries. The Earth Centered Earth Fixed (ECEF) coordinate system is used for positioning in terms of 3D Cartesian coordinates. The Geodetic coordinate system using the World Geodetic System (WGS) 84 model is used for positioning in terms of latitude, longitude, and altitude. The local ECEF reference frame is a translated ECEF coordinate system. The East North Up (ENU) reference frame is used to define the satellite local reference frame. The sensor reference frame is used to define the antenna array geometry with respect to the satellite local reference frame. The relationship between the ECEF, geodetic, and ENU coordinate systems is shown in Figure 2.1.

The ECEF frame is a geocentric right handed 3D Cartesian coordinate system with the origin at the center of mass of the Earth. The X_e-axis points towards the intersection of the equator and the prime meridian (0° latitude 0° longitude), the Z_e-axis points towards the

3
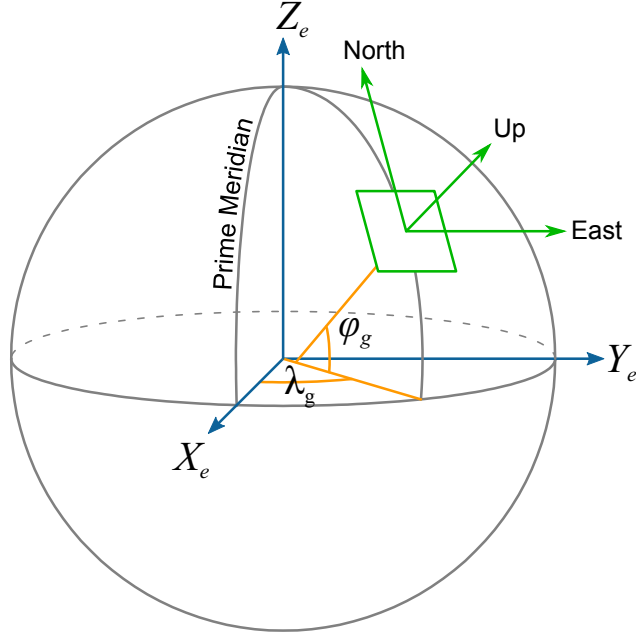
Figure 2.1: Relationship between the ECEF (X_e, Y_e, Z_e), geodetic ($\varphi_g, \lambda_g, h_g$), and ENU coordinate systems [7].

north pole (0° latitude 90° longitude), and the Y_e-axis is normal to the X_eZ_e-plane in accordance with the right hand rule.

The geodetic frame is an angular coordinate system which uses an ellipsoidal approximation of the Earth geoid to define a 3D point in terms of latitude (φ_g), longitude (λ_g), and altitude (h_g). Latitude is the angle measured from the equatorial plane to the point normal to the surface of the ellipsoid and ranges from −90° to 90°. Longitude is the angle measured counterclockwise from the prime meridian in the equatorial plane and ranges from −180° to 180°. Altitude is the height above the surface of the ellipsoid along the longitude vector. The reference ellipsoid model used in this thesis is the WGS 84 ellipsoid with the key parameters listed in Table 2.1.

The local ECEF reference frame is specified by the origin located at a point **p** in ECEF coordinates and is a translation of the ECEF coordinate system. The X'_e, Y'_e, and Z'_e axes of

Table 2.1: WGS 84 key parameters [8].

Semi-major axis	6378137 m
Semi-minor axis	6356752.3142 m
Eccentricity	0.0818191908426
Inverse flattening	298.257223563

the local ECEF reference frame are parallel to the X_e, Y_e, and Z_e axes of the ECEF frame, respectively.

The local ENU reference frame is used as the satellite reference frame and is specified by an origin and the vectors east, north, and up. The location of the origin is located at point **p** in ECEF coordinates. The up vector (U-axis) points along the longitude vector and is normal to the ellipsoid surface. The north vector (N-axis) points towards the north pole (X_e-axis) and is tangent to the ellipsoid surface. The east vector (E-axis) is normal to the UN-plane in accordance with the right hand rule. The NE-plane of the ENU frame is at the altitude h_g of **p** and is tangent to the surface of the ellipsoid at λ_g and φ_g.

The sensor reference frame is used to specify the position of an antenna array within the local satellite ENU reference frame and consists of a right handed orthogonal set of x, y, and z axes originating from point **p**. The relationship between the sensor frame and ENU frame is dependent on the orientation of the satellite and is detailed in Section 3.2. A summary of the reference frames used in this research is shown in Table 2.2 and the angles are defined in the following sections.

2.2 Multiple Signal Classification with a Uniform Circular Array

The first step of the AOA geolocation process is to determine the AOA of an impinging RF signal. The MUSIC algorithm with a Uniform Circular Array (UCA) antenna utilizes the phase delays of an impinging Electromagnetic (EM) wavefront across the individual

Table 2.2: Reference frames.

Reference Frame	Origin	Axes	Angles
ECEF	Center of mass of the earth	$X_e Y_e Z_e$	
Local ECEF	ECEF position $\mathbf{p}$	$X'_e Y'_e Z'_e$	α, ε
Local ENU	ECEF position $\mathbf{p}$	ENU	ϕ_{ENU}, θ_{ENU}
Sensor	ECEF position $\mathbf{p}$	xyz	ϕ, θ

antenna elements to determine the AOA. The AOA and position of the receiver platform are used to generate a 3D Line of Bearing (LOB) in the direction of the emitter.

2.2.1 Signal Model.

Consider a general complex baseband signal $s(t)$ of unit magnitude $|s(t)| = 1$ where $\text{Re}\{s(t)\}$ and $\text{Im}\{s(t)\}$ are the In-phase and Quadrature-phase components, respectively. The wireless RF transmission of $s(t)$ is [9]

$$s_t(t) = \text{Re}\left\{ \sqrt{\sigma_t^2} s(t) e^{j\omega_c t} \right\} \tag{2.1}$$

where σ_t^2 is the transmitted signal power in Watts, $\omega_c = 2\pi f_c$ is the carrier frequency in rad/s, and f_c is the carrier frequency in Hz.

The signal received by an antenna after the transmitted EM wave propagates through the atmosphere and free space is

$$s_r(t) = \text{Re}\left\{ \sqrt{\sigma_r^2(t)} s(t) e^{j\omega_c t} e^{j\omega_D(t)t} \right\} \tag{2.2}$$

where $\sigma_r^2(t)$ is the received power and $\omega_D(t)$ is the Doppler frequency shift due to the relative velocity between the transmitter and receiver.

The received power is given as [10, 11]

$$\sigma_r^2(t) = \frac{\sigma_t^2 G_t G_r}{L_a L_p L_s \left(d(t), \lambda_c \right)} \tag{2.3}$$

6

where G_t is the gain of the transmit antenna, G_r is the gain of the receive antenna, L_a is the atmospheric loss, L_p is the polarization mismatch loss, $L_s(d(t), \lambda_c)$ is the free space propagation loss, $d(t)$ is the Euclidean distance (range) from the transmitter to receiver, and λ_c is the wavelength of the transmitted signal. The free space propagation loss is [10]

$$L_s(d(t), \lambda_c) = \left(\frac{4\pi d(t)}{\lambda_c} \right)^2 \tag{2.4}$$

where

$$\lambda_c = \frac{c}{f_c} \tag{2.5}$$

and $c = 299{,}792{,}458$ m/s is the speed of light in a vacuum [10].

The Doppler frequency shift is

$$\omega_D(t) = \frac{-\dot{d}(t)}{c}\omega_c \tag{2.6}$$

where $\dot{d}(t)$ is the time derivative of the distance (range rate) between the transmitter and receiver. Equation (2.6) is derived from [5, 11]

$$\omega_r(t) = \left(1 - \frac{\dot{d}(t)}{c} \right)\omega_c = \omega_c + \omega_D(t) \tag{2.7}$$

where $\omega_r(t) = 2\pi f_r(t)$ is the frequency of the received signal in rad/s and $f_r(t)$ is the received frequency in Hz.

The received signal after complex demodulation is [9]

$$s_d(t) = s_r(t)e^{-j\omega_c t} = \sqrt{\sigma_r^2(t)}s(t)e^{j\omega_D(t)t} \tag{2.8}$$

and after sampling, with a period of T_s, becomes

$$s_d[n] = \sqrt{\sigma_r^2[n]}s[n]e^{j\omega_D[n]n} \tag{2.9}$$

where $n = t|_{t=nT_s}$ is the discrete sample index.

Consider a planar EM wavefront impinging on a M element UCA antenna [12–16]. The antenna elements lie in the xy plane of the sensor reference frame and are uniformly

7

spaced around the circumference of a circle of radius r. As the plane wave propagates across the UCA, it will arrive at each element at a different time as shown in Figure 2.2. The reception time delays are observed as phase delays in the received signals. The AOA of the wavefront is given in terms of elevation and azimuth angles, θ and ϕ respectively. θ is measured down from the z axis and ϕ is measured counterclockwise from the x axis as shown in Figure 2.3. The observed phase delay is a function of the array geometry (radius and element spacing), the wavelength of the impinging signal, and the AOA. If the receiving antenna elements are assumed to be identical and omnidirectional, the phase delay referenced to the center of the UCA at the m-th element is given as [15]

$$a_m(\theta, \phi) = \exp\left(j\frac{2\pi}{\lambda_r}r\sin(\theta)\cos(\phi - \gamma_m)\right) \tag{2.10}$$

where $\lambda_r = c/f_r$ is the wavelength of the received signal and $\gamma_m = 2\pi(m-1)/M$ is the counterclockwise angle of the m-th element to the x axis. In order to avoid spatial aliasing, adjacent antenna elements are required to be spaced no further apart than $\lambda_r/2$ [12].
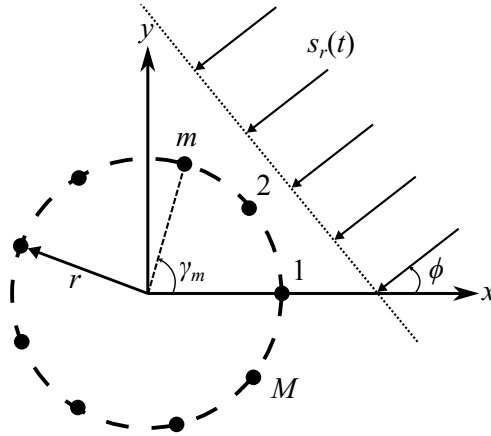
Figure 2.2: Uniform circular array phase delay. A planar wavefront will arrive at each antenna element at a different time. The time difference is observed as a phase delay in the received signal [9].

8
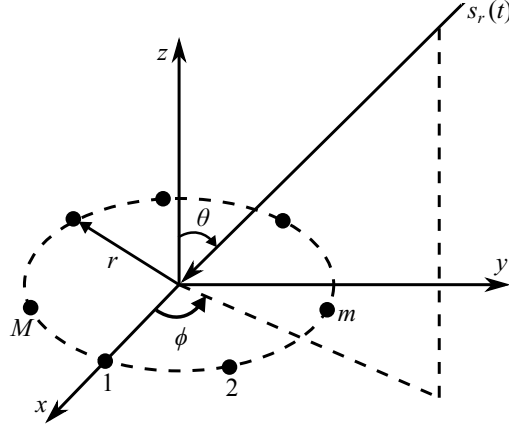
Figure 2.3: Uniform circular array geometry. M identical antenna elements lie in the xy plane of the sensor reference frame and are evenly spaced along the circumference of a circle of radius r. For an impinging planar wavefront, the elevation θ and azimuth ϕ angles of arrival are measured down from the z axis and counterclockwise from the x axis, respectively [16].

If it is assumed that the impinging signal is narrowband such that the propagation delay across the antenna array is much smaller than the reciprocal of the bandwidth of the impinging signal [9, 13], then the signal from the m-th antenna element after demodulation and sampling is [15]

$$x_m[n] = a_m(\theta, \phi)s_d[n] + w_m[n] \tag{2.11}$$

where $w_m[n]$ is a zero mean complex Additive White Gaussian Noise (AWGN) random process with covariance $\sigma_w^2 \mathbf{I}$. It is commonly assumed [12, 13, 16–18] that the noise $w_m[n]$ is spatially and temporally independent of the signal $s_d[n]$. The power of $w_m[n]$ is given as [10, 11]

$$\sigma_w^2 = \kappa T_{sys} W \tag{2.12}$$

where $\kappa = 1.3806504 \times 10^{-23}$ J/K is the Boltzmann constant [10, 11], T_{sys} is the noise temperature of the receiver system, and W is the bandwidth of interest.

Using compact matrix notation for the M antenna array signals with one impinging signal present and N samples,

$$\mathbf{X} = \mathbf{a}\,(\theta, \phi)\,\mathbf{s} + \mathbf{W} \tag{2.13}$$

where

$$\mathbf{X} = \begin{bmatrix} x_1[1] & x_1[2] & \cdots & x_1[N] \\ x_2[1] & x_2[2] & \cdots & x_2[N] \\ \vdots & \vdots & \ddots & \vdots \\ x_M[1] & x_M[2] & \cdots & x_M[N] \end{bmatrix}_{M \times N} = \begin{bmatrix} \mathbf{x}[1] & \mathbf{x}[2] & \cdots & \mathbf{x}[N] \end{bmatrix}_{M \times N} \tag{2.14}$$

are the M received signals as defined in (2.11) and $\mathbf{x}[n]$ is the received signal vector at sample n,

$$\mathbf{a}\,(\theta, \phi) = \begin{bmatrix} a_1(\theta, \phi) \\ a_2(\theta, \phi) \\ \vdots \\ a_M(\theta, \phi) \end{bmatrix}_{M \times 1} \tag{2.15}$$

is the steering vector comprised of the antenna element phase delays defined in (2.10),

$$\mathbf{s} = \begin{bmatrix} s_1[1] & s_1[2] & \cdots & s_1[N] \end{bmatrix}_{1 \times N} \tag{2.16}$$

is the sampled demodulated signal and,

$$\mathbf{W} = \begin{bmatrix} w_1[1] & w_1[2] & \cdots & w_1[N] \\ w_2[1] & w_2[2] & \cdots & w_2[N] \\ \vdots & \vdots & \ddots & \vdots \\ w_M[1] & w_M[2] & \cdots & w_M[N] \end{bmatrix}_{M \times N} \tag{2.17}$$

are independent noise realizations.

The general signal model for M antenna elements, K impinging signals, and N samples is given as [9, 19]

$$\mathbf{X} = \mathbf{AS} + \mathbf{W} \tag{2.18}$$

where each column of $\mathbf{A}$ is the steering vector of the k-th impinging signal,

$$\mathbf{A} = \left[\begin{array}{cccc} \mathbf{a}(\theta_1, \phi_1) & \mathbf{a}(\theta_2, \phi_2) & \cdots & \mathbf{a}(\theta_K, \phi_K) \end{array}\right]_{M \times K} \tag{2.19}$$

and $\mathbf{S}$ is the collection of K demodulated signals

$$\mathbf{S} = \begin{bmatrix} s_1[1] & s_1[2] & \cdots & s_1[N] \\ s_2[1] & s_2[2] & \cdots & s_2[N] \\ \vdots & \vdots & \ddots & \vdots \\ s_K[1] & s_K[2] & \cdots & s_K[N] \end{bmatrix}_{K \times N}. \tag{2.20}$$

2.2.2 MUSIC Algorithm.

The MUSIC algorithm [19] utilizes the eigenstructure of the spatial covariance matrix of the signals received by M antenna elements to determine the AOA of K impinging signals. The $M \times M$ spatial covariance matrix is given as [9]

$$\mathbf{R}_{xx} = E\left[\mathbf{X}\mathbf{X}^H\right] = E\left[(\mathbf{A}\mathbf{S} + \mathbf{W})(\mathbf{A}\mathbf{S} + \mathbf{W})^H\right] = \mathbf{A}E\left[\mathbf{S}\mathbf{S}^H\right]\mathbf{A}^H + E\left[\mathbf{W}\mathbf{W}^H\right]. \tag{2.21}$$

Since it is assumed that the noise is an uncorrelated zero mean complex AWGN process, the noise covariance matrix is

$$E\left[\mathbf{W}\mathbf{W}^H\right] = \sigma_w^2 \mathbf{I}_{M \times M} \tag{2.22}$$

and (2.21) becomes

$$\mathbf{R}_{xx} = \mathbf{A}\mathbf{R}_{ss}\mathbf{A}^H + \sigma_w^2 \mathbf{I}_{M \times M} \tag{2.23}$$

where

$$\mathbf{R}_{ss} = E\left[\mathbf{S}\mathbf{S}^H\right] \tag{2.24}$$

is the $K \times K$ signal covariance matrix. In the case of zero mean uncorrelated signals,

$$\mathbf{R}_{ss} = \mathrm{diag}\left[\sigma_1^2, \sigma_2^2, \cdots, \sigma_K^2\right] \tag{2.25}$$

where $\sigma_1^2, \sigma_2^2, \ldots, \sigma_K^2$ are the signal powers [15, 20].

11

Since $\mathbf{R}_{xx}$ is a Hermitian matrix by design ($\mathbf{R}_{xx} = \mathbf{R}_{xx}^H$), it has a unitary eigendecomposition with real eigenvalues and orthonormal eigenvectors [21]. When the number of signals is less than the number of antenna array elements ($K < M$) the eigendecomposition of the spatial covariance matrix can be arranged such that [9]

$$\mathbf{R}_{xx} = \mathbf{QDQ}^H = \begin{bmatrix} \mathbf{Q}_s & \mathbf{Q}_w \end{bmatrix} \begin{bmatrix} \mathbf{D}_s & 0 \\ 0 & \sigma_w^2 \mathbf{I} \end{bmatrix} \begin{bmatrix} \mathbf{Q}_s & \mathbf{Q}_w \end{bmatrix}^H \tag{2.26}$$

where $\mathbf{Q}_s$ consists of the K eigenvectors which span the signal subspace with corresponding eigenvalues $\mathbf{D}_s = \mathrm{diag}\left[\lambda_1 + \sigma_w^2, \lambda_2 + \sigma_w^2, \cdots, \lambda_K + \sigma_w^2\right]$ and $\mathbf{Q}_w$ consists of the $M - K$ eigenvectors which span the noise subspace with corresponding eigenvalues σ_w^2. The form of (2.26) comes about when the eigenvalues contained in $\mathbf{D}$ are arranged in descending order.

When $K < M$ the matrix $\mathbf{AR}_{ss}\mathbf{A}^H$ is singular with rank K and the relation [19]

$$\det\left(\mathbf{AR}_{ss}\mathbf{A}^H\right) = \det\left(\mathbf{R}_{xx} - \sigma_w^2 \mathbf{I}\right) = 0 \tag{2.27}$$

indicates that σ_w^2 is an eigenvalue of $\mathbf{R}_{xx}$ which occurs $M - K$ times. An eigenvector $\mathbf{q}_w$ of $\mathbf{R}_{xx}$ corresponding with a σ_w^2 eigenvalue is shown to be orthogonal to the columns of $\mathbf{A}$ [9]

$$\mathbf{R}_{xx}\mathbf{q}_w = \left(\mathbf{AR}_{ss}\mathbf{A}^H + \sigma_w^2 \mathbf{I}\right)\mathbf{q}_w = 0 + \sigma_w^2 \mathbf{I}\mathbf{q}_w = \sigma_w^2 \mathbf{q}_w \tag{2.28}$$

and the $M - K$ $\mathbf{q}_w$ eigenvectors span the noise subspace defined by the columns of $\mathbf{Q}_w$. There are K linearly independent eigenvectors $\mathbf{q}_s$ with corresponding eigenvalues λ_s of the matrix $\mathbf{AR}_{ss}\mathbf{A}^H$ which are also eigenvectors of $\mathbf{R}_{xx}$ as shown by [9]

$$\mathbf{R}_{xx}\mathbf{q}_s = \left(\mathbf{AR}_{ss}\mathbf{A}^H + \sigma_w^2 \mathbf{I}\right)\mathbf{q}_s = \lambda_s\mathbf{q}_s + \sigma_w^2 \mathbf{I}\mathbf{q}_s = \left(\lambda_s + \sigma_w^2\right)\mathbf{q}_s \tag{2.29}$$

where $\lambda_s + \sigma_w^2$ is the corresponding eigenvalue of $\mathbf{R}_{xx}$. The K $\mathbf{q}_s$ eigenvectors span the signal subspace defined by the columns of $\mathbf{Q}_s$. Sorting the M eigenvalues of $\mathbf{R}_{xx}$ contained in $\mathbf{D}$ in descending order ($\lambda_1 + \sigma_w^2 > \cdots > \lambda_K + \sigma_w^2 > \sigma_w^2 \geq \cdots \geq \sigma_w^2$),

$$\mathbf{D} = \mathrm{diag}\left[\lambda_1 + \sigma_w^2, \cdots, \lambda_K + \sigma_w^2, \sigma_w^2, \cdots, \sigma_w^2\right] = \begin{bmatrix} \mathbf{D}_s & 0 \\ 0 & \sigma_w^2 \mathbf{I} \end{bmatrix}_{M \times M}, \tag{2.30}$$

and arranging the corresponding K eigenvectors of $\mathbf{Q}_s$ and $M - K$ eigenvectors of $\mathbf{Q}_w$ to partition the $\mathbf{Q}$ matrix

$$\mathbf{Q} = \begin{bmatrix} \mathbf{Q}_s & \mathbf{Q}_w \end{bmatrix} \tag{2.31}$$

yields the eigendecomposition shown in (2.26). Since the eigenvectors contained in $\mathbf{Q}$ are orthonormal, the signal subspace is orthogonal to the noise subspace ($\mathbf{Q}_s^H \mathbf{Q}_w = \mathbf{0}$).

The orthogonality of the signal and noise subspaces provides a means to determine the AOA of the impinging signals. The columns of $\mathbf{A}$ are the signal steering vectors which lie in the signal subspace. Due to subspace orthogonality, $\mathbf{a}^H (\theta, \phi) \mathbf{Q}_w = \mathbf{0}$ when θ and ϕ are the angles of an impinging signal. Since the steering vector is a function of the known antenna array geometry, evaluation of the MUSIC spectrum [9, 19]

$$P_{\text{MUSIC}} (\theta, \phi) = \frac{1}{\mathbf{a}^H (\theta, \phi) \mathbf{Q}_w \mathbf{Q}_w^H \mathbf{a} (\theta, \phi)} \tag{2.32}$$

over the range of θ and ϕ will yield peaks whenever θ and ϕ correspond to the AOA of an impinging signal. The location of the peaks are taken as the AOA estimates of $\hat{\theta}$ and $\hat{\phi}$. In practice, $\mathbf{R}_{xx}$ is estimated from the received signal data [9, 12, 13]

$$\hat{\mathbf{R}}_{xx} = \frac{1}{N} \sum_{n=1}^{N} \mathbf{x}[n]\mathbf{x}^H[n] = \frac{1}{N} \mathbf{X}\mathbf{X}^H \tag{2.33}$$

and the estimate of the noise subspace $\hat{\mathbf{Q}}_w$ is used in (2.32) with a grid search over the range of θ and ϕ. An example of the MUSIC spectrum is shown in Figure 2.4 with peaks corresponding to the AOA of the impinging signals.

2.2.3   MUSIC Theoretical Performance.

Analytic expressions for the theoretical performance of MUSIC using a UCA have been developed in [12, 13] from a first order Taylor series expansion of the MUSIC spectrum in the vicinity of the true AOA. The expressions are asymptotic for a large number of N samples and yield the error, covariance, and variances of the estimated angles. The following derivation is adapted from [12, 13] in terms of the elevation θ and azimuth ϕ angles of the impinging signals.

13
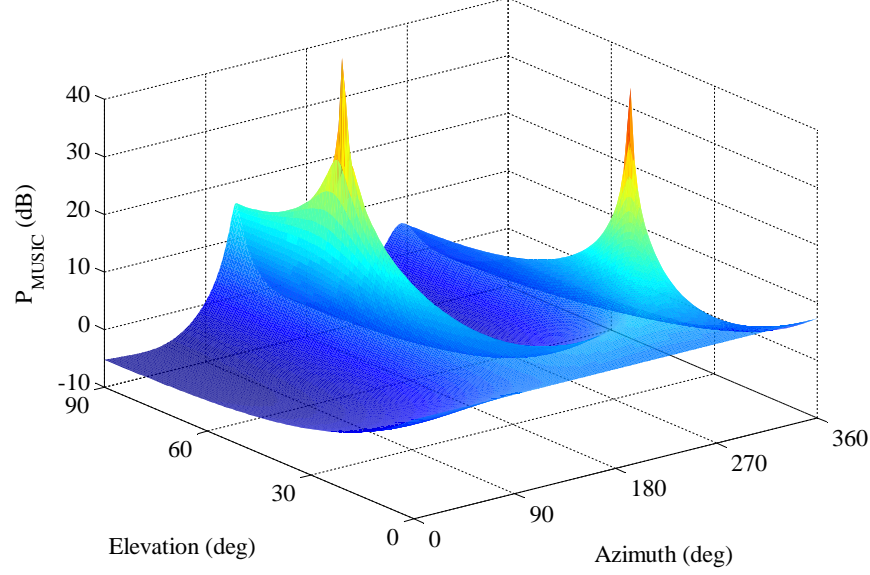
Figure 2.4: Example MUSIC spectrum for a 4 element UCA with 2 impinging signals. The peaks at $(\theta_1, \phi_1) = (60°, 120°)$ and $(\theta_2, \phi_2) = (25°, 270°)$ correspond to the AOAs of the impinging signals.

The estimated angle error vector of the k-th impinging signal in the sensor reference frame is defined as

$$\mathbf{e}_{\theta\phi,k} = \begin{bmatrix} \hat{\theta}_k - \theta_k \\ \hat{\phi}_k - \phi_k \end{bmatrix} \tag{2.34}$$

and is evaluated as

$$\mathbf{e}_{\theta\phi,k} = \left[\mathbf{E}^{-1}\mathbf{d} \right]\Big|_{\theta=\theta_k, \phi=\phi_k} \tag{2.35}$$

where

$$\mathbf{E} = \begin{bmatrix} \mathbf{a}_\theta^H \hat{\mathbf{Q}}_w \hat{\mathbf{Q}}_w^H \mathbf{a}_\theta & \mathrm{Re}\left\{\mathbf{a}_\phi^H \hat{\mathbf{Q}}_w \hat{\mathbf{Q}}_w^H \mathbf{a}_\theta\right\} \\ \mathrm{Re}\left\{\mathbf{a}_\phi^H \hat{\mathbf{Q}}_w \hat{\mathbf{Q}}_w^H \mathbf{a}_\theta\right\} & \mathbf{a}_\phi^H \hat{\mathbf{Q}}_w \hat{\mathbf{Q}}_w^H \mathbf{a}_\phi \end{bmatrix} \tag{2.36}$$

and

$$\mathbf{d} = \begin{bmatrix} -\mathrm{Re}\left\{\mathbf{a}^H \hat{\mathbf{Q}}_w \hat{\mathbf{Q}}_w^H \mathbf{a}_\theta\right\} \\ -\mathrm{Re}\left\{\mathbf{a}^H \hat{\mathbf{Q}}_w \hat{\mathbf{Q}}_w^H \mathbf{a}_\phi\right\} \end{bmatrix}. \tag{2.37}$$

14

The terms $\mathbf{a}_\theta$ and $\mathbf{a}_\phi$ are the partial derivatives of $\mathbf{a}$ with respect to θ and ϕ,

$$\mathbf{a}_\theta = \frac{\partial \mathbf{a}}{\partial \theta} = \begin{bmatrix} j\frac{2\pi}{\lambda_r}r\cos(\theta)\cos(\phi-\gamma_1)\exp\left[j\frac{2\pi}{\lambda_r}r\sin(\theta)\cos(\phi-\gamma_1)\right] \\ \vdots \\ j\frac{2\pi}{\lambda_r}r\cos(\theta)\cos(\phi-\gamma_M)\exp\left[j\frac{2\pi}{\lambda_r}r\sin(\theta)\cos(\phi-\gamma_M)\right] \end{bmatrix} \tag{2.38}$$

$$\mathbf{a}_\phi = \frac{\partial \mathbf{a}}{\partial \phi} = \begin{bmatrix} -j\frac{2\pi}{\lambda_r}r\sin(\theta)\sin(\phi-\gamma_1)\exp\left[j\frac{2\pi}{\lambda_r}r\sin(\theta)\cos(\phi-\gamma_1)\right] \\ \vdots \\ -j\frac{2\pi}{\lambda_r}r\sin(\theta)\sin(\phi-\gamma_M)\exp\left[j\frac{2\pi}{\lambda_r}r\sin(\theta)\cos(\phi-\gamma_M)\right] \end{bmatrix}. \tag{2.39}$$

The error vector of the k-th impinging signal is Gaussian distributed with zero mean and covariance matrix

$$\mathbf{C}_{\hat{\theta}\hat{\phi},k} = \frac{\sigma_w^2\rho}{2K\det(\mathbf{E})}\left.\begin{bmatrix} \mathbf{a}_\phi^H\hat{\mathbf{Q}}_w\hat{\mathbf{Q}}_w^H\mathbf{a}_\phi & \mathrm{Re}\left\{\mathbf{a}_\phi^H\hat{\mathbf{Q}}_w\hat{\mathbf{Q}}_w^H\mathbf{a}_\theta\right\} \\ \mathrm{Re}\left\{\mathbf{a}_\phi^H\hat{\mathbf{Q}}_w\hat{\mathbf{Q}}_w^H\mathbf{a}_\theta\right\} & \mathbf{a}_\theta^H\hat{\mathbf{Q}}_w\hat{\mathbf{Q}}_w^H\mathbf{a}_\theta \end{bmatrix}\right|_{\theta=\theta_k,\phi=\phi_k} \tag{2.40}$$

where

$$\rho = \left[\mathbf{R}_{ss}^{-1}\right]_{k,k} + \sigma_w^2\left[\mathbf{R}_{ss}^{-1}\left(\mathbf{A}^H\mathbf{A}\right)^{-1}\mathbf{R}_{ss}^{-1}\right]_{k,k}. \tag{2.41}$$

In the case of a single impinging signal,

$$\rho = \sigma_s^{-2} + \sigma_w^2\sigma_s^{-2}\left(\mathbf{a}^H\mathbf{a}\right)^{-1}\sigma_s^{-2}. \tag{2.42}$$

2.2.4   CRLB for 2D Angle Estimation of a Single Source Using a UCA.

This section derives the stochastic Cramér-Rao Lower Bound (CRLB) for 2D angle of arrival estimation of a single source using a UCA and follows a similar derivation found in [22]. The CRLB is the lower bound on the variance of any unbiased estimator of θ and ϕ

$$\begin{bmatrix} \mathrm{var}\left(\hat{\theta}\right) & \mathrm{cov}\left(\hat{\theta},\hat{\phi}\right) \\ \mathrm{cov}\left(\hat{\phi},\hat{\theta}\right) & \mathrm{var}\left(\hat{\phi}\right) \end{bmatrix} \geq \mathrm{CRLB}\left(\hat{\theta},\hat{\phi}\right) \tag{2.43}$$

and is equal to the inverse of the Fisher Information Matrix (FIM)

$$\mathrm{CRLB}\left(\hat{\theta},\hat{\phi}\right) = \mathbf{F}^{-1}(\theta,\phi). \tag{2.44}$$

From (2.23) the received signal covariance matrix for a single impinging source is

$$\mathbf{R}_{xx} = \sigma_s^2 \mathbf{a}\mathbf{a}^H + \sigma_w^2 \mathbf{I}_{M \times M} \tag{2.45}$$

where $\mathbf{a}$ is the steering vector as defined in (2.15), σ_s^2 is the signal power, and σ_w^2 is the noise power. Since the received signal vector $\mathbf{X}$ is assumed to be a complex valued Gaussian distrusted random process with zero mean and covariance matrix $\mathbf{R}_{xx}$, the stochastic FIM for the parameters θ and ϕ is given as [22, 23]

$$\mathbf{F}(\theta, \phi) = \begin{bmatrix} \text{trace} \left\{ \frac{\partial \mathbf{R}_{xx}}{\partial \theta} \mathbf{R}_{xx}^{-1} \frac{\partial \mathbf{R}_{xx}}{\partial \theta} \mathbf{R}_{xx}^{-1} \right\} & \text{trace} \left\{ \frac{\partial \mathbf{R}_{xx}}{\partial \theta} \mathbf{R}_{xx}^{-1} \frac{\partial \mathbf{R}_{xx}}{\partial \phi} \mathbf{R}_{xx}^{-1} \right\} \\ \text{trace} \left\{ \frac{\partial \mathbf{R}_{xx}}{\partial \phi} \mathbf{R}_{xx}^{-1} \frac{\partial \mathbf{R}_{xx}}{\partial \theta} \mathbf{R}_{xx}^{-1} \right\} & \text{trace} \left\{ \frac{\partial \mathbf{R}_{xx}}{\partial \phi} \mathbf{R}_{xx}^{-1} \frac{\partial \mathbf{R}_{xx}}{\partial \phi} \mathbf{R}_{xx}^{-1} \right\} \end{bmatrix} \tag{2.46}$$

where the partial derivatives of the covariance matrix with respect to θ and ϕ are

$$\frac{\partial \mathbf{R}_{xx}}{\partial \theta} = \sigma_s^2 \mathbf{a}_\theta \mathbf{a}^H + \sigma_s^2 \mathbf{a}\mathbf{a}_\theta^H \tag{2.47}$$

$$\frac{\partial \mathbf{R}_{xx}}{\partial \phi} = \sigma_s^2 \mathbf{a}_\phi \mathbf{a}^H + \sigma_s^2 \mathbf{a}\mathbf{a}_\phi^H. \tag{2.48}$$

Element 1,1 of the FIM is

$$\mathbf{F}_{1,1}(\theta, \phi) = \text{trace} \left\{ \frac{\partial \mathbf{R}_{xx}}{\partial \theta} \mathbf{R}_{xx}^{-1} \frac{\partial \mathbf{R}_{xx}}{\partial \theta} \mathbf{R}_{xx}^{-1} \right\} \tag{2.49}$$

and is evaluated by substituting (2.47) into (2.46)

$$\mathbf{F}_{1,1}(\theta, \phi) = \left(\sigma_s^2 \right)^2 \text{trace} \left\{ \left(\mathbf{a}_\theta \mathbf{a}^H \mathbf{R}_{xx}^{-1} + \mathbf{a}\mathbf{a}_\theta^H \mathbf{R}_{xx}^{-1} \right) \left(\mathbf{a}_\theta \mathbf{a}^H \mathbf{R}_{xx}^{-1} + \mathbf{a}\mathbf{a}_\theta^H \mathbf{R}_{xx}^{-1} \right) \right\}. \tag{2.50}$$

Performing the matrix trace operation yields

$$\mathbf{F}_{1,1}(\theta, \phi) = \left(\sigma_s^2 \right)^2 \left[\left(\mathbf{a}^H \mathbf{R}_{xx}^{-1} \mathbf{a}_\theta \right)^2 + 2 \left(\mathbf{a}^H \mathbf{R}_{xx}^{-1} \mathbf{a} \right) \left(\mathbf{a}_\theta^H \mathbf{R}_{xx}^{-1} \mathbf{a}_\theta \right) + \left(\mathbf{a}_\theta^H \mathbf{R}_{xx}^{-1} \mathbf{a} \right)^2 \right]. \tag{2.51}$$

The terms of (2.51) are evaluated by making use of the following:

$$\mathbf{a}^H \mathbf{a}_\theta = j \frac{2\pi}{\lambda_r} r \cos(\theta) \sum_{m=1}^{M} \cos(\phi - \gamma_m) = 0 \tag{2.52}$$

$$\mathbf{a}_\theta^H \mathbf{a} = -\mathbf{a}^H \mathbf{a}_\theta = 0 \tag{2.53}$$

16

$$\mathbf{a}^H \mathbf{a}_\phi = j\frac{2\pi}{\lambda_r} r \sin(\theta) \sum_{m=1}^{M} \sin(\phi - \gamma_m) = 0 \tag{2.54}$$

$$\mathbf{a}_\phi^H \mathbf{a} = -\mathbf{a}^H \mathbf{a}_\phi = 0 \tag{2.55}$$

since for a UCA, the phase center of the array is located at the center of the array [22]

such that

$$\begin{aligned} \sum_{m=1}^{M} \cos(\phi - \gamma_m) &= 0 \\ \sum_{m=1}^{M} \sin(\phi - \gamma_m) &= 0. \end{aligned} \tag{2.56}$$

The inverse of the signal covariance matrix is evaluated using the Woodbury matrix identity [22]

$$(A + BCD)^{-1} = A^{-1} - A^{-1}B\left(C^{-1} + DA^{-1}B\right)^{-1}DA^{-1} \tag{2.57}$$

such that

$$\mathbf{R}_{xx}^{-1} = \frac{1}{\sigma_w^2}\left[\mathbf{I} - \frac{1}{\frac{\sigma_w^2}{\sigma_s^2} + \mathbf{a}^H\mathbf{a}}\mathbf{a}\mathbf{a}^H\right]. \tag{2.58}$$

Evaluating the first and last terms of (2.51) yields

$$\mathbf{a}^H \mathbf{R}_{xx}^{-1} \mathbf{a}_\theta = \frac{1}{\sigma_w^2}\left[\mathbf{a}^H\mathbf{a}_\theta - \frac{1}{\frac{\sigma_w^2}{\sigma_s^2} + \mathbf{a}^H\mathbf{a}}\left(\mathbf{a}^H\mathbf{a}\right)\left(\mathbf{a}^H\mathbf{a}_\theta\right)\right] = 0 \tag{2.59}$$

$$\mathbf{a}_\theta^H \mathbf{R}_{xx}^{-1} \mathbf{a} = \frac{1}{\sigma_w^2}\left[\mathbf{a}_\theta^H\mathbf{a} - \frac{1}{\frac{\sigma_w^2}{\sigma_s^2} + \mathbf{a}^H\mathbf{a}}\left(\mathbf{a}_\theta^H\mathbf{a}\right)\left(\mathbf{a}^H\mathbf{a}\right)\right] = 0 \tag{2.60}$$

since $\mathbf{a}_\theta^H\mathbf{a} = \mathbf{a}^H\mathbf{a}_\theta = 0$. The second term of (2.51) is evaluated as

$$\mathbf{a}^H \mathbf{R}_{xx}^{-1} \mathbf{a} = \frac{1}{\sigma_w^2}\left[\mathbf{a}^H\mathbf{a} - \frac{1}{\frac{\sigma_w^2}{\sigma_s^2} + \mathbf{a}^H\mathbf{a}}\left(\mathbf{a}^H\mathbf{a}\right)\left(\mathbf{a}^H\mathbf{a}\right)\right] \tag{2.61}$$

and after simplification with $\mathbf{a}^H\mathbf{a} = \|\mathbf{a}\|^2$ and a common denominator becomes

$$\mathbf{a}^H \mathbf{R}_{xx}^{-1} \mathbf{a} = \frac{1}{\sigma_s^2}\frac{\|\mathbf{a}\|^2}{\frac{\sigma_w^2}{\sigma_s^2} + \|\mathbf{a}\|^2}. \tag{2.62}$$

Similarly, the third term of (2.51) is evaluated as

$$\mathbf{a}_\theta^H \mathbf{R}_{xx}^{-1} \mathbf{a}_\theta = \frac{1}{\sigma_w^2}\left[\mathbf{a}_\theta^H\mathbf{a}_\theta - \frac{1}{\frac{\sigma_w^2}{\sigma_s^2} + \mathbf{a}^H\mathbf{a}}\left(\mathbf{a}_\theta^H\mathbf{a}\right)\left(\mathbf{a}^H\mathbf{a}_\theta\right)\right] = \frac{1}{\sigma_w^2}\|\mathbf{a}_\theta\|^2. \tag{2.63}$$

17

Continuing with the evaluation of element 1,1 of the FIM, (2.51) becomes

$$\mathbf{F}_{1,1}(\theta,\phi) = 2\frac{\sigma_s^2}{\sigma_w^2}\frac{\|\mathbf{a}\|^2}{\frac{\sigma_w^2}{\sigma_s^2} + \|\mathbf{a}\|^2}\|\mathbf{a}_\theta\|^2 \tag{2.64}$$

and with the assumption of omnidirectional antenna element such that $\|\mathbf{a}\|^2 = M$ [22],

(2.64) becomes

$$\mathbf{F}_{1,1}(\theta,\phi) = 2\frac{\sigma_s^2}{\sigma_w^2}\frac{M}{\frac{\sigma_w^2}{\sigma_s^2} + M}\|\mathbf{a}_\theta\|^2. \tag{2.65}$$

Evaluating the term

$$\|\mathbf{a}_\theta\|^2 = (2\pi r/\lambda_r)^2\cos^2(\theta)\sum_{m=1}^{M}\cos^2(\theta - \gamma_m) \tag{2.66}$$

and noting that

$$\sum_{m=1}^{M}\cos^2(\theta - \gamma_m) = \sum_{m=1}^{M}\frac{1 + \cos(2\theta - 2\gamma_m)}{2} = \frac{M}{2} \tag{2.67}$$

yields

$$\|\mathbf{a}_\theta\|^2 = \frac{M}{2}(2\pi r/\lambda_r)^2\cos^2(\theta) \tag{2.68}$$

and (2.65) becomes

$$\mathbf{F}_{1,1}(\theta,\phi) = \frac{\sigma_s^2}{\sigma_w^2}\frac{M^2}{\frac{\sigma_w^2}{\sigma_s^2} + M}(2\pi r/\lambda_r)^2\cos^2(\theta). \tag{2.69}$$

In a similar manner, elements 1,2 and 2,1 of the FIM are evaluated as

$$\mathbf{F}_{1,2}(\theta,\phi) = \mathbf{F}_{2,1}(\theta,\phi) = 2\frac{\sigma_s^2}{\sigma_w^2}\frac{M}{\frac{\sigma_w^2}{\sigma_s^2} + M}(2\pi r/\lambda_r)^2\sum_{m=1}^{M}\cos(\theta - \gamma_m)\sin(\theta - \gamma_m) = 0 \tag{2.70}$$

since

$$\sum_{m=1}^{M}\cos(\theta - \gamma_m)\sin(\theta - \gamma_m) = \sum_{m=1}^{M}\tfrac{1}{2}\sin(2\theta - 2\gamma_m) = 0. \tag{2.71}$$

Element 2,2 of the FIM is evaluated as

$$\mathbf{F}_{2,2}(\theta,\phi) = \frac{\sigma_s^2}{\sigma_w^2}\frac{M^2}{\frac{\sigma_w^2}{\sigma_s^2} + M}(2\pi r/\lambda_r)^2\sin^2(\theta) \tag{2.72}$$

since

$$\sum_{m=1}^{M}\sin^2(\theta - \gamma_m) = \sum_{m=1}^{M}\frac{1 - \cos(2\theta - 2\gamma_m)}{2} = \frac{M}{2}. \tag{2.73}$$

18

Using (2.69), (2.70), and (2.72) the FIM for the parameters θ and ϕ is

$$\mathbf{F}(\theta, \phi) = \frac{\sigma_s^2}{\sigma_w^2} \frac{M^2}{\frac{\sigma_w^2}{\sigma_s^2} + M} (2\pi r/\lambda_r)^2 \begin{bmatrix} \cos^2(\theta) & 0 \\ 0 & \sin^2(\theta) \end{bmatrix}$$ (2.74)

and the AOA CRLB using N samples of the signal $\mathbf{X}$ is the inverse of the FIM [22]

$$\text{CRLB}(\theta, \phi) = \tfrac{1}{N}[\mathbf{F}(\theta, \phi)]^{-1}.$$ (2.75)

Evaluating (2.75) with (2.74) produces the stochastic CRLB on the variance of 2D angle estimates of a single source using a UCA in rad^2

$$\text{CRLB}(\theta, \phi) = \frac{\frac{\sigma_w^2}{\sigma_s^2} + M}{\frac{\sigma_s^2}{\sigma_w^2} NM^2(2\pi r/\lambda_r)^2} \begin{bmatrix} 1/\cos^2(\theta) & 0 \\ 0 & 1/\sin^2(\theta) \end{bmatrix}.$$ (2.76)

Defining η as the Signal to Noise Ratio (SNR),

$$\eta = \frac{\sigma_s^2}{\sigma_w^2}$$ (2.77)

the elevation angle CRLB is

$$\text{var}\left(\hat{\theta}\right) \geq \frac{\eta^{-1} + M}{\eta NM^2(2\pi r/\lambda_r)^2 \cos^2(\theta)}$$ (2.78)

and the azimuth angle CRLB is

$$\text{var}\left(\hat{\phi}\right) \geq \frac{\eta^{-1} + M}{\eta NM^2(2\pi r/\lambda_r)^2 \sin^2(\theta)}.$$ (2.79)

In general, the CRLB for 2D angle estimates is a function of the SNR of the received signal, number of samples N, number of antenna elements M, radius of the UCA r, wavelength of the received signal λ_r, and the elevation angle θ of the received signal.

2.3 Angle of Arrival Geolocation

Geolocation of a RF Signal of Interest (SOI) emitter can be accomplished with a two-step process using the AOA of an impinging signal and the position of the receiver platform when the signal is received. The first step in the process is to determine the AOA

of the received RF signal and generate a LOB in the direction of the received signal from the position of the receiver platform when the signal was received. As the receiver passes over the emitter, the AOA and position will vary, and the process is repeated to generate multiple LOBs. The second step uses the collection of LOBs to estimate the position of the emitter.

2.3.1 Lines of Bearing.

Once the AOA of the received SOI has been determined, the estimated angles along with the attitude and position of the receiver platform are used to generate a 3D LOB in the direction of the emitter. A LOB is a pointing vector originating at the position of the receiver $\mathbf{p}_i$ in the direction of the estimated angles $\hat{\theta}_i$ and $\hat{\phi}_i$. The attitude of the receiver is used to define the LOBs in a common coordinate system and the process is detailed in Section 3.2. In the general case shown in Figure 2.5, the LOB vector $\mathbf{r}_i$ from $\mathbf{p}_i$ to a geolocation point $\mathbf{g}$ in ECEF coordinates is [24]

$$\mathbf{r}_i = \mathbf{g} - \mathbf{p}_i \tag{2.80}$$

with Cartesian components

$$
\begin{aligned}
r_{i,x} &= g_x - p_{i,x} \\
r_{i,y} &= g_y - p_{i,y} \\
r_{i,z} &= g_z - p_{i,z}
\end{aligned}
\tag{2.81}
$$

The azimuth α_i and elevation ε_i angles in the local ECEF frame are [24]

$$
\begin{aligned}
\alpha_i &= \text{atan2}\left(r_{i,y}, r_{i,x}\right) \\
\varepsilon_i &= \text{atan2}\left(\sqrt{r_{i,x}^2 + r_{i,y}^2}, r_{i,z}\right)
\end{aligned}
\tag{2.82}
$$

where α_i is measured counterclockwise from the X_e'-axis and ε_i is measured down from the Z_e'-axis. The angles and Cartesian components are related through

$$
\begin{aligned}
r_{i,x} &= \|\mathbf{r}_i\| \sin(\varepsilon_i) \cos(\alpha_i) \\
r_{i,y} &= \|\mathbf{r}_i\| \sin(\varepsilon_i) \sin(\alpha_i) \\
r_{i,z} &= \|\mathbf{r}_i\| \cos(\varepsilon_i)
\end{aligned}
\tag{2.83}
$$

20

The vector $\mathbf{r}_i$ is the true (error free) LOB from $\mathbf{p}_i$ to $\mathbf{g}$ with the associated bearing angles $\alpha_i(\mathbf{g})$ and $\varepsilon_i(\mathbf{g})$. The estimated i-th LOB in the ECEF coordinate system used for the second step of the geolocation process is defined as a vector originating at point $\mathbf{p}_i$ and pointing in the direction of $\hat{\alpha}_i$ and $\hat{\varepsilon}_i$.
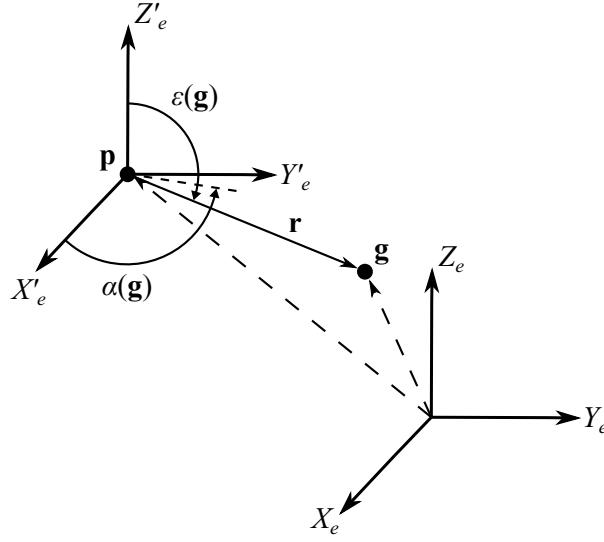
Figure 2.5: LOB vector $\mathbf{r}$ pointing from $\mathbf{p}$ to $\mathbf{g}$ with angles α and ε in the local ECEF frame.

2.3.2 Angle of Arrival Geolocation Methods.

The second step of the AOA geolocation process is to determine the position of a RF SOI emitter from the LOB data sets generated in the first step. If there is a single emitter or multiple emitters that have been segregated, the LOBs as shown in Figure 2.6 will point in the direction of a common position which is assumed to be the location of the emitter. Two methods which utilize LOB data sets to generate geolocation estimates are the Least Squares (LS) intersection [25, 26] and Non-Linear Optimization (NLO) [24, 27].

2.3.2.1 Least Squares Intersection.

Due to various errors (e.g. AOA estimation error, position knowledge error, and attitude knowledge error) the collection of LOBs will not all intersect at the location of the

21
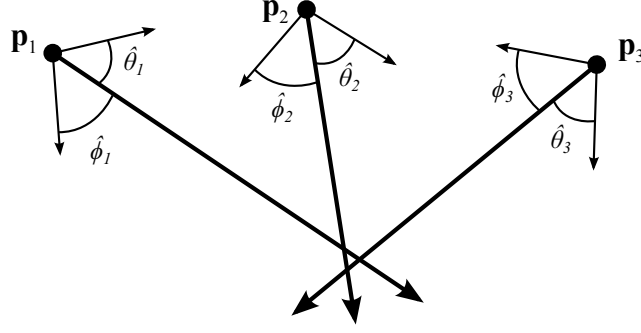
Figure 2.6: Three lines of bearing and a single emitter.

emitter. However, there is a point which minimizes the squared distances between that point and the LOBs. The closest point is found as the LS solution that minimizes the sum of the Euclidean distances squared from a point to a set of L lines [24]. The LS intersection point and distances from four LOBs is shown in Figure 2.7.

The method used in [26] to find the LS intersection point uses the estimated bearing angles $\hat{\alpha}_i$ and $\hat{\varepsilon}_i$ of the i-th LOB to create the Cartesian pointing vector from $\hat{\mathbf{p}}_i$

$$
\mathbf{u}_i = \begin{bmatrix} \sin(\hat{\varepsilon}_i)\cos(\hat{\alpha}_i) \\ \sin(\hat{\varepsilon}_i)\sin(\hat{\alpha}_i) \\ \cos(\hat{\varepsilon}_i) \end{bmatrix}.
\tag{2.84}
$$

The unit vectors of the L LOBs are used to create the following matrices

$$
\mathbf{B} = \sum_{i=1}^{L} \mathbf{I}_{3\times3} - \mathbf{u}_i\mathbf{u}_i^T
\tag{2.85}
$$

$$
\mathbf{b} = \sum_{i=1}^{L} \left(\mathbf{I}_{3\times3} - \mathbf{u}_i\mathbf{u}_i^T\right)\hat{\mathbf{p}}_i
\tag{2.86}
$$

which form a set of linear equations

$$
\mathbf{B}\hat{\mathbf{g}} = \mathbf{b}
\tag{2.87}
$$

where $\hat{\mathbf{g}}$ is the geolocation estimate of the emitter. The LS minimum distance solution [21] to (2.87) is

$$
\hat{\mathbf{g}}_{LS} = \left(\mathbf{B}^T\mathbf{B}\right)^{-1}\mathbf{B}^T\mathbf{b}
\tag{2.88}
$$

22

where $\left(\mathbf{B}^T\mathbf{B}\right)^{-1}\mathbf{B}^T$ is the Moore-Penrose pseudoinverse of $\mathbf{B}$ and $\hat{\mathbf{g}}_{LS}$ is the LS intersection geolocation estimate of the emitter.
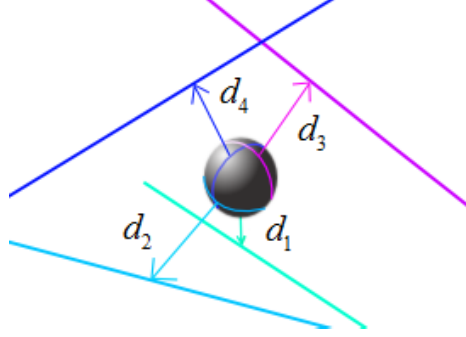
Figure 2.7: The least squares intersection is the point which is the closest approximation to the intersection of a set of lines of bearing. The location of the point is determined by minimizing the sum of the distances squared to all lines in the set [24, 27].

2.3.2.2 *Non-Linear Optimization.*

The NLO AOA geolocation method as described in [24, 27] is an iterative non-linear weighted least squares approach which has been shown to produce more accurate estimates of an emitter's location than the LS intersection method. The variance of the angular estimates from MUSIC are used as as the weighting factors for the collection of LOBs. NLO also produces the spatial covariance matrix of the geolocation estimate.

The iterative NLO process begins with the $\mathbf{r}_i$ vector from position $\mathbf{p}_i$ to a geolocation point $\mathbf{g}$ as defined in (2.80) with the bearing angles α_i and ε_i as defined in (2.82). The angles α_i and ε_i depend on the non-linear arctangent function. As shown in Figure 2.8, the arctangent function is approximately linear with unit slope in the range of $-\pi/4$ to $\pi/4$. In order to keep α_i and ε_i in the linear range of the arctangent function, the angles are converted to one of four local NLO reference frames shown in Figure 2.9. The frame

conversion process begins by using the following rules to determine which reference frame to use for the angle pair:

Frame 1: if $-\frac{\pi}{4} \leq \varepsilon_i \leq \frac{\pi}{4}$ and $-\frac{\pi}{4} \leq \alpha_i \leq \frac{\pi}{4}$ or $\frac{3\pi}{4} \leq \alpha_i \leq \frac{5\pi}{4}$

Frame 2: if $-\frac{\pi}{4} \leq \varepsilon_i \leq \frac{\pi}{4}$ and $\frac{\pi}{4} \leq \alpha_i \leq \frac{3\pi}{4}$ or $-\frac{3\pi}{4} \leq \alpha_i \leq -\frac{\pi}{4}$

Frame 3: if $|\varepsilon_i| > \frac{\pi}{4}$ and $-\frac{\pi}{4} \leq \alpha_i \leq \frac{\pi}{4}$ or $\frac{3\pi}{4} \leq \alpha_i \leq \frac{5\pi}{4}$

Frame 4: if $|\varepsilon_i| > \frac{\pi}{4}$ and $\frac{\pi}{4} < \alpha_i < \frac{3\pi}{4}$ or $-\frac{3\pi}{4} < \alpha_i < -\frac{\pi}{4}$

Once the appropriate reference frame has been identified, the angles $\alpha_{NLO,i}$ and $\varepsilon_{NLO,i}$, and the gradients with respect to $\mathbf{g}$, $\nabla_{\mathbf{g}}\alpha_{NLO,i}$ and $\nabla_{\mathbf{g}}\varepsilon_{NLO,i}$ are calculated using Equations (2.90)–(2.93) for the selected frame. The frame conversion process ensures the values of $\alpha_{NLO,i}$ and $\varepsilon_{NLO,i}$ lie in the $-\pi/4$ to $\pi/4$ linear range of the arctangent function and the appropriate gradients of each angle pair are used to construct the Jacobian matrix. The following term is defined for simplified notation:

$$\left\| \mathbf{r}_{i,xy} \right\|^2 = r_{i,x}{}^2 + r_{i,y}{}^2. \tag{2.89}$$
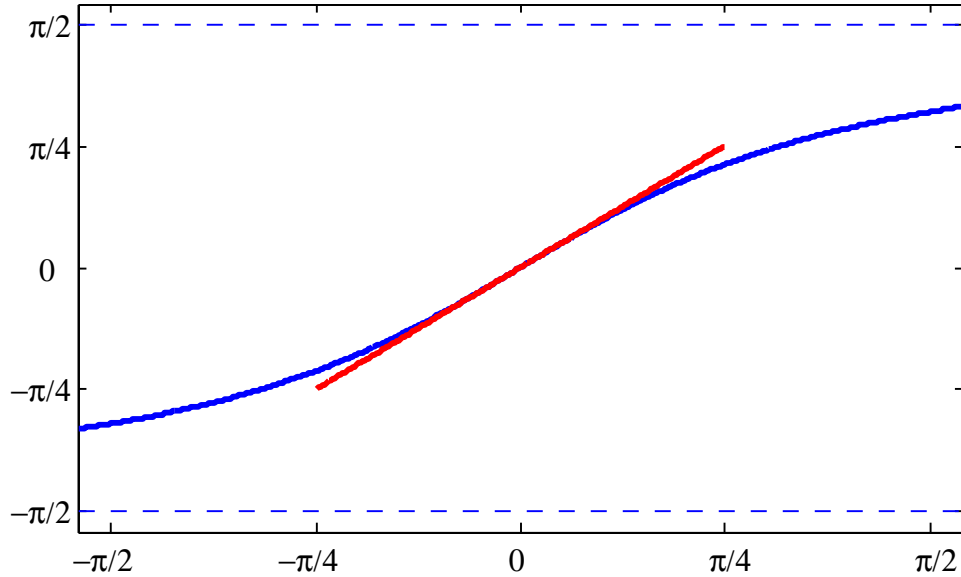
Figure 2.8: Linear approximation of the arctangent function between $-\pi/4$ and $\pi/4$ [27].
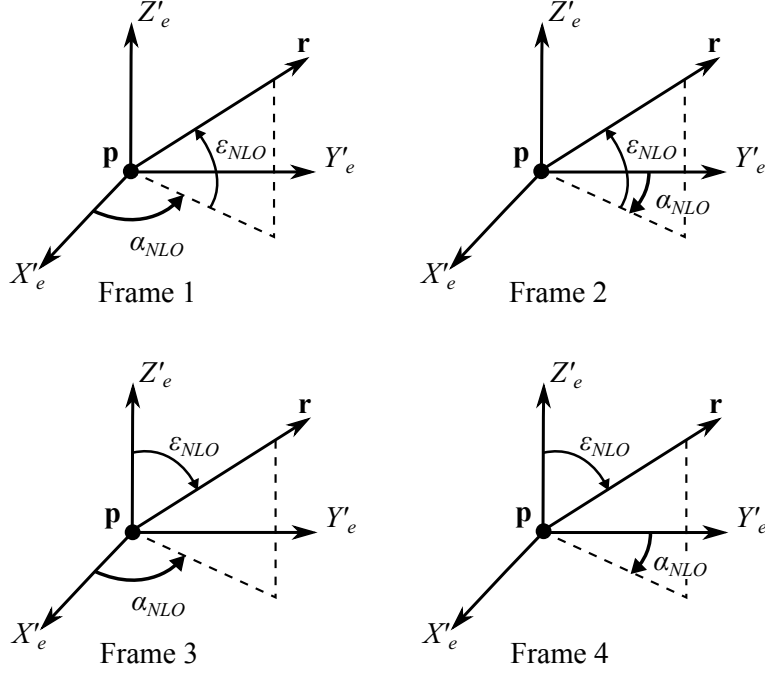
Figure 2.9: The four NLO reference frames [27].

Frame 1: $\varepsilon_{NLO,i}$ is measured from the $X'_e Y'_e$-plane and $\alpha_{NLO,i}$ is measured from the X'_e-axis.

$$\varepsilon_{NLO,i}(\mathbf{g}) = \text{atan2}\left(r_{i,z}, \sqrt{r_{i,x}^2 + r_{i,y}^2}\right)$$

$$\alpha_{NLO,i}(\mathbf{g}) = \text{atan2}\left(r_{i,y}, r_{i,x}\right)$$

$$\nabla_{\mathbf{g}}\varepsilon_{NLO,i} = \left[\begin{array}{ccc} -\dfrac{r_{i,x}r_{i,z}}{\|\mathbf{r}_i\|^2 \|\mathbf{r}_{i,xy}\|} & -\dfrac{r_{i,y}r_{i,z}}{\|\mathbf{r}_i\|^2 \|\mathbf{r}_{i,xy}\|} & \dfrac{\|\mathbf{r}_{i,xy}\|}{\|\mathbf{r}_i\|^2} \end{array} \right]$$

$$\nabla_{\mathbf{g}}\alpha_{NLO,i} = \left[\begin{array}{ccc} -\dfrac{r_{i,y}}{\|\mathbf{r}_{i,xy}\|^2} & \dfrac{r_{i,x}}{\|\mathbf{r}_{i,xy}\|^2} & 0 \end{array} \right]$$

(2.90)

The arctangent function with two arguments (atan2) is used to return angles in the range of $-\pi$ to π in order to preserve the quadrant of the angle.

Frame 2: $\varepsilon_{NLO,i}$ is measured from the $X'_e Y'_e$-plane and $\alpha_{NLO,i}$ is measured from the Y'_e-axis.

$$\varepsilon_{NLO,i}(\mathbf{g}) = \text{atan2}\left(r_{i,z}, \sqrt{r_{i,x}^2 + r_{i,y}^2}\right)$$

$$\alpha_{NLO,i}(\mathbf{g}) = \text{atan2}\left(r_{i,x}, r_{i,y}\right)$$

$$\nabla_{\mathbf{g}}\varepsilon_{NLO,i} = \left[\begin{array}{ccc} -\dfrac{r_{i,x}r_{i,z}}{\|\mathbf{r}_i\|^2 \|\mathbf{r}_{i,xy}\|} & -\dfrac{r_{i,y}r_{i,z}}{\|\mathbf{r}_i\|^2 \|\mathbf{r}_{i,xy}\|} & \dfrac{\|\mathbf{r}_{i,xy}\|}{\|\mathbf{r}_i\|^2} \end{array}\right]$$

$$\nabla_{\mathbf{g}}\alpha_{NLO,i} = \left[\begin{array}{ccc} \dfrac{r_{i,y}}{\|\mathbf{r}_{i,xy}\|^2} & -\dfrac{r_{i,x}}{\|\mathbf{r}_{i,xy}\|^2} & 0 \end{array}\right]$$

(2.91)

Frame 3: $\varepsilon_{NLO,i}$ is measured from the Z'_e-axis and $\alpha_{NLO,i}$ is measured from the X'_e-axis.

$$\varepsilon_{NLO,i}(\mathbf{g}) = \text{atan2}\left(\sqrt{r_{i,x}^2 + r_{i,y}^2}, r_{i,z}\right)$$

$$\alpha_{NLO,i}(\mathbf{g}) = \text{atan2}\left(r_{i,y}, r_{i,x}\right)$$

$$\nabla_{\mathbf{g}}\varepsilon_{NLO,i} = \left[\begin{array}{ccc} \dfrac{r_{i,x}r_{i,z}}{\|\mathbf{r}_i\|^2 \|\mathbf{r}_{i,xy}\|} & \dfrac{r_{i,y}r_{i,z}}{\|\mathbf{r}_i\|^2 \|\mathbf{r}_{i,xy}\|} & -\dfrac{\|\mathbf{r}_{i,xy}\|}{\|\mathbf{r}_i\|^2} \end{array}\right]$$

$$\nabla_{\mathbf{g}}\alpha_{NLO,i} = \left[\begin{array}{ccc} -\dfrac{r_{i,y}}{\|\mathbf{r}_{i,xy}\|^2} & \dfrac{r_{i,x}}{\|\mathbf{r}_{i,xy}\|^2} & 0 \end{array}\right]$$

(2.92)

Frame 4: $\varepsilon_{NLO,i}$ is measured from the Z'_e-axis and $\alpha_{NLO,i}$ is measured from the Y'_e-axis.

$$\varepsilon_{NLO,i}(\mathbf{g}) = \text{atan2}\left(\sqrt{r_{i,x}^2 + r_{i,y}^2}, r_{i,z}\right)$$

$$\alpha_{NLO,i}(\mathbf{g}) = \text{atan2}\left(r_{i,x}, r_{i,y}\right)$$

$$\nabla_{\mathbf{g}}\varepsilon_{NLO,i} = \left[\begin{array}{ccc} \dfrac{r_{i,x}r_{i,z}}{\|\mathbf{r}_i\|^2 \|\mathbf{r}_{i,xy}\|} & \dfrac{r_{i,y}r_{i,z}}{\|\mathbf{r}_i\|^2 \|\mathbf{r}_{i,xy}\|} & -\dfrac{\|\mathbf{r}_{i,xy}\|}{\|\mathbf{r}_i\|^2} \end{array}\right]$$

$$\nabla_{\mathbf{g}}\alpha_{NLO,i} = \left[\begin{array}{ccc} \dfrac{r_{i,y}}{\|\mathbf{r}_{i,xy}\|^2} & -\dfrac{r_{i,x}}{\|\mathbf{r}_{i,xy}\|^2} & 0 \end{array}\right]$$

(2.93)

The Jacobian matrix $\mathbf{J}(\mathbf{g})$ consists of the partial derivatives of $\varepsilon_{NLO,i}$ and $\alpha_{NLO,i}$ with respect to the x, y, and z components of $\mathbf{g}$ and is given as

$$\mathbf{J}(\mathbf{g}) = \begin{bmatrix} \dfrac{\partial \varepsilon_{NLO,1}}{\partial g_x} & \dfrac{\partial \varepsilon_{NLO,1}}{\partial g_y} & \dfrac{\partial \varepsilon_{NLO,1}}{\partial g_z} \\[2ex] \dfrac{\partial \alpha_{NLO,1}}{\partial g_x} & \dfrac{\partial \alpha_{NLO,1}}{\partial g_y} & \dfrac{\partial \alpha_{NLO,1}}{\partial g_z} \\[2ex] \vdots & \vdots & \vdots \\[2ex] \dfrac{\partial \varepsilon_{NLO,L}}{\partial g_x} & \dfrac{\partial \varepsilon_{NLO,L}}{\partial g_y} & \dfrac{\partial \varepsilon_{NLO,L}}{\partial g_z} \\[2ex] \dfrac{\partial \alpha_{NLO,L}}{\partial g_x} & \dfrac{\partial \alpha_{NLO,L}}{\partial g_y} & \dfrac{\partial \alpha_{NLO,L}}{\partial g_z} \end{bmatrix}_{2L\times 3} = \begin{bmatrix} \nabla_{\mathbf{g}}\varepsilon_{NLO,1} \\[2ex] \nabla_{\mathbf{g}}\alpha_{NLO,1} \\[2ex] \vdots \\[2ex] \nabla_{\mathbf{g}}\varepsilon_{NLO,L} \\[2ex] \nabla_{\mathbf{g}}\alpha_{NLO,L} \end{bmatrix}_{2L\times 3} .$$

(2.94)

The set of L estimated angle pairs from MUSIC in the appropriate reference frames are contained in the vector

$$\hat{\boldsymbol{\Omega}} = \begin{bmatrix} \hat{\varepsilon}_{NLO,1} \\ \hat{\alpha}_{NLO,1} \\ \vdots \\ \hat{\varepsilon}_{NLO,L} \\ \hat{\alpha}_{NLO,L} \end{bmatrix}_{2L \times 1} \tag{2.95}$$

and the angles as a function of $\mathbf{p}_i$ to $\mathbf{g}$ in the corresponding reference frames are

$$\boldsymbol{\Omega}(\mathbf{g}) = \begin{bmatrix} \varepsilon_{NLO,1}(\mathbf{g}) \\ \alpha_{NLO,1}(\mathbf{g}) \\ \vdots \\ \varepsilon_{NLO,L}(\mathbf{g}) \\ \alpha_{NLO,L}(\mathbf{g}) \end{bmatrix}_{2L \times 1}. \tag{2.96}$$

The iterative NLO process continues by using the LS geolocation estimate as the initial NLO estimate ($\hat{\mathbf{g}}_0 = \hat{\mathbf{g}}_{LS}$) in the Gauss-Newton iteration

$$\hat{\mathbf{g}}_{k+1} = \hat{\mathbf{g}}_k + \left(\mathbf{J}_k^T \Sigma_{\boldsymbol{\Omega}}^{-1} \mathbf{J}_k \right)^{-1} \mathbf{J}_k^T \Sigma_{\boldsymbol{\Omega}}^{-1} \Delta \boldsymbol{\Omega}_k \tag{2.97}$$

where

$$\Delta \boldsymbol{\Omega}_k = \hat{\boldsymbol{\Omega}} - \boldsymbol{\Omega}(\hat{\mathbf{g}}_k) \tag{2.98}$$

is the difference between the angles estimated from MUSIC and the angles from the k-th geolocation estimate, $\Sigma_{\boldsymbol{\Omega}}$ is the covariance of the MUSIC estimated angles which are used as the weighting factors, and

$$\mathbf{J}_k = \mathbf{J}(\hat{\mathbf{g}}_k) \tag{2.99}$$

is the Jacobian of the k-th geolocation estimate. Assuming that the angles estimated from MUSIC are independent and Gaussian distributed implies that the covariance matrix $\Sigma_{\boldsymbol{\Omega}}$ of the angles contains variances of the estimated angles along the diagonal.

27

Equation (2.97) is iterated until the difference between estimates has sufficiently converged ($\|\hat{\mathbf{g}}_{k+1} - \hat{\mathbf{g}}_k\| < \epsilon$) and the final iteration is taken as the NLO geolocation estimate of the emitter ($\hat{\mathbf{g}}_{NLO}$).

The spatial covariance of the k-th geolocation estimate is related to the angular covariance matrix through

$$\mathbf{\Sigma}_{\hat{\mathbf{g}}_k} = \left(\mathbf{J}_k^T \mathbf{\Sigma}_{\mathbf{\Omega}}^{-1} \mathbf{J}_k \right)^{-1} \tag{2.100}$$

which can be used to visualize the confidence surface using the method developed in Section 2.6. The NLO method will be shown to be the minimization of the maximum likelihood cost function in Section 3.3 and (2.100) will be shown to be equivalent to the Cramér-Rao lower bound developed in Section 3.4.

2.4 Maximum Likelihood Estimation, Gauss-Newton Iterations, and the Cramér-Rao Lower Bound

Consider a general known scalar nonlinear function $\mu(\boldsymbol{\theta})$ dependent on P scalar parameters

$$\boldsymbol{\theta} = \begin{bmatrix} \theta_1 & \cdots & \theta_P \end{bmatrix}^T. \tag{2.101}$$

It is desired to estimate the P unknown parameters from $N \geq P$ noisy observations of $\mu(\boldsymbol{\theta})$ such that

$$\mathbf{x} = \boldsymbol{\mu}(\boldsymbol{\theta}) + \mathbf{w} \tag{2.102}$$

where

$$\mathbf{x} = \begin{bmatrix} x_1 & \cdots & x_N \end{bmatrix}^T, \tag{2.103}$$

$$\boldsymbol{\mu}(\boldsymbol{\theta}) = \begin{bmatrix} \mu_1(\boldsymbol{\theta}) & \cdots & \mu_N(\boldsymbol{\theta}) \end{bmatrix}^T, \tag{2.104}$$

and

$$\mathbf{w} = \begin{bmatrix} w_1 & \cdots & w_N \end{bmatrix}^T. \tag{2.105}$$

The noise samples $\mathbf{w}$ are assumed to be independent real zero mean Gaussian random processes distributed as

$$\mathbf{w} \sim \mathcal{N}\left(\mathbf{0}, \mathbf{C_w}\right) \tag{2.106}$$

with covariance matrix

$$\mathbf{C_w} = \text{diag}\left[\sigma_{w,1}^2, \cdots, \sigma_{w,N}^2\right]_{N \times N}. \tag{2.107}$$

Due to the noise process, the N observations are distributed as

$$\mathbf{x} \sim \mathcal{N}\left(\boldsymbol{\mu}\left(\boldsymbol{\theta}\right), \mathbf{C_w}\right) \tag{2.108}$$

with the conditional Probability Density Function (PDF)

$$f\left(\mathbf{x} | \boldsymbol{\theta}\right) = \frac{1}{\sqrt{(2\pi)^N \det\left(\mathbf{C_w}\right)}} \exp\left(-\frac{1}{2} \sum_{n=1}^{N} \frac{\left(x_n - \mu_n\left(\boldsymbol{\theta}\right)\right)^2}{\sigma_{w,n}^2}\right). \tag{2.109}$$

The Maximum Likelihood Estimate (MLE) of the parameters $\hat{\boldsymbol{\theta}}_{MLE}$ is taken as the value of $\boldsymbol{\theta}$ which maximizes the likelihood function [28]

$$\hat{\boldsymbol{\theta}}_{MLE} = \arg\max_{\boldsymbol{\theta}} \left\{f\left(\mathbf{x} | \boldsymbol{\theta}\right)\right\} \tag{2.110}$$

and is equivalent to minimizing the term in the exponent of the PDF

$$\hat{\boldsymbol{\theta}}_{MLE} = \arg\min_{\boldsymbol{\theta}} \left\{\sum_{n=1}^{N} \frac{\left(x_n - \mu_n\left(\boldsymbol{\theta}\right)\right)^2}{\sigma_{w,n}^2}\right\}. \tag{2.111}$$

Writing (2.111) in matrix notation yields

$$\hat{\boldsymbol{\theta}}_{MLE} = \arg\min_{\boldsymbol{\theta}} \left\{\left[\mathbf{x} - \boldsymbol{\mu}\left(\boldsymbol{\theta}\right)\right]^T \mathbf{C_w}^{-1} \left[\mathbf{x} - \boldsymbol{\mu}\left(\boldsymbol{\theta}\right)\right]\right\}. \tag{2.112}$$

Equation (2.112) is a nonlinear weighted least squares minimization problem which can be solved using the Gauss-Newton method.

The iterative Gauss-Newton method uses a first order Taylor series expansion to linearize the function $\boldsymbol{\mu}\left(\boldsymbol{\theta}\right)$ about the value $\hat{\boldsymbol{\theta}}_k$ [28]. The resulting linear least squares problem is solved and the produced estimate $\hat{\boldsymbol{\theta}}_{k+1}$ is used to linearize $\boldsymbol{\mu}\left(\boldsymbol{\theta}\right)$ for the next

iteration. The method is said to converge to a solution when the difference between successive estimates is sufficiently small. The nonlinear function $\boldsymbol{\mu}(\boldsymbol{\theta})$ is approximated as a linear function about $\hat{\boldsymbol{\theta}}_k$ with the expansion

$$\boldsymbol{\mu}(\boldsymbol{\theta}) \approx \boldsymbol{\mu}\left(\hat{\boldsymbol{\theta}}_k\right) + \mathbf{J}\left(\hat{\boldsymbol{\theta}}_k\right)\left[\boldsymbol{\theta} - \hat{\boldsymbol{\theta}}_k\right] \tag{2.113}$$

where the Jacobian matrix of partial derivatives of $\boldsymbol{\mu}(\boldsymbol{\theta})$ with respect to the P unknown parameters is

$$\mathbf{J}(\boldsymbol{\theta}) = \begin{bmatrix} \frac{\partial \mu_1(\boldsymbol{\theta})}{\partial \theta_1} & \cdots & \frac{\partial \mu_1(\boldsymbol{\theta})}{\partial \theta_P} \\ \vdots & \ddots & \vdots \\ \frac{\partial \mu_N(\boldsymbol{\theta})}{\partial \theta_1} & \cdots & \frac{\partial \mu_N(\boldsymbol{\theta})}{\partial \theta_P} \end{bmatrix}_{N \times P} = \begin{bmatrix} \nabla_{\boldsymbol{\theta}} \mu_1(\boldsymbol{\theta}) \\ \vdots \\ \nabla_{\boldsymbol{\theta}} \mu_N(\boldsymbol{\theta}) \end{bmatrix}_{N \times P} \tag{2.114}$$

and the Jacobian at the current estimate $\hat{\boldsymbol{\theta}}_k$ is

$$\mathbf{J}_k = \mathbf{J}\left(\hat{\boldsymbol{\theta}}_k\right). \tag{2.115}$$

Substituting the linear approximation of (2.113) into (2.112) yields

$$\hat{\boldsymbol{\theta}}_{k+1} = \arg\min_{\boldsymbol{\theta}} \left\{ \left[\mathbf{x} - \left(\boldsymbol{\mu}\left(\hat{\boldsymbol{\theta}}_k\right) + \mathbf{J}_k\left[\boldsymbol{\theta} - \hat{\boldsymbol{\theta}}_k\right] \right) \right]^T \mathbf{C}_{\mathbf{w}}^{-1} \left[\mathbf{x} - \left(\boldsymbol{\mu}\left(\hat{\boldsymbol{\theta}}_k\right) + \mathbf{J}_k\left[\boldsymbol{\theta} - \hat{\boldsymbol{\theta}}_k\right] \right) \right] \right\} \tag{2.116}$$

which can be rearranged as [28, 29]

$$\hat{\boldsymbol{\theta}}_{k+1} = \arg\min_{\boldsymbol{\theta}} \left\{ \left[\underbrace{\mathbf{x} - \boldsymbol{\mu}\left(\hat{\boldsymbol{\theta}}_k\right) + \mathbf{J}_k\hat{\boldsymbol{\theta}}_k}_{=\mathbf{y}} - \mathbf{J}_k\boldsymbol{\theta} \right]^T \mathbf{C}_{\mathbf{w}}^{-1} \left[\underbrace{\mathbf{x} - \boldsymbol{\mu}\left(\hat{\boldsymbol{\theta}}_k\right) + \mathbf{J}_k\hat{\boldsymbol{\theta}}_k}_{=\mathbf{y}} - \mathbf{J}_k\boldsymbol{\theta} \right] \right\} \tag{2.117}$$

$$\hat{\boldsymbol{\theta}}_{k+1} = \arg\min_{\boldsymbol{\theta}} \left\{ [\mathbf{y} - \mathbf{J}_k\boldsymbol{\theta}]^T \mathbf{C}_{\mathbf{w}}^{-1} [\mathbf{y} - \mathbf{J}_k\boldsymbol{\theta}] \right\} \tag{2.118}$$

where all the terms of $\mathbf{y}$ are known quantities. Equation (2.118) is a weighted linear least squares minimization problem of $\boldsymbol{\theta}$ with the solution [28, 29]

$$\hat{\boldsymbol{\theta}}_{k+1} = \left(\mathbf{J}_k^T \mathbf{C}_{\mathbf{w}}^{-1} \mathbf{J}_k \right)^{-1} \mathbf{J}_k^T \mathbf{C}_{\mathbf{w}}^{-1} \mathbf{y}. \tag{2.119}$$

Back substituting for $\mathbf{y}$ produces

$$\hat{\boldsymbol{\theta}}_{k+1} = \left(\mathbf{J}_k^T \mathbf{C}_{\mathbf{w}}^{-1} \mathbf{J}_k \right)^{-1} \mathbf{J}_k^T \mathbf{C}_{\mathbf{w}}^{-1} \left[\mathbf{x} - \boldsymbol{\mu}\left(\hat{\boldsymbol{\theta}}_k\right) + \mathbf{J}_k\hat{\boldsymbol{\theta}}_k \right] \tag{2.120}$$

which after distribution of terms

$$\hat{\boldsymbol{\theta}}_{k+1} = \underbrace{\left(\mathbf{J}_k^T \mathbf{C}_\mathbf{w}^{-1} \mathbf{J}_k\right)^{-1} \mathbf{J}_k^T \mathbf{C}_\mathbf{w}^{-1} \mathbf{J}_k}_{=\mathbf{I}} \hat{\boldsymbol{\theta}}_k + \left(\mathbf{J}_k^T \mathbf{C}_\mathbf{w}^{-1} \mathbf{J}_k\right)^{-1} \mathbf{J}_k^T \mathbf{C}_\mathbf{w}^{-1} \left[\mathbf{x} - \boldsymbol{\mu}\left(\hat{\boldsymbol{\theta}}_k\right)\right] \qquad (2.121)$$

simplifies to the Gauss-Newton iteration [28, 29]

$$\hat{\boldsymbol{\theta}}_{k+1} = \hat{\boldsymbol{\theta}}_k + \left(\mathbf{J}_k^T \mathbf{C}_\mathbf{w}^{-1} \mathbf{J}_k\right)^{-1} \mathbf{J}_k^T \mathbf{C}_\mathbf{w}^{-1} \left[\mathbf{x} - \boldsymbol{\mu}\left(\hat{\boldsymbol{\theta}}_k\right)\right]. \qquad (2.122)$$

The Gauss-Newton method is said to converge when the norm of the difference between successive iteration estimates is below a specified threshold

$$\left\|\hat{\boldsymbol{\theta}}_{k+1} - \hat{\boldsymbol{\theta}}_k\right\| \leq \varepsilon \qquad (2.123)$$

and the final iteration is taken as the least squares estimate of the parameter vector $\hat{\boldsymbol{\theta}}_{LSE} = \hat{\boldsymbol{\theta}}_{k+1}$. When the observations are Gaussian distributed, the least squares estimate is also the MLE ($\hat{\boldsymbol{\theta}}_{MLE} = \hat{\boldsymbol{\theta}}_{LSE}$) [28].

An example of the Gauss-Newton iterative minimization method for 2 unknown parameters is shown in Figure 2.10, where the function

$$f(\boldsymbol{\theta}) = \theta_1^2 + \theta_1\theta_2 + \theta_2^2 \qquad (2.124)$$

has a global minimum at $(\theta_1, \theta_2) = (0, 0)$. The starting point for the first iteration step is $(\theta_1, \theta_2) = (-4, -4)$ and the norm of the difference from the 20th iteration to the global minimum is less than 10^{-4}.

The CRLB is defined [28] as the statistical lower bound on the variance of any unbiased estimator of $\hat{\boldsymbol{\theta}}$ such that

$$\begin{bmatrix} \text{var}\left(\hat{\theta}_1\right) & \cdots & \text{cov}\left(\hat{\theta}_1, \hat{\theta}_P\right) \\ \vdots & \ddots & \vdots \\ \text{cov}\left(\hat{\theta}_P, \hat{\theta}_1\right) & \cdots & \text{var}\left(\hat{\theta}_P\right) \end{bmatrix} \geq \text{CRLB}\left(\hat{\boldsymbol{\theta}}\right) \qquad (2.125)$$

and is equal to the inverse of the FIM

$$\text{CRLB}\left(\hat{\boldsymbol{\theta}}\right) = \mathbf{F}^{-1}(\boldsymbol{\theta}). \qquad (2.126)$$
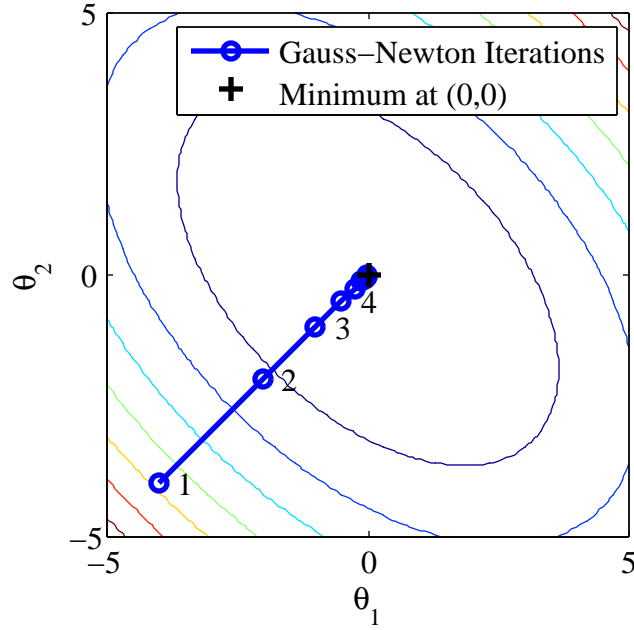
Figure 2.10: Example Gauss-Newton iterations for a 2 parameter minimization problem.

Each element of the FIM is defined as

$$\mathbf{F}_{i,j}(\boldsymbol{\theta}) = E\left[\left(\frac{\partial \mathcal{L}(\mathbf{x}|\boldsymbol{\theta})}{\partial \theta_i}\right)^T \left(\frac{\partial \mathcal{L}(\mathbf{x}|\boldsymbol{\theta})}{\partial \theta_j}\right)\right] \tag{2.127}$$

where the log-likelihood function is the natural logarithm of the PDF

$$\mathcal{L}(\mathbf{x}|\boldsymbol{\theta}) = \ln\left(f(\mathbf{x}|\boldsymbol{\theta})\right). \tag{2.128}$$

For Gaussian distributed observations, the FIM of (2.127) after differentiation and the expectation operation becomes [28]

$$\mathbf{F}_{i,j}(\boldsymbol{\theta}) = \sum_{n=1}^{N} \frac{1}{\sigma_{w,n}^2} \frac{\partial \mu_n(\boldsymbol{\theta})}{\partial \theta_i} \frac{\partial \mu_n(\boldsymbol{\theta})}{\partial \theta_j} \tag{2.129}$$

and can be expressed using matrix notation as

$$\mathbf{F}(\boldsymbol{\theta}) = \mathbf{J}^T(\boldsymbol{\theta}) \mathbf{C}_{\mathbf{w}}^{-1} \mathbf{J}(\boldsymbol{\theta}). \tag{2.130}$$

For a large enough number of samples N, the estimates of the MLE are shown to be asymptotically Gaussian distributed with variance equal to the CRLB such that [28]

$$\hat{\boldsymbol{\theta}} \overset{a}{\sim} \mathcal{N}\left(\boldsymbol{\theta}, \mathbf{F}^{-1}\left(\boldsymbol{\theta}\right)\right). \tag{2.131}$$

2.5 Single Sinusoidal Signal Parameter Estimation

This section derives the MLE and CRLB for estimating the parameters of a single sinusoidal signal from noisy observations. The derivation follows the example found in [28]. It is desired to estimate the normalized frequency, amplitude, and phase of a single complex exponential signal corrupted by AWGN. Consider N discrete samples of noisy observations of the signal

$$x[n] = \sigma_s \exp\left[j\left(2\pi f n + \phi\right)\right] + w[n] \tag{2.132}$$

where the noise is complex Gaussian distributed as

$$w[n] \sim C\left(\mathbf{0}, \sigma_w^2 \mathbf{I}\right) \tag{2.133}$$

and the signal parameters to be estimated are the normalized frequency f, amplitude σ_s, and phase ϕ

$$\boldsymbol{\alpha} = [f, \sigma_s, \phi]^T. \tag{2.134}$$

The normalized frequency ranges from 0 to 1 and is defined as $f = f_r/f_s$ where f_r is the received frequency of the signal and f_s is the sampling frequency, both in Hz. Defining the non-linear function

$$\mu[n] = \sigma_s \exp\left[j\left(2\pi f n + \phi\right)\right] \tag{2.135}$$

the PDF of the observed signal $\mathbf{x}$ conditioned on the parameters $\boldsymbol{\alpha}$ is [28]

$$f\left(\mathbf{x}|\boldsymbol{\alpha}\right) = \prod_{n=1}^{N} \frac{1}{\pi\sigma_w^2} \exp\left(-\frac{1}{\sigma_w^2}|x[n] - \mu[n]|^2\right) = \frac{1}{(\pi\sigma_w^2)^N} \exp\left(-\frac{1}{\sigma_w^2}\sum_{n=1}^{N}|x[n] - \mu[n]|^2\right). \tag{2.136}$$

33

The normalized frequency MLE is shown [28, 30, 31] to be

$$\hat{f}_{MLE} = \arg \max_f \left| \frac{1}{N} \sum_{n=1}^{N} x[n] \exp(-j2\pi f n) \right|^2 \qquad (2.137)$$

which is the location of the maximum value of the Discrete Fourier Transform (DFT) of **x**

$$\hat{f}_{MLE} = \arg \max_f \left| \frac{1}{N} \text{DFT}[\mathbf{x}] \right|^2. \qquad (2.138)$$

Similarity, [28, 30] the amplitude MLE is the value of the DFT evaluated at $\hat{f}_{MLE}$

$$\hat{\sigma}_{s,MLE} = \left| \frac{1}{N} \text{DFT}[\mathbf{x}] \right|_{f=\hat{f}_{MLE}}. \qquad (2.139)$$

An example of the frequency and amplitude MLEs is shown in Figure 2.11.
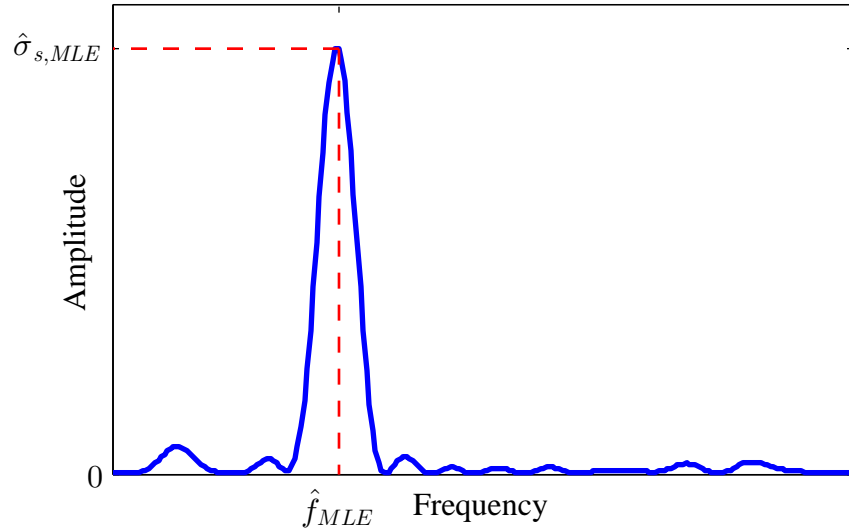
Figure 2.11: The normalized frequency and amplitude MLEs of a single complex exponential signal from noisy observations are the location of the maximum value and the maximum value of the DFT of the observations.

The FIM for complex AWGN is given as [28]

$$\mathbf{F}_{i,j}(\boldsymbol{\alpha}) = \frac{2}{\sigma_w^2} \text{Re} \left[\sum_{n=1}^{N} \frac{\partial \mu^H[n]}{\partial \alpha_i} \frac{\partial \mu[n]}{\partial \alpha_j} \right] \qquad (2.140)$$

34

and the partial derivatives of $\mu[n]$ with respect to the normalized frequency, amplitude, and phase are

$$\frac{\partial \mu[n]}{\partial f} = j2\pi n \sigma_s \exp\left[j(2\pi fn + \phi)\right] \tag{2.141}$$

$$\frac{\partial \mu[n]}{\partial \sigma_s} = \exp\left[j(2\pi fn + \phi)\right] \tag{2.142}$$

$$\frac{\partial \mu[n]}{\partial \phi} = j\sigma_s \exp\left[j(2\pi fn + \phi)\right]. \tag{2.143}$$

Evaluating (2.140) yields

$$\mathbf{F}(\alpha) = \frac{2}{\sigma_w^2} \begin{bmatrix} \sigma_s^2(2\pi)^2 \sum_{n=1}^{N} n^2 & 0 & \sigma_s^2 2\pi \sum_{n=1}^{N} n \\ 0 & N & 0 \\ \sigma_s^2 2\pi \sum_{n=1}^{N} n & 0 & N\sigma_s^2 \end{bmatrix}. \tag{2.144}$$

Utilizing the following summation identities [28],

$$\sum_{n=1}^{N} n = \frac{N(N+1)}{2} \tag{2.145}$$

$$\sum_{n=1}^{N} n^2 = \frac{N(N+1)(2N+1)}{6} \tag{2.146}$$

produces the CRLB on unbiased estimates of the single sinusoidal signal parameters [28]

$$\text{CRLB}(\alpha) = \mathbf{F}^{-1}(\alpha) = \begin{bmatrix} \frac{6}{\eta(2\pi)^2 N(N^2-1)} & 0 & \frac{-3}{\eta 2\pi N(N-1)} \\ 0 & \frac{\sigma_w^2}{2N} & 0 \\ \frac{-3}{\eta 2\pi N(N-1)} & 0 & \frac{2N+1}{\eta N(N-1)} \end{bmatrix}. \tag{2.147}$$

The normalized frequency, amplitude, and phase CRLBs are therefore

$$\text{var}\left(\hat{f}\right) \geq \frac{6}{\eta(2\pi)^2 N(N^2-1)} \tag{2.148}$$

$$\text{var}\left(\hat{\sigma}_s\right) \geq \frac{\sigma_w^2}{2N} \tag{2.149}$$

$$\text{var}\left(\hat{\phi}\right) \geq \frac{2N+1}{\eta N(N-1)}. \tag{2.150}$$

The variance of the received frequency f_r in Hz^2 is

$$\text{var}\left(\hat{f}_r\right) \geq \frac{6f_s^2}{\eta(2\pi)^2 N(N^2-1)}. \tag{2.151}$$

2.6 Confidence Surfaces

Using a single unbiased Gaussian distributed estimate $\hat{\boldsymbol{\theta}}$ of a $k \times 1$ vector parameter $\boldsymbol{\theta}$ with $k \times k$ covariance matrix $\mathbf{C}_{\hat{\boldsymbol{\theta}}}$,

$$\hat{\boldsymbol{\theta}} \sim \mathcal{N}\left(\boldsymbol{\theta}, \mathbf{C}_{\hat{\boldsymbol{\theta}}}\right) \tag{2.152}$$

it is possible to define a k-dimensional surface centered at the estimate $\hat{\boldsymbol{\theta}}$ which has the probability P of containing the value of the $\boldsymbol{\theta}$ parameter. The k-dimensional confidence surface is defined by the quadratic relation

$$\left(\boldsymbol{\theta} - \hat{\boldsymbol{\theta}}\right)^T \mathbf{C}_{\hat{\boldsymbol{\theta}}}^{-1} \left(\boldsymbol{\theta} - \hat{\boldsymbol{\theta}}\right) = c^2 \tag{2.153}$$

where c is a constant to be determined that defines a contour of constant probability. The probability P that the value $\boldsymbol{\theta}$ is contained within the confidence surface centered at the estimate $\hat{\boldsymbol{\theta}}$ is given as [28, 32]

$$P = \Pr\left\{\left(\boldsymbol{\theta} - \hat{\boldsymbol{\theta}}\right)^T \mathbf{C}_{\hat{\boldsymbol{\theta}}}^{-1} \left(\boldsymbol{\theta} - \hat{\boldsymbol{\theta}}\right) \leq c^2\right\}. \tag{2.154}$$

Letting $u = \left(\boldsymbol{\theta} - \hat{\boldsymbol{\theta}}\right)^T \mathbf{C}_{\hat{\boldsymbol{\theta}}}^{-1} \left(\boldsymbol{\theta} - \hat{\boldsymbol{\theta}}\right)$, since $\hat{\boldsymbol{\theta}}$ is Gaussian distributed with covariance $\mathbf{C}_{\hat{\boldsymbol{\theta}}}$ and u is a quadratic sum of Gaussian random variables, u is a Chi-squared random variable with k degrees of freedom [28, 32]

$$u \sim \chi_k^2. \tag{2.155}$$

The PDF of the Chi-squared distribution is given as [33]

$$\chi_k^2(u) = \frac{e^{-u/2}u^{k/2-1}}{2^{k/2}\Gamma(k/2)} \tag{2.156}$$

where the complete Gamma function is defined as [33]

$$\Gamma(\alpha) = \int_0^{\infty} e^{-t}t^{\alpha-1}dt. \tag{2.157}$$

Using the Cumulative Distribution Function (CDF) of the Chi-squared distribution to evaluate (2.154), the probability P, constant c, and dimension k are related through [32]

$$P = \Pr\left\{u \leq c^2\right\} = \frac{\gamma\left(\frac{k}{2}, \frac{c^2}{2}\right)}{\Gamma\left(\frac{k}{2}\right)} \tag{2.158}$$

where the lower incomplete Gamma function is defined as [33]

$$\gamma(\alpha, \beta) = \int_0^\beta e^{-t} t^{\alpha-1} dt. \tag{2.159}$$

When $k = 2$ dimensions, u is exponentially distributed and the constant c can be defined in terms of the probability P using [28, 32]

$$c = \sqrt{2 \ln\left(\frac{1}{1-P}\right)}. \tag{2.160}$$

Using c and (2.153), the resulting surface defines a confidence ellipse centered at $\hat{\theta}$ with probability P of containing the θ value as shown in Figure 2.12.

When $k = 3$ dimensions, a value of $c \approx 2.7959$ with (2.158) yields $P = 0.95$, and is a 95% confidence ellipsoid surface defined by

$$\left(\theta - \hat{\theta}\right)^T \mathbf{C}_{\hat{\theta}}^{-1} \left(\theta - \hat{\theta}\right) = (2.7959)^2. \tag{2.161}$$
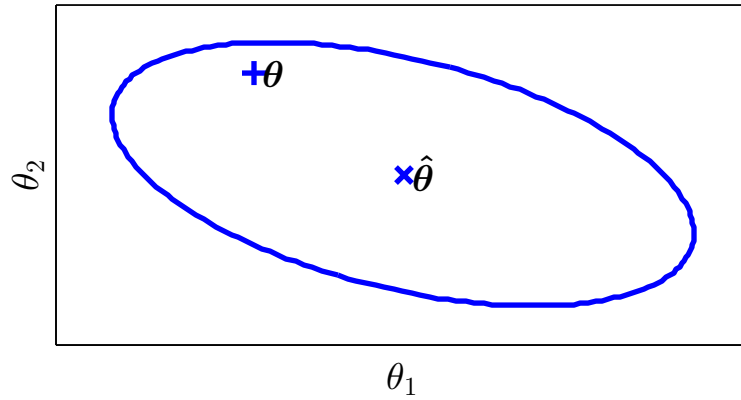

Figure 2.12: 2D confidence ellipse centered at $\hat{\theta}$ with a 95% probability of containing θ.

III. Methodology

This chapter outlines the analysis scenario in Section 3.1, defines the relationship between reference frames in Section 3.2, derives the geolocation maximum likelihood estimators in Section 3.3, derives the Cramér-Rao lower bound on geolocation estimates in Section 3.4, and details the geolocation performance analysis in Section 3.5.

3.1 Scenario Overview

Consider a single RF SOI emitter located at the Air Force Institute of Technology (Latitude: 39.782° N, Longitude: 84.083° W, Altitude: 0 m) transmitting a 1315 MHz narrowband signal. The signal is received by a single 6U CubeSat in a 60° inclined 450 km circular LEO over the SOI. The assumed CubeSat geolocation payload consists of a 4 element UCA tuned to 1315 MHz and calibrated to perform AOA measurements. Each antenna array element is connected to a RF receiver for filtering, demodulation, and digitizing the received signals from the antennas. The 4 payload receivers are assumed to be frequency and phase coherent with sufficient bandwidth and sampling rate to process the received signals. Estimation of signal parameters from the received signals, running geolocation algorithms, and interfacing with other CubeSat subsystems is accomplished through a dedicated payload processor with sufficient processing capability. The CubeSat is also assumed to have a Guidance Navigation and Control (GNC) subsystem consisting of an onboard Global Positioning System (GPS) receiver to provide position and velocity information, and an Attitude Determination and Control System (ADCS) to provide attitude information and maintain a Local Vertical Local Horizontal (LVLH) orientation over the RF SOI. The assumed payload functional diagram is shown in Figure 3.1.

This analysis scenario considers only a single RF emitter with no co-channel interference. It is assumed that the signals collected from multiple RF emitters have been
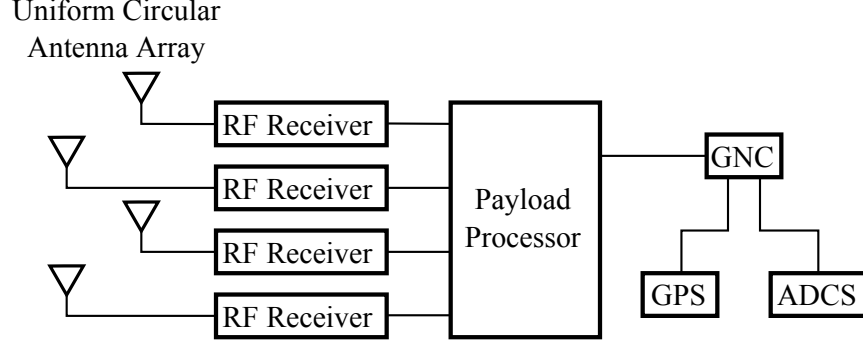
Figure 3.1: Assumed CubeSat geolocation payload consisting of a 4 element UCA, 4 frequency and phase coherent RF receivers, and a payload processor interfaced with the CubeSat GNC subsystem.

properly segregated such that the estimated signal parameters used as inputs into the geolocation algorithms correspond to a single emitter. Methods for data association and segregation of multiple emitters with co-channel interference, as well as the implementation of specific RF receiver and payload processor design, are beyond the scope of this thesis.

The payload UCA shown in Figure 3.2 consists of 4 antenna elements evenly spaced around a circle on the nadir face of a 6U CubeSat. The UCA elements lie in the *xy*-plane and are centered at the origin of the sensor reference frame. Using (2.5) the wavelength of the 1315 MHz SOI is 0.228 m, and the diameter of the UCA is 0.114 m to satisfy the $\lambda_r/2$ antenna element spacing requirement of MUSIC. The counterclockwise angles of the antenna elements from the *x*-axis are: $\gamma_1 = 45°$, $\gamma_2 = 135°$, $\gamma_3 = 225°$, and $\gamma_4 = 315°$. It is assumed that the payload antenna array is properly calibrated with a uniform hemispherical gain pattern to receive the SOI planar EM wavefront. Implementation specific antenna design to include variable gain patterns, mutual coupling, calibration, and other antenna parameters, are beyond the scope of this thesis.
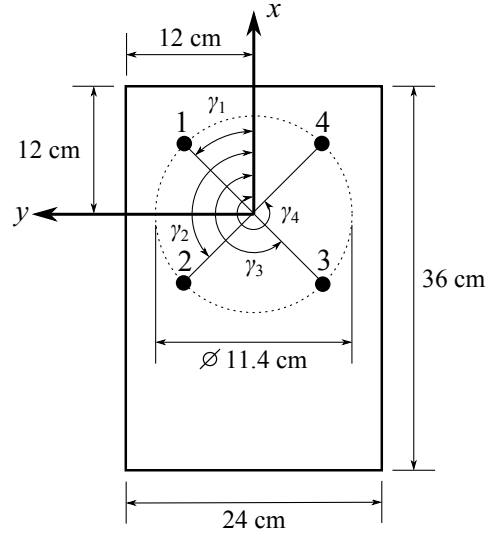
Figure 3.2: Assumed geolocation payload 4 element UCA located on the nadir face of a 6U CubeSat.

The analysis scenario geometry is shown in Figures 3.3 and 3.4 where the RF SOI is located at position **g**. The gain pattern of the RF SOI is modeled as a uniform cone centered at **g** and extending 10° above the horizon with an 80° cone half angle. The single 6U CubeSat receiver platform in a 60° inclined, 450 km altitude, circular orbit receives the RF SOI at ECEF positions $\mathbf{p}_i$ and velocities $\mathbf{v}_i$ while traveling through the cone. Different types of RF emitters are simulated by varying the number of signal collects, the timing between signal collects, and the SNR of the received signals. Emitter types and other simulation variables are described in Section 3.5.
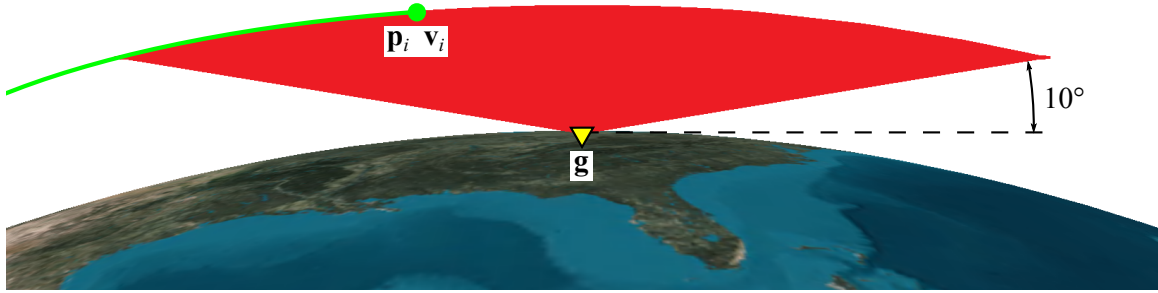
Figure 3.3: Profile view of the analysis scenario geometry. The RF SOI gain pattern is an 80° half angle cone centered at **g**. The single moving platform receives the SOI at positions **p**$_i$ and velocities **v**$_i$.

Figure 3.4: Top-down view of the analysis scenario geometry.

3.2 Reference Frame Transformations

The relationships between the local reference frames used in this thesis are shown in Figure 3.5. The reference frame transformation process uses the points **p** and **g** with the attitude of the CubeSat to determine the azimuth $\phi(\mathbf{g})$ and elevation $\theta(\mathbf{g})$ angles in the sensor reference frame as a function of geolocation point **g**. The expressions for $\phi(\mathbf{g})$ and $\theta(\mathbf{g})$ are used to derive the MLE and CRLB for AOA geolocation in Sections 3.3 and 3.4.
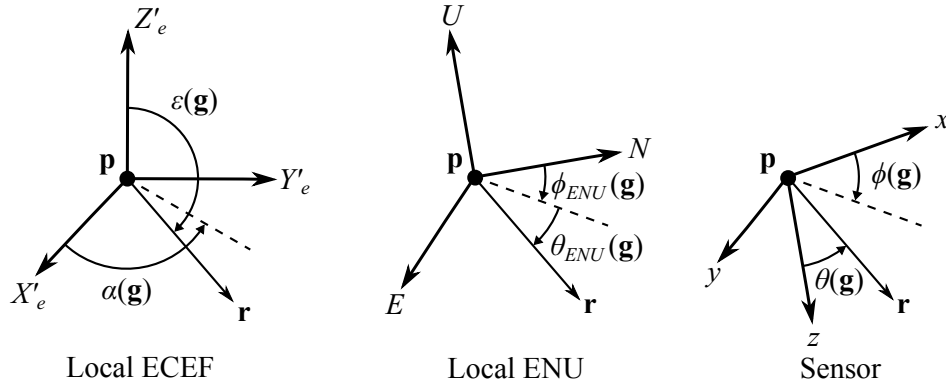

Figure 3.5: Relationships between the local reference frames.

3.2.1 ECEF to Local ECEF Reference Frame Transformation.

Using the LOB vector $\mathbf{r} = \mathbf{g} - \mathbf{p}$ in ECEF coordinates between the receiver position **p** and geolocation point **g**, the corresponding azimuth and elevation angles in the local ECEF frame are

$$\alpha(\mathbf{g}) = \operatorname{atan2}\left(g_y - p_y, g_x - p_x\right)$$
$$\varepsilon(\mathbf{g}) = \operatorname{atan2}\left(\sqrt{(g_x - p_x)^2 + (g_y - p_y)^2}, g_z - p_z\right)$$

(3.1)

where $\alpha(\mathbf{g})$ is measured down from the local Z'_e-axis and ε is measured counterclockwise from the local X'_e-axis. The local ECEF LOB vector Cartesian coordinates are

$$
\begin{aligned}
X'_e &= \sin\left(\varepsilon\left(\mathbf{g}\right)\right)\cos\left(\alpha\left(\mathbf{g}\right)\right) \\
Y'_e &= \sin\left(\varepsilon\left(\mathbf{g}\right)\right)\sin\left(\alpha\left(\mathbf{g}\right)\right) \\
Z'_e &= \cos\left(\varepsilon\left(\mathbf{g}\right)\right)
\end{aligned}
\tag{3.2}
$$

which can be expressed in terms of $\mathbf{p}$ and $\mathbf{g}$ as

$$
\begin{aligned}
X'_e &= \frac{\sqrt{(g_x-p_x)^2+(g_y-p_y)^2}}{(g_z-p_z)\sqrt{\frac{(g_x-p_x)^2+(g_y-p_y)^2}{(g_z-p_z)^2}+1}\sqrt{\frac{(g_y-p_y)^2}{(g_x-p_x)^2}+1}} \\
Y'_e &= \frac{(g_y-p_y)\sqrt{(g_x-p_x)^2+(g_y-p_y)^2}}{(g_x-p_x)(g_z-p_z)\sqrt{\frac{(g_x-p_x)^2+(g_y-p_y)^2}{(g_z-p_z)^2}+1}\sqrt{\frac{(g_y-p_y)^2}{(g_x-p_x)^2}+1}} \\
Z'_e &= \frac{1}{\sqrt{\frac{(g_x-p_x)^2+(g_y-p_y)^2}{(g_z-p_z)^2}+1}}.
\end{aligned}
\tag{3.3}
$$

3.2.2 Local ECEF to Local ENU Reference Frame Transformation.

The local ENU coordinates are obtained through the Direction Cosine Matrix (DCM) operation on the local ECEF coordinates [34]

$$
\begin{bmatrix} E \\ N \\ U \end{bmatrix} = \mathbf{R}_{ENU/ECEF}\left(\varphi_g, \lambda_g\right)\begin{bmatrix} X'_e \\ Y'_e \\ Z'_e \end{bmatrix}
\tag{3.4}
$$

where the DCM $\mathbf{R}_{ENU/ECEF}\left(\varphi_g, \lambda_g\right)$ is a function of the geodetic latitude φ_g and geodetic longitude λ_g of point $\mathbf{p}$,

$$
\mathbf{R}_{ENU/ECEF}\left(\varphi_g, \lambda_g\right) = \begin{bmatrix} -\sin\left(\lambda_g\right) & \cos\left(\lambda_g\right) & 0 \\ -\sin\left(\varphi_g\right)\cos\left(\lambda_g\right) & -\sin\left(\varphi_g\right)\sin\left(\lambda_g\right) & \cos\left(\varphi_g\right) \\ \cos\left(\varphi_g\right)\cos\left(\lambda_g\right) & \cos\left(\varphi_g\right)\sin\left(\lambda_g\right) & \sin\left(\varphi_g\right) \end{bmatrix}.
\tag{3.5}
$$

The local ENU coordinates in terms of the local ECEF coordinates are

$$
\begin{aligned}
E &= -X'_e\sin\left(\lambda_g\right) + Y'_e\cos\left(\lambda_g\right) \\
N &= -X'_e\sin\left(\varphi_g\right)\cos\left(\lambda_g\right) - Y'_e\sin\left(\varphi_g\right)\sin\left(\lambda_g\right) + Z'_e\cos\left(\varphi_g\right) \\
U &= X'_e\cos\left(\varphi_g\right)\cos\left(\lambda_g\right) + Y'_e\cos\left(\varphi_g\right)\sin\left(\lambda_g\right) + Z'_e\sin\left(\varphi_g\right).
\end{aligned}
\tag{3.6}
$$

The local ENU azimuth angle $\phi_{ENU}(\mathbf{g})$ is measured clockwise from the N-axis and local elevation angle $\theta_{ENU}(\mathbf{g})$ is measured up from the NE-plane

$$
\begin{aligned}
\phi_{ENU}(\mathbf{g}) &= \text{atan2}(E, N) \\
\theta_{ENU}(\mathbf{g}) &= \text{atan2}\left(U, \sqrt{E^2 + N^2}\right).
\end{aligned}
\tag{3.7}
$$

The expressions for $\phi_{ENU}(\mathbf{g})$ and $\theta_{ENU}(\mathbf{g})$ in terms of $\mathbf{p}$ and $\mathbf{g}$ are obtained by substituting (3.3) and (3.6) into (3.7).

3.2.3   *Local ENU to Sensor Reference Frame Transformation.*

It is assumed that the CubeSat is in a LVLH orientation over the RF SOI where the x-axis of the sensor frame is aligned with the velocity vector of the CubeSat and the z-axis points towards nadir in the opposite direction of the U-axis. The xy-plane of the sensor frame is coplanar with the NE-plane of the local ENU reference frame. The relationship between the local ENU and sensor reference frames is shown in Figure 3.6 and the expressions of the azimuth $\phi(\mathbf{g})$ and elevation $\theta(\mathbf{g})$ angles in the sensor reference frame are

$$
\begin{aligned}
\phi(\mathbf{g}) &= \phi_{ENU}(\mathbf{g}) - \phi_{North} \\
\theta(\mathbf{g}) &= \theta_{ENU}(\mathbf{g}) + \frac{\pi}{2}
\end{aligned}
\tag{3.8}
$$

where ϕ_{North} is the angle between the x-axis and N-axis. If the CubeSat is not in a LVLH orientation, then the appropriate transformation from the ENU to the sensor frame will apply.

3.2.4   *Sensor Reference Frame to ECEF Coordinate System Transformation.*

The MUSIC algorithm described in Section 2.2 estimates the azimuth and elevation angles of the received SOI which are used to generate a LOB from $\mathbf{p}$ in the direction of the estimated angles $\hat{\phi}$ and $\hat{\theta}$. In order geolocate the RF SOI, the LOB is transformed from the sensor reference frame to the ECEF coordinate system. The process begins by
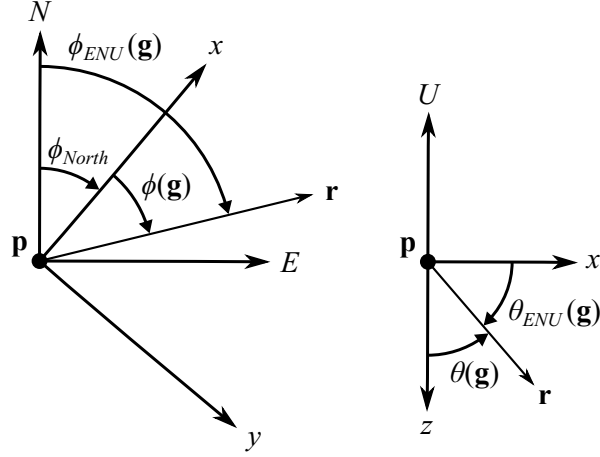
Figure 3.6: Relationship between the local ENU and sensor reference frames assuming a LVLH CubeSat orientation.

transforming the estimated angles in the senor frame to the local ENU reference frame,

$$
\begin{aligned}
\hat{\phi}_{ENU} &= \hat{\phi} + \phi_{North} + \phi_{error} \\
\hat{\theta}_{ENU} &= \hat{\theta} - \frac{\pi}{2} + \theta_{error}
\end{aligned}
\tag{3.9}
$$

where the attitude knowledge error is expressed in terms of ϕ_{error} and θ_{error}. The local ENU Cartesian components are

$$
\begin{aligned}
\hat{E} &= \cos\left(\hat{\theta}_{ENU}\right) \sin\left(\hat{\phi}_{ENU}\right) \\
\hat{N} &= \cos\left(\hat{\theta}_{ENU}\right) \cos\left(\hat{\phi}_{ENU}\right) \\
\hat{U} &= \sin\left(\hat{\theta}_{ENU}\right).
\end{aligned}
\tag{3.10}
$$

The local ECEF Cartesian components are related to the local ENU Cartesian components through

$$
\begin{bmatrix} \hat{X}'_e \\ \hat{Y}'_e \\ \hat{Z}'_e \end{bmatrix} = \mathbf{R}_{ECEF/ENU}\left(\varphi_g, \lambda_g\right) \begin{bmatrix} \hat{E} \\ \hat{N} \\ \hat{U} \end{bmatrix}
\tag{3.11}
$$

where $\mathbf{R}_{ECEF/ENU}\left(\varphi_g, \lambda_g\right) = \left[\mathbf{R}_{ENU/ECEF}\left(\varphi_g, \lambda_g\right)\right]^T$ is the DCM from the local ENU to local ECEF reference frame. The local ECEF estimated azimuth and elevation angles are

$$
\begin{aligned}
\hat{\alpha} &= \operatorname{atan2}\left(\hat{Y}'_e, \hat{X}'_e\right) \\
\hat{\varepsilon} &= \operatorname{atan2}\left(\sqrt{\left(\hat{X}'_e\right)^2 + \left(\hat{Y}'_e\right)^2}, \hat{Z}'_e\right).
\end{aligned}
\tag{3.12}
$$

The i-th estimated LOB in the ECEF coordinate system is the vector $\hat{\mathbf{r}}_i$ originating from the position $\hat{\mathbf{p}}_i$ and pointing the $\hat{\alpha}_i$ and $\hat{\varepsilon}_i$ direction,

$$
\hat{\mathbf{r}}_i = \hat{\mathbf{p}}_i + \begin{bmatrix} \hat{X}'_{i,e} \\ \hat{Y}'_{i,e} \\ \hat{Z}'_{i,e} \end{bmatrix}
\tag{3.13}
$$

where $\hat{\mathbf{p}}_i = \mathbf{p}_i + \mathbf{p}_{error}$ is the estimated position with position knowledge error.

3.3 Geolocation Maximum Likelihood Estimators

This section develops the geolocation MLEs used in this thesis. From the received signals, the collection of AOA and Frequency of Arrival (FOA) measurements are used to estimate the location $\hat{\mathbf{g}}$ of the RF SOI. From (2.7), the received FOA in Hz consists of the RF carrier frequency and Doppler shifted frequency

$$
f_r\left(\mathbf{g}\right) = f_c + f_d\left(\mathbf{g}\right).
\tag{3.14}
$$

The Doppler frequency

$$
f_d\left(\mathbf{g}\right) = -\frac{f_c}{c}\dot{d}\left(\mathbf{g}\right)
\tag{3.15}
$$

is a function of the position $\mathbf{g}$ of the SOI along with the position and velocity of the receiver where $\dot{d}\left(\mathbf{g}\right)$ is the range rate of the distance between $\mathbf{p}$ and $\mathbf{g}$. Letting $\mathbf{v} = \begin{bmatrix} v_x & v_y & v_z \end{bmatrix}^T$ be the $X_e Y_e Z_e$ components of the receiver velocity in the ECEF coordinate system, the range rate is given as [35, 36]

$$
\dot{d}\left(\mathbf{g}\right) = \frac{\mathbf{v}^T \mathbf{r}\left(\mathbf{g}\right)}{\|\mathbf{r}\left(\mathbf{g}\right)\|} = \left[\frac{v_x\left(p_x - g_x\right) + v_y\left(p_y - g_y\right) + v_z\left(p_z - g_z\right)}{\sqrt{\left(p_x - g_x\right)^2 + \left(p_y - g_y\right)^2 + \left(p_z - g_z\right)^2}}\right].
\tag{3.16}
$$

If f_c is assumed to be known, the observed frequency after demodulation consists solely of the Doppler frequency shift and the FOA of the i-th signal collect is

$$f_{d,i}(\mathbf{g}) = -\frac{f_c}{c}\left[\frac{v_{x,i}\left(p_{x,i}-g_x\right)+v_{y,i}\left(p_{y,i}-g_y\right)+v_{z,i}\left(p_{z,i}-g_z\right)}{\sqrt{\left(p_{x,i}-g_x\right)^2+\left(p_{y,i}-g_y\right)^2+\left(p_{z,i}-g_z\right)^2}}\right]. \tag{3.17}$$

Consider a single moving receiver in the ECEF coordinate system at position $\mathbf{p}$ and velocity $\mathbf{v}$ receiving signals from a single RF SOI located at $\mathbf{g}$. At each signal collect, the angles and frequency of arrival are estimated from the received signal. Let the i-th set of estimated parameters be

$$\hat{\Omega}_i = \begin{bmatrix} \hat{\theta}_{ENU,i} \\ \hat{\phi}_{ENU,i} \\ \hat{f}_{d,i} \end{bmatrix} \tag{3.18}$$

where $\hat{\theta}_{ENU,i}$ and $\hat{\phi}_{ENU,i}$ are the estimated elevation and azimuth angles in the ENU reference frame to account for attitude knowledge error, and $\hat{f}_{d,i}$ is the estimated received frequency of the signal. The true parameter values as a function of $\mathbf{p}_i$, $\mathbf{v}_i$ and $\mathbf{g}$ are

$$\Omega_i(\mathbf{g}) = \begin{bmatrix} \theta_{ENU,i}(\mathbf{g}) \\ \phi_{ENU,i}(\mathbf{g}) \\ f_{d,i}(\mathbf{g}) \end{bmatrix} \tag{3.19}$$

where $\theta_{ENU,i}(\mathbf{g})$ and $\phi_{ENU,i}(\mathbf{g})$ are defined in (3.7), and $f_{d,i}(\mathbf{g})$ is defined in (3.17). The variance of the estimated parameters with the additional attitude and frequency knowledge errors are contained in the covariance matrix of the i-th set of parameters,

$$\mathbf{C}_{\hat{\Omega},i} = \begin{bmatrix} \sigma_{\hat{\theta},i}^2 + \sigma_{\text{attitude},i}^2 & 0 & 0 \\ 0 & \sigma_{\hat{\phi},i}^2 + \sigma_{\text{attitude},i}^2 & 0 \\ 0 & 0 & \sigma_{\hat{f},i}^2 + \sigma_{\text{frequency},i}^2 \end{bmatrix} \tag{3.20}$$

where $\sigma_{\hat{\theta},i}^2$ is the elevation error variance, $\sigma_{\hat{\phi},i}^2$ is the azimuth error variance, $\sigma_{\hat{f},i}^2$ is the frequency error variance, $\sigma_{\text{attitude},i}^2$ is the attitude knowledge error variance, and $\sigma_{\text{frequency},i}^2$ is the frequency knowledge error variance.

If each set of estimated parameters are Gaussian distributed such that

$$\hat{\Omega}_i \sim \mathcal{N}\left(\Omega_i\left(\mathbf{g}\right), \mathbf{C}_{\hat{\Omega},i}\right) \tag{3.21}$$

then the PDF of a collection of L sets of parameters conditioned on $\mathbf{g}$ is

$$f\left(\hat{\Omega}_1, \cdots, \hat{\Omega}_L \middle| \mathbf{g}\right) = \prod_{i=1}^{L} \left(2\pi\right)^{-\frac{3}{2}} \left[\det\left(\mathbf{C}_{\hat{\Omega},i}\right)\right]^{-\frac{1}{2}} \exp\left[-\frac{1}{2}\left(\hat{\Omega}_i - \Omega_i\left(\mathbf{g}\right)\right)^T \mathbf{C}_{\hat{\Omega},i}^{-1}\left(\hat{\Omega}_i - \Omega_i\left(\mathbf{g}\right)\right)\right] \tag{3.22}$$

and taking the natural logarithm of the PDF produces the log-likelihood function

$$\mathcal{L}\left(\hat{\Omega}_1, \cdots, \hat{\Omega}_L \middle| \mathbf{g}\right) =$$
$$-\frac{3L}{2}\ln\left(2\pi\right) - \frac{1}{2}\ln\left[\prod_{i=1}^{L}\det\left(\mathbf{C}_{\hat{\Omega},i}\right)\right] - \frac{1}{2}\sum_{i=1}^{L}\left(\hat{\Omega}_i - \Omega_i\left(\mathbf{g}\right)\right)^T \mathbf{C}_{\hat{\Omega},i}^{-1}\left(\hat{\Omega}_i - \Omega_i\left(\mathbf{g}\right)\right). \tag{3.23}$$

If the parameter estimates are independent with the covariance of (3.20), then the log-likelihood function becomes

$$\mathcal{L}\left(\hat{\Omega}_1, \cdots, \hat{\Omega}_L \middle| \mathbf{g}\right) =$$
$$-\frac{3L}{2}\ln\left(2\pi\right) - \frac{1}{2}\ln\left[\prod_{i=1}^{L}\left(\sigma_{\hat{\theta},i}^2 + \sigma_{\text{attitude},i}^2\right)\left(\sigma_{\hat{\phi},i}^2 + \sigma_{\text{attitude},i}^2\right)\left(\sigma_{\hat{f},i}^2 + \sigma_{\text{frequency},i}^2\right)\right]$$
$$-\frac{1}{2}\left(\sum_{i=1}^{L}\frac{\left(\hat{\theta}_{ENU,i} - \theta_{ENU,i}\left(\mathbf{g}\right)\right)^2}{\sigma_{\hat{\theta},i}^2 + \sigma_{\text{attitude},i}^2} + \sum_{i=1}^{L}\frac{\left(\hat{\phi}_{ENU,i} - \phi_{ENU,i}\left(\mathbf{g}\right)\right)^2}{\sigma_{\hat{\phi},i}^2 + \sigma_{\text{attitude},i}^2} + \sum_{i=1}^{L}\frac{\left(\hat{f}_{d,i} - f_{d,i}\left(\mathbf{g}\right)\right)^2}{\sigma_{\hat{f},i}^2 + \sigma_{\text{frequency},i}^2}\right). \tag{3.24}$$

As described in Section 2.4, the MLE of the parameter $\mathbf{g}$ is the value of $\mathbf{g}$ which maximizes the log-likelihood function. Maximization of the log-likelihood function is accomplished by minimizing the the summation terms. Utilizing angle and frequency estimates, the AOA/FOA geolocation MLE is [37, 38]

$$\hat{\mathbf{g}}_{AOA/FOA} =$$
$$\arg\min_{\mathbf{g}}\left\{\sum_{i=1}^{L}\frac{\left(\hat{\theta}_{ENU,i} - \theta_{ENU,i}\left(\mathbf{g}\right)\right)^2}{\sigma_{\hat{\theta},i}^2 + \sigma_{\text{attitude},i}^2} + \sum_{i=1}^{L}\frac{\left(\hat{\phi}_{ENU,i} - \phi_{ENU,i}\left(\mathbf{g}\right)\right)^2}{\sigma_{\hat{\phi},i}^2 + \sigma_{\text{attitude},i}^2} + \sum_{i=1}^{L}\frac{\left(\hat{f}_{d,i} - f_{d,i}\left(\mathbf{g}\right)\right)^2}{\sigma_{\hat{f},i}^2 + \sigma_{\text{frequency},i}^2}\right\}. \tag{3.25}$$

48

Using just the estimated angles, the AOA geolocation MLE is [39]

$$\hat{\mathbf{g}}_{AOA} = \underset{\mathbf{g}}{\arg\min} \left\{ \sum_{i=1}^{L} \frac{\left(\hat{\theta}_{ENU,i} - \theta_{ENU,i}(\mathbf{g}) \right)^2}{\sigma_{\hat{\theta},i}^2 + \sigma_{\text{attitude},i}^2} + \sum_{i=1}^{L} \frac{\left(\hat{\phi}_{ENU,i} - \phi_{ENU,i}(\mathbf{g}) \right)^2}{\sigma_{\hat{\phi},i}^2 + \sigma_{\text{attitude},i}^2} \right\}. \tag{3.26}$$

Using just the estimated frequency, the FOA geolocation MLE is [5]

$$\hat{\mathbf{g}}_{FOA} = \underset{\mathbf{g}}{\arg\min} \left\{ \sum_{i=1}^{L} \frac{\left(\hat{f}_{d,i} - f_{d,i}(\mathbf{g}) \right)^2}{\sigma_{\hat{f},i}^2 + \sigma_{\text{frequency},i}^2} \right\}. \tag{3.27}$$

The non-linear weighted least-squares minimization of (3.25) for the AOA/FOA MLE is solved using the iterative Gauss-Newton process. The AOA and FOA solutions are derived by omitting the frequency and angle terms, respectively. Equation (3.25) is expressed in matrix notation as

$$\hat{\mathbf{g}}_{AOA/FOA} = \underset{\mathbf{g}}{\arg\min} \left\{ \left[\hat{\mathbf{\Omega}} - \mathbf{\Omega}(\mathbf{g}) \right]^T \mathbf{C}_{\hat{\mathbf{\Omega}}}^{-1} \left[\hat{\mathbf{\Omega}} - \mathbf{\Omega}(\mathbf{g}) \right] \right\} \tag{3.28}$$

where the collection of L sets of estimated parameters is

$$\hat{\mathbf{\Omega}} = \left[\begin{array}{cccccccc} \hat{\theta}_{ENU,1} & \hat{\phi}_{ENU,1} & \hat{f}_{d,1} & \cdots & \hat{\theta}_{ENU,L} & \hat{\phi}_{ENU,L} & \hat{f}_{d,L} \end{array} \right]_{1 \times 3L}^T, \tag{3.29}$$

with covariance

$$\mathbf{C}_{\hat{\mathbf{\Omega}}} = \text{diag} \left[\begin{array}{ccc} \mathbf{C}_{\hat{\mathbf{\Omega}},1} & \cdots & \mathbf{C}_{\hat{\mathbf{\Omega}},L} \end{array} \right]_{3L \times 3L}, \tag{3.30}$$

and the true parameter values as a function of $\mathbf{g}$ are

$$\mathbf{\Omega}(\mathbf{g}) = \left[\begin{array}{cccccccc} \theta_{ENU,1}(\mathbf{g}) & \phi_{ENU,1}(\mathbf{g}) & f_{d,1}(\mathbf{g}) & \cdots & \theta_{ENU,L}(\mathbf{g}) & \phi_{ENU,L}(\mathbf{g}) & f_{d,L}(\mathbf{g}) \end{array} \right]_{1 \times 3L}^T. \tag{3.31}$$

The gradients of the angle and frequency functions with respect to the ECEF components of $\mathbf{g}$ are

$$\nabla_{\mathbf{g}} \theta_{ENU,i}(\mathbf{g}) = \left[\begin{array}{ccc} \frac{\partial \theta_{ENU,i}(\mathbf{g})}{\partial g_x} & \frac{\partial \theta_{ENU,i}(\mathbf{g})}{\partial g_y} & \frac{\partial \theta_{ENU,i}(\mathbf{g})}{\partial g_z} \end{array} \right] \tag{3.32}$$

$$\nabla_{\mathbf{g}} \phi_{ENU,i}(\mathbf{g}) = \left[\begin{array}{ccc} \frac{\partial \phi_{ENU,i}(\mathbf{g})}{\partial g_x} & \frac{\partial \phi_{ENU,i}(\mathbf{g})}{\partial g_y} & \frac{\partial \phi_{ENU,i}(\mathbf{g})}{\partial g_z} \end{array} \right] \tag{3.33}$$

$$\nabla_{\mathbf{g}} f_{d,i}(\mathbf{g}) = \left[\begin{array}{ccc} \frac{\partial f_{d,i}(\mathbf{g})}{\partial g_x} & \frac{\partial f_{d,i}(\mathbf{g})}{\partial g_y} & \frac{\partial f_{d,i}(\mathbf{g})}{\partial g_z} \end{array} \right]. \tag{3.34}$$

The partial derivatives of the non-linear angle and frequency functions can be evaluated numerically by defining the following perturbation terms:

$$\begin{aligned}
\Delta_x &= \begin{bmatrix} 1 & 0 & 0 \end{bmatrix}^T \\
\Delta_y &= \begin{bmatrix} 0 & 1 & 0 \end{bmatrix}^T \\
\Delta_z &= \begin{bmatrix} 0 & 0 & 1 \end{bmatrix}^T.
\end{aligned} \tag{3.35}$$

The partial derivatives of the elevation angles are approximated as:

$$\begin{aligned}
\frac{\partial \theta_{ENU,i}(\mathbf{g})}{\partial g_x} &\approx \theta_{ENU,i}(\mathbf{g} + \Delta_x) - \theta_{ENU,i}(\mathbf{g}) \\
\frac{\partial \theta_{ENU,i}(\mathbf{g})}{\partial g_y} &\approx \theta_{ENU,i}(\mathbf{g} + \Delta_y) - \theta_{ENU,i}(\mathbf{g}) \\
\frac{\partial \theta_{ENU,i}(\mathbf{g})}{\partial g_z} &\approx \theta_{ENU,i}(\mathbf{g} + \Delta_z) - \theta_{ENU,i}(\mathbf{g}).
\end{aligned} \tag{3.36}$$

The partial derivatives of the azimuth angles are approximated as:

$$\begin{aligned}
\frac{\partial \phi_{ENU,i}(\mathbf{g})}{\partial g_x} &\approx \phi_{ENU,i}(\mathbf{g} + \Delta_x) - \phi_{ENU,i}(\mathbf{g}) \\
\frac{\partial \phi_{ENU,i}(\mathbf{g})}{\partial g_y} &\approx \phi_{ENU,i}(\mathbf{g} + \Delta_y) - \phi_{ENU,i}(\mathbf{g}) \\
\frac{\partial \phi_{ENU,i}(\mathbf{g})}{\partial g_z} &\approx \phi_{ENU,i}(\mathbf{g} + \Delta_z) - \phi_{ENU,i}(\mathbf{g}).
\end{aligned} \tag{3.37}$$

The partial derivatives of the frequencies are approximated as:

$$\begin{aligned}
\frac{\partial f_{d,i}(\mathbf{g})}{\partial g_x} &\approx f_{d,i}(\mathbf{g} + \Delta_x) - f_{d,i}(\mathbf{g}) \\
\frac{\partial f_{d,i}(\mathbf{g})}{\partial g_y} &\approx f_{d,i}(\mathbf{g} + \Delta_y) - f_{d,i}(\mathbf{g}) \\
\frac{\partial f_{d,i}(\mathbf{g})}{\partial g_z} &\approx f_{d,i}(\mathbf{g} + \Delta_z) - f_{d,i}(\mathbf{g}).
\end{aligned} \tag{3.38}$$

The gradients of the i-th set of true parameters is

$$\nabla_{\mathbf{g}} \Omega_i(\mathbf{g}) = \begin{bmatrix} \nabla_{\mathbf{g}} \theta_{ENU,i}(\mathbf{g}) \\ \nabla_{\mathbf{g}} \phi_{ENU,i}(\mathbf{g}) \\ \nabla_{\mathbf{g}} f_{d,i}(\mathbf{g}) \end{bmatrix}_{3 \times 3} \tag{3.39}$$

and the Jacobian of the collection of L sets is

$$\mathbf{J}(\mathbf{g}) = \begin{bmatrix} \nabla_{\mathbf{g}} \Omega_1(\mathbf{g}) \\ \vdots \\ \nabla_{\mathbf{g}} \Omega_L(\mathbf{g}) \end{bmatrix}_{3L \times 3} . \tag{3.40}$$

The Gauss-Newton iterations for the AOA/FOA geolocation MLE becomes

$$\hat{\mathbf{g}}_{k+1} = \hat{\mathbf{g}}_k + \left(\mathbf{J}^T \left(\hat{\mathbf{g}}_k \right) \mathbf{C}_{\hat{\Omega}}^{-1} \mathbf{J} \left(\hat{\mathbf{g}}_k \right) \right)^{-1} \mathbf{J}^T \left(\hat{\mathbf{g}}_k \right) \mathbf{C}_{\hat{\Omega}}^{-1} \left[\hat{\Omega} - \Omega \left(\hat{\mathbf{g}}_k \right) \right] \tag{3.41}$$

and is iterated until successive estimates converge to a specified threshold ($\|\hat{\mathbf{g}}_{k+1} - \hat{\mathbf{g}}_k\| \leq \varepsilon$) or a specified number of iterations has been reached. The least squares intersection point of the collection of LOBs is used as the starting iteration ($\hat{\mathbf{g}}_1 = \hat{\mathbf{g}}_{LS}$). The Gauss-Newton process for the AOA geolocation MLE is equivalent to the NLO method described in Section 2.3.2.2 and [24, 27]. An example of the Gauss-Newton iterations for the AOA/FOA geolocation MLE is shown in Figure 3.7 where after 16 iterations, the difference between iterations is less than 1 m ($\|\hat{\mathbf{g}}_{16} - \hat{\mathbf{g}}_{15}\| \leq 1$ m) and the final iteration is the AOA/FOA estimate of the emitter location ($\hat{\mathbf{g}}_{AOA/FOA} = \hat{\mathbf{g}}_{16}$).
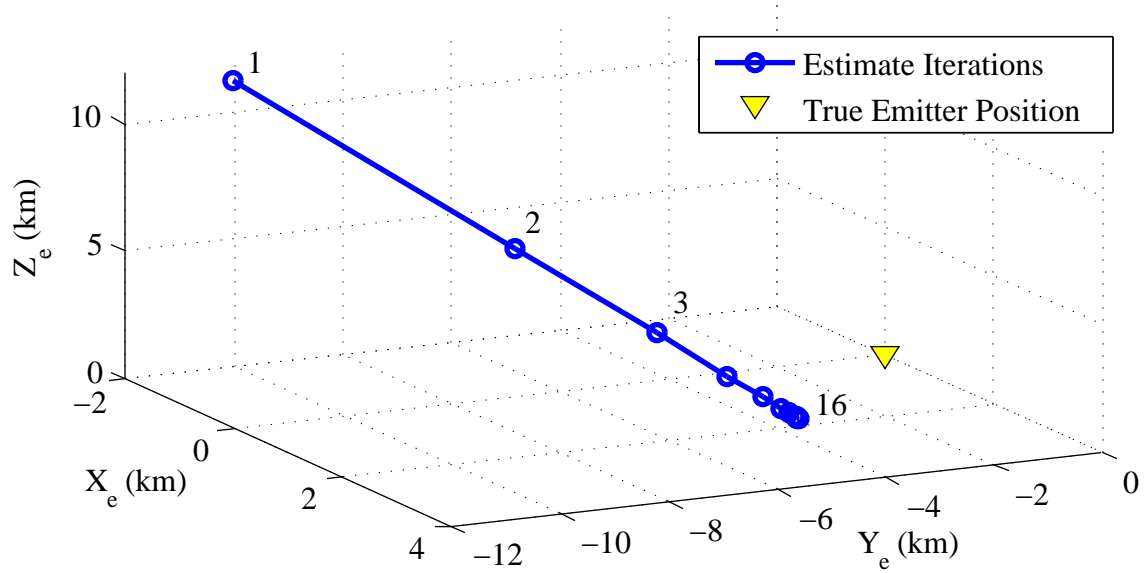
Figure 3.7: Gauss-Newton iterations for the AOA/FOA geolocation MLE. The initial iteration is the LS intersection of the collection of LOBs and the final iteration is the AOA/FOA estimate of the emitter location.

51

The 95% confidence surface of the final geolocation estimate is the ellipsoid in the ECEF coordinate system centered at $\hat{\mathbf{g}}$ and defined by

$$\left(\begin{bmatrix} x \\ y \\ z \end{bmatrix} - \hat{\mathbf{g}} \right)^T \left(\mathbf{J}^T \left(\hat{\mathbf{g}} \right) \mathbf{C}_{\hat{\Omega}}^{-1} \mathbf{J} \left(\hat{\mathbf{g}} \right) \right)^{-1} \left(\begin{bmatrix} x \\ y \\ z \end{bmatrix} - \hat{\mathbf{g}} \right) = (2.7959)^2 \qquad (3.42)$$

where x, y, and z are the ECEF components. An example of the confidence surfaces for the AOA, FOA, and AOA/FOA geolocation estimates is shown in Figure 3.8 where the term $\left(\mathbf{J}^T \left(\hat{\mathbf{g}} \right) \mathbf{C}_{\hat{\Omega}}^{-1} \mathbf{J} \left(\hat{\mathbf{g}} \right) \right)^{-1}$ is the approximated CRLB for estimate $\hat{\mathbf{g}}$.
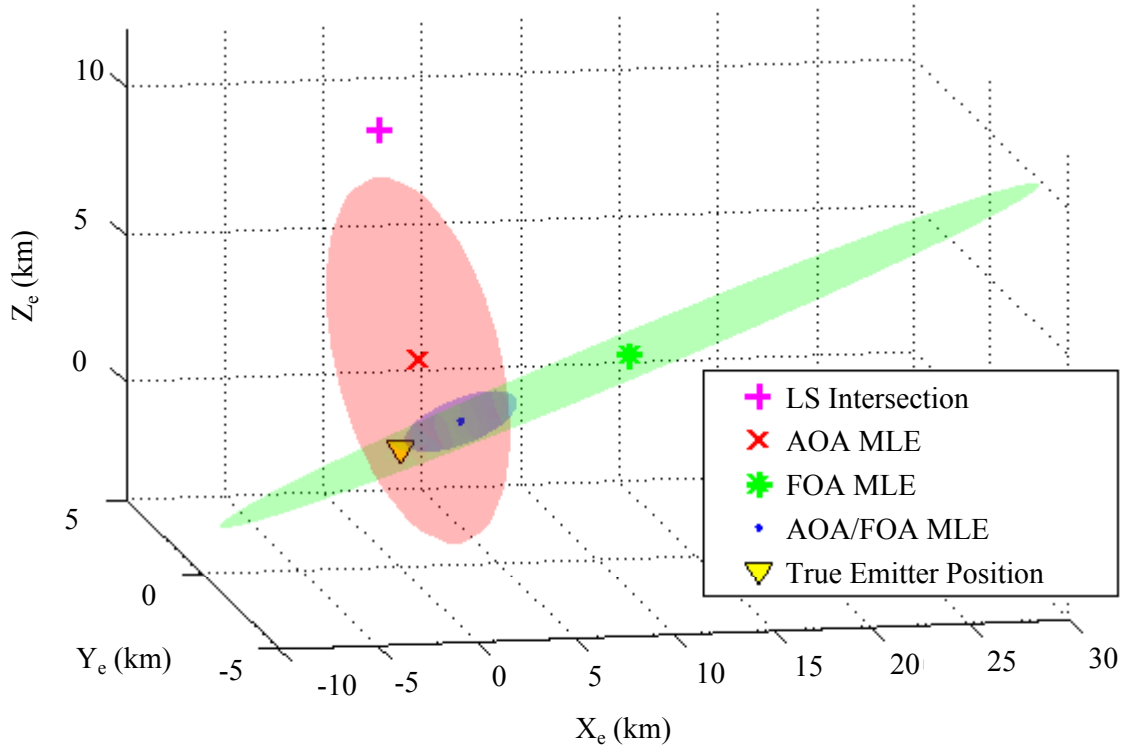
Figure 3.8: Confidence surfaces for single estimates of the emitter location from the AOA, FOA, and AOA/FOA maximum likelihood estimators. The LS intersection is used as the initial iteration for the estimators.

3.4 Cramér-Rao Lower Bound on Geolocation Estimates

$$\text{cov}\,(\hat{\mathbf{g}}) \geq \text{CRLB}\,(\hat{\mathbf{g}}) = \left(\mathbf{J}^{\text{T}}\,(\mathbf{g})\,\mathbf{C}_{\boldsymbol{\Omega}}^{-1}\mathbf{J}\,(\mathbf{g})\right)^{-1} \tag{3.43}$$

For a particular geolocation analysis scenario where L sets of angle and frequency measurements collected by a single moving receiver at positions $\mathbf{p}_i$ and velocities $\mathbf{v}_i$ from a RF emitter located at $\mathbf{g}$, the covariance of unbiased estimates of $\mathbf{g}$ is bounded by the CRLB

$$\begin{bmatrix} \text{var}\,(\hat{g}_x) & \text{cov}\,(\hat{g}_x, \hat{g}_y) & \text{cov}\,(\hat{g}_x, \hat{g}_z) \\ \text{cov}\,(\hat{g}_x, \hat{g}_y) & \text{var}\,(\hat{g}_y) & \text{cov}\,(\hat{g}_y, \hat{g}_z) \\ \text{cov}\,(\hat{g}_x, \hat{g}_z) & \text{cov}\,(\hat{g}_y, \hat{g}_z) & \text{var}\,(\hat{g}_z) \end{bmatrix} \geq \text{CRLB}\,(\hat{\mathbf{g}}). \tag{3.44}$$

The FIM for Gaussian distributed AOA and FOA measurements is

$$\mathbf{F}_{AOA/FOA}\,(\mathbf{g}) = E\left\{\left[\nabla_{\mathbf{g}}\mathcal{L}\left(\hat{\Omega}_1, \cdots, \hat{\Omega}_L\big|\mathbf{g}\right)\right]^T \left[\nabla_{\mathbf{g}}\mathcal{L}\left(\hat{\Omega}_1, \cdots, \hat{\Omega}_L\big|\mathbf{g}\right)\right]\right\} \tag{3.45}$$

and after evaluation of the gradient and expectation operations becomes

$$\mathbf{F}_{AOA/FOA}\,(\mathbf{g}) = \sum_{i=1}^{L}\left[\nabla_{\mathbf{g}}\Omega_i\,(\mathbf{g})\right]^T \mathbf{C}_{\Omega,i}^{-1}\left[\nabla_{\mathbf{g}}\Omega_i\,(\mathbf{g})\right]. \tag{3.46}$$

Using the matrix notation defined in Section 3.3, the FIM for AOA/FOA is expressed as

$$\mathbf{F}_{AOA/FOA}\,(\mathbf{g}) = \mathbf{J}^T\,(\mathbf{g})\,\mathbf{C}_{\boldsymbol{\Omega}}^{-1}\mathbf{J}\,(\mathbf{g}), \tag{3.47}$$

the FIM for AOA is,

$$\mathbf{F}_{AOA}\,(\mathbf{g}) = \sum_{i=1}^{L} \frac{\left[\nabla_{\mathbf{g}}\theta_{ENU,i}\,(\mathbf{g})\right]^T \left[\nabla_{\mathbf{g}}\theta_{ENU,i}\,(\mathbf{g})\right]}{\sigma_{\theta,i}^2 + \sigma_{\text{attitude},i}^2} + \sum_{i=1}^{L} \frac{\left[\nabla_{\mathbf{g}}\phi_{ENU,i}\,(\mathbf{g})\right]^T \left[\nabla_{\mathbf{g}}\phi_{ENU,i}\,(\mathbf{g})\right]}{\sigma_{\phi,i}^2 + \sigma_{\text{attitude},i}^2}, \tag{3.48}$$

the FIM for FOA is

$$\mathbf{F}_{FOA}\,(\mathbf{g}) = \sum_{i=1}^{L} \frac{\left[\nabla_{\mathbf{g}}f_{d,i}\,(\mathbf{g})\right]^T \left[\nabla_{\mathbf{g}}f_{d,i}\,(\mathbf{g})\right]}{\sigma_{f,i}^2 + \sigma_{\text{frequency},i}^2}, \tag{3.49}$$

and the CRLB for each geolocation method is equal to the inverse of the respective FIM

$$\text{CRLB}\,(\hat{\mathbf{g}}) = \mathbf{F}^{-1}\,(\mathbf{g}). \tag{3.50}$$

An example of the CRLBs on geolocation estimates is shown in Figure 3.9 where the CRLBs are visualized as 95% confidence surfaces centered at the true emitter position and defined by the FIM covariance matrix. Given a sufficient number of L signal collects, the estimates of the emitter location are asymptotically distributed as

$$\hat{\mathbf{g}} \overset{a}{\sim} \mathcal{N}\left(\mathbf{g}, \mathbf{F}^{-1}\left(\mathbf{g}\right)\right). \tag{3.51}$$
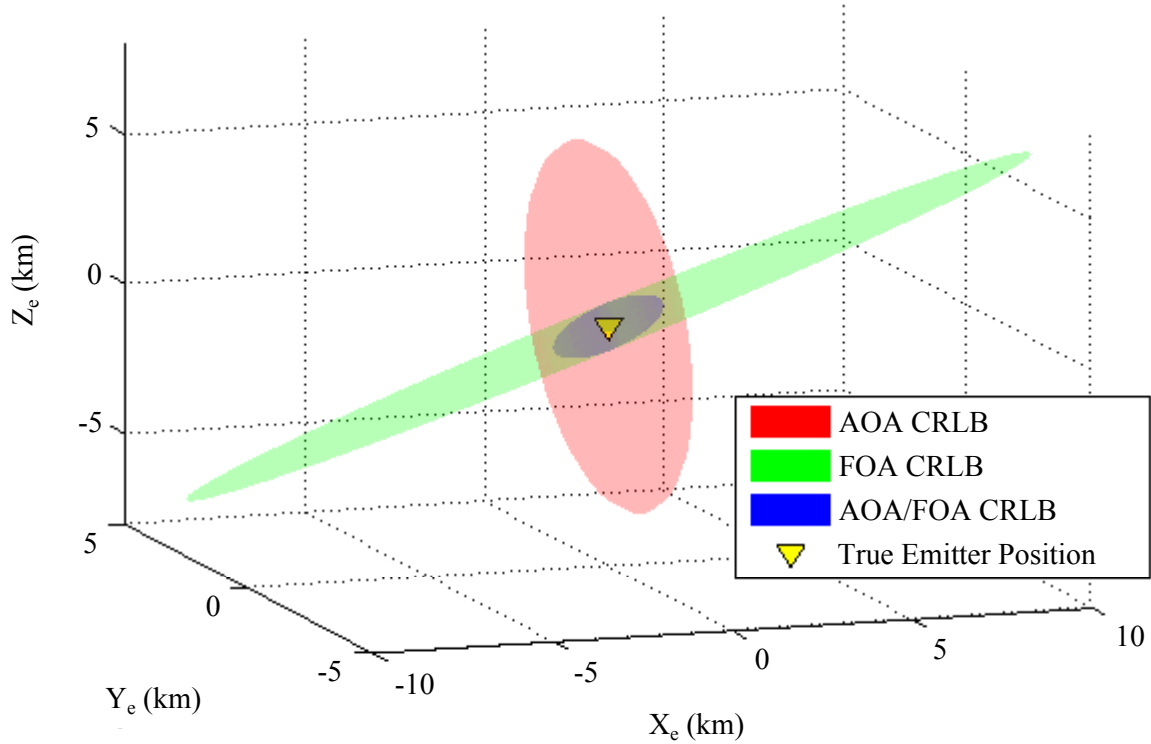
Figure 3.9: Cramér-Rao lower bounds on geolocation estimates of the emitter location for the AOA, FOA, and AOA/FOA geolocation methods visualized as 95% confidence surfaces.

3.5   Geolocation Algorithm Performance Analysis

This section describes the simulation environment used to evaluate the performance of the geolocation algorithms developed in this thesis. Systems Tool Kit (STK) 10 developed

by Analytical Graphics Inc. was used to model the analysis scenario geometry of a single

CubeSat in LEO and a single RF SOI. MATLAB developed by MathWorks Inc. was used

implement the geolocation algorithms using simulated estimates of the signal parameters

based off the orbital position and velocity data generated from STK.

3.5.1 Orbital Position and Velocity Simulation.

The analysis scenario was modeled in STK and outputs the orbital position and

velocity data in 1 second intervals to simulate the CubeSat onboard GNC subsystem. The

RF SOI was modeled as shown in Figures 3.3 and 3.4 as an 80° half angle cone centered

at 39.782° N latitude, 84.083° W longitude, and 0 m altitude. The single CubeSat platform

was modeled as a 60° inclined, 450 km circular orbit. The right ascension of the ascending

node orbital parameter was varied in 2.5° increments to produce 11 passes of the CubeSat

over the SOI as shown in Figure 3.10 with the time durations shown in Table 3.1. Each

pass produces a set of ECEF position and velocity data in 1 second intervals when the

CubeSat is traveling through the SOI cone. The intervals of pass 7 are shown in Table 3.2

as an example.

Table 3.1: Time duration of each orbital pass of the CubeSat over the RF SOI.

Pass:	1	2	3	4	5	6	7	8	9	10	11
Duration (s):	72	184	247	294	331	363	386	405	417	425	428

3.5.2 Geolocation Algorithm Simulation.

The analysis scenario positions and velocities for a given pass are imported to the

MATLAB environment to simulate the parameter measurements and to assess the

performance of the geolocation algorithms. A single RF SOI is located at position **g** and

the collection of L measurements are simulated from the true parameters of the pass from
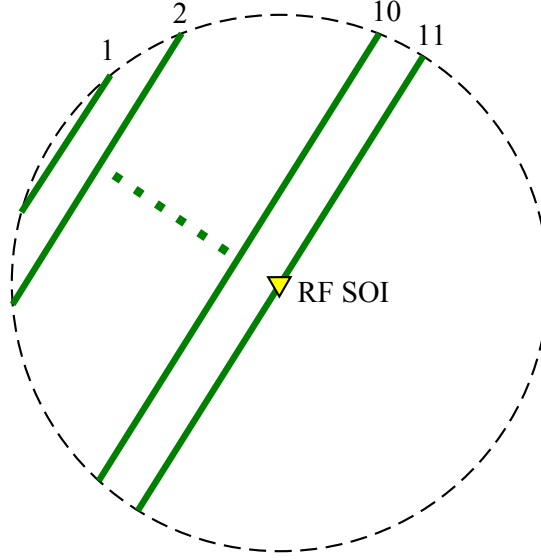
Figure 3.10: 11 orbital passes of a single CubeSat over the RF SOI.

Table 3.2: ECEF position and velocity data for pass 7.

Time t (s)	X_e (m)	Y_e (m)	Z_e (m)	v_x (m/s)	v_y (m/s)	v_z (m/s)
1	-915252	-5557270	3860379	4729.851	2699.525	5007.538
2	-910526	-5554566	3865384	4731.386	2705.758	5002.701
$\vdots$						
386	968956	-4096095	5376484	4934.411	4771.814	2746.139

the analysis scenario. All measurements are assumed to be Gaussian distributed with the value of the means being the true parameter values. The measurement variances are defined by the estimator's respective CRLBs and an additional error variance. The CRLB variances are in terms of the number of samples N per measurement, the SNR η of each measurement, and the associated system parameters. The performance of the single sinusoidal parameter estimators for angle, frequency, and SNR measurements will be

shown in Section 4.1 and the threshold is defined where the estimator performance achieves the respective CRLB.

The i-th estimate of the CubeSat position and velocity are simulated as

$$\hat{\mathbf{p}}_i \sim \mathcal{N}\left(\mathbf{p}_i, \sigma^2_{\text{position}}\mathbf{I}_{3\times3}\right) \tag{3.52}$$

and

$$\hat{\mathbf{v}}_i \sim \mathcal{N}\left(\mathbf{v}_i, \sigma^2_{\text{velocity}}\mathbf{I}_{3\times3}\right) \tag{3.53}$$

where $\sigma^2_{\text{position}}$ and $\sigma^2_{\text{velocity}}$ are the variances of the position knowledge error and velocity knowledge error, respectively.

The i-th estimate of the elevation angle in the local ENU reference frame is simulated as

$$\hat{\theta}_{ENU,i} \sim \mathcal{N}\left(\theta_{ENU,i}\left(\mathbf{g}\right), \sigma^2_{\theta,i} + \sigma^2_{\text{attitude}}\right) \tag{3.54}$$

where the true elevation angle is

$$\theta_{ENU,i}\left(\mathbf{g}\right) = \text{atan2}\left(U_i, \sqrt{E_i^2 + N_i^2}\right), \tag{3.55}$$

the elevation angle CRLB is

$$\sigma^2_{\theta,i} = \frac{\left[\eta_i\left(\mathbf{g}\right)\right]^{-1} + M}{\eta_i\left(\mathbf{g}\right)NM^2(2\pi r/\lambda_{r,i})^2\cos^2\left(\theta_{ENU,i}\left(\mathbf{g}\right) + \pi/2\right)(\pi/180)^2}, \tag{3.56}$$

and $\sigma^2_{\text{attitude}}$ is the variance of the attitude knowledge error.

The i-th estimate of the azimuth angle in the local ENU reference frame is simulated as

$$\hat{\phi}_{ENU,i} \sim \mathcal{N}\left(\phi_{ENU,i}\left(\mathbf{g}\right), \sigma^2_{\phi,i} + \sigma^2_{\text{attitude}}\right) \tag{3.57}$$

where the true azimuth angle is

$$\phi_{ENU,i}\left(\mathbf{g}\right) = \text{atan2}\left(E_i, N_i\right), \tag{3.58}$$

and the azimuth angle CRLB is

$$\sigma^2_{\phi,i} = \frac{\left[\eta_i\left(\mathbf{g}\right)\right]^{-1} + M}{\eta_i\left(\mathbf{g}\right)NM^2(2\pi r/\lambda_{r,i})^2\sin^2\left(\theta_{ENU,i}\left(\mathbf{g}\right) + \pi/2\right)(\pi/180)^2}. \tag{3.59}$$

An example of L LOBs in the ECEF coordinate system using the estimated positions and angles is shown in Figure 3.11.
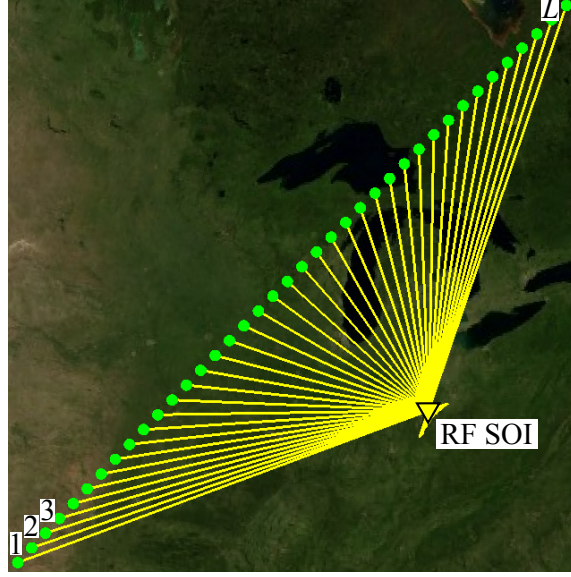
Figure 3.11: Lines of bearing using the simulated positions and angles from an analysis scenario pass.

The i-th estimate of the Doppler shifted frequency is simulated as

$$\hat{f}_{d,i} \sim \mathcal{N}\left(f_{d,i}\left(\mathbf{g}\right), \sigma^2_{f_d,i} + \sigma^2_{\text{frequency}}\right) \tag{3.60}$$

where the true Doppler shifted frequency is

$$f_{d,i}\left(\mathbf{g}\right) = -\frac{f_c}{c}\left[\frac{v_{x,i}\left(p_{x,i} - g_x\right) + v_{y,i}\left(p_{y,i} - g_y\right) + v_{z,i}\left(p_{z,i} - g_z\right)}{\sqrt{\left(p_{x,i} - g_x\right)^2 + \left(p_{y,i} - g_y\right)^2 + \left(p_{z,i} - g_z\right)^2}}\right], \tag{3.61}$$

the frequency CRLB is

$$\sigma^2_{f_d,i} = \frac{6f_s^2}{\eta_i\left(\mathbf{g}\right)\left(2\pi\right)^2 N\left(N^2 - 1\right)}, \tag{3.62}$$

and $\sigma^2_{\text{frequency}}$ is the variance of the frequency knowledge error.

The i-th estimate of the received SNR is simulated as

$$\hat{\eta}_i \sim \mathcal{N}\left(\eta_i\left(\mathbf{g}\right), \sigma^2_\eta\right) \tag{3.63}$$

where the true SNR is

$$\eta_i(\mathbf{g}) = \frac{\sigma_t^2 G_t G_r}{L_a L_p L_{s,i}(\mathbf{g}, \lambda_c) \kappa T_{sys} W} \tag{3.64}$$

and the SNR CRLB is

$$\sigma_\eta^2 = \frac{1}{2N}. \tag{3.65}$$

The received SNR is a function of the assumed transmitter parameters, assumed receiver parameters, and free space path loss. If the transmitter and receiver properties are assumed constant, then the received SNR varies due to the free space path loss, such that

$$\eta_i(\mathbf{g}) = \frac{\text{const.}}{L_{s,i}(\mathbf{g}, \lambda_c)} \tag{3.66}$$

where the free space path loss is a function of the distance between transmitter and receiver, and the wavelength of the transmitted signal

$$L_{s,i}(\mathbf{g}, \lambda_c) = \left(\frac{4\pi}{\lambda_c} \sqrt{\left(p_{x,i} - g_x\right)^2 + \left(p_{y,i} - g_y\right)^2 + \left(p_{z,i} - g_z\right)^2} \right)^2. \tag{3.67}$$

In order to generalize the received SNR parameter, the SNR at the first signal collect η_1 is used to define the SNR of subsequent signal collects such that

$$\eta_i(\mathbf{g}) = \eta_1 \frac{L_{s,1}(\mathbf{g}, \lambda_c)}{L_{s,i}(\mathbf{g}, \lambda_c)}. \tag{3.68}$$

An example link budget for the received SNR at the first signal collect is shown in Table 3.3. The distance from transmitter to receiver in the analysis scenario is approximately 1,600 km. The transmitter parameters are expressed as the Effective Isotropic Radiated Power (EIRP). The atmospheric attenuation at 1,315 MHz is assumed to be 0.5 dB [40] and constant. Assuming a vertically polarized transmit antenna and a circularly polarized receive antenna array, the polarization mismatch loss is -3 dB. Assuming a noise temperature of 800 K and 200 kHz signal bandwidth of interest, the received SNR at the first signal collect is 9.2 dB. Since defining implementation specific parameters is beyond the scope of this thesis, the η_1 parameter is used to represent the transmitter and receiver system parameters.

Table 3.3: Example link budget for the received SNR at the first signal collect.

Transmitter Frequency	f_c	1,315	MHz
Propagation Path Length	d	1,600	km
Transmitter EIRP	$\sigma_t^2 G_t$	20.0	dB
Free Space Path Loss	$L_s(\mathbf{g}, \lambda_c)$	-158.9	dB
Atmospheric Loss	L_a	-0.5	dB
Receiver Antenna Gain	G_r	5.0	dB
Polarization Loss	L_p	-3.0	dB
Received Signal Power	σ_r^2	-137.4	dBW
System Noise Temperature	T_{sys}	800	K
Noise Bandwidth	W	200	kHz
Noise Power	σ_w^2	-146.6	dBW
Received SNR	η	9.2	dB

The 4 geolocation algorithms implemented in the MATLAB simulation are the LS intersection, and the AOA/FOA, AOA, and FOA MLEs. Using the collection of L simulated and estimated positions, velocities, angles, frequencies, and variances, the LS intersection algorithm is implemented as described in Section 2.3.2.1 and the MLE algorithms are implemented as described in Section 3.3. The LS intersection estimate is used as the initial estimate ($\hat{\mathbf{g}}_1 = \hat{\mathbf{g}}_{LS}$) for all 3 MLE iterative algorithms and the estimated parameters are used to estimate the parameter variances. Examples of the estimated SNR, frequencies, and parameter variances for 39 signal collects are compared to the true values in Figures 3.12 through 3.16.
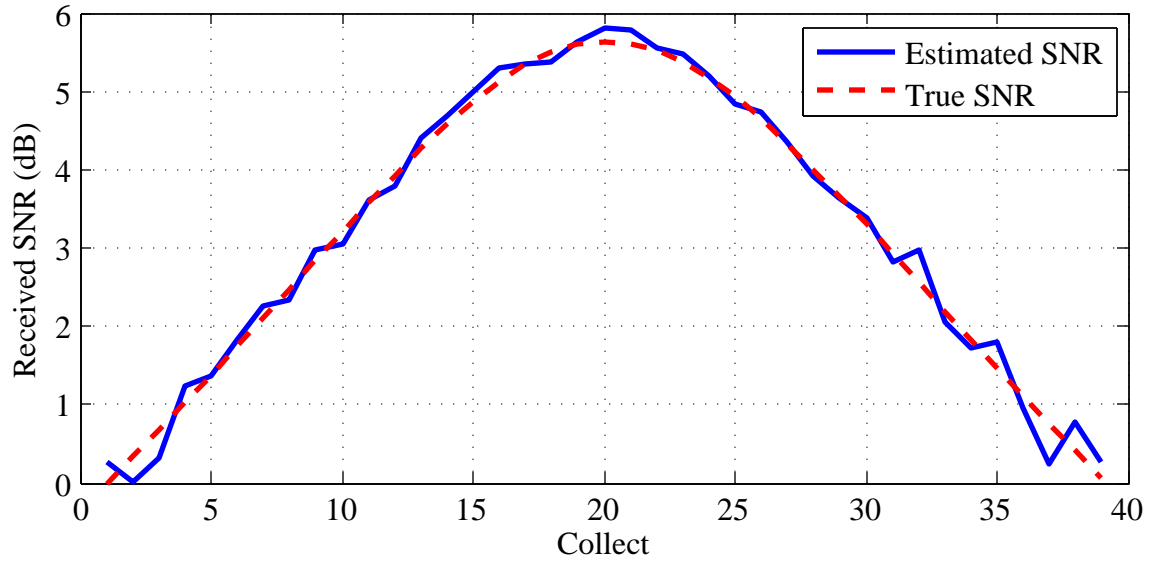
Figure 3.12: Estimated received SNR per signal collect for $\eta_1 = 0$ dB.
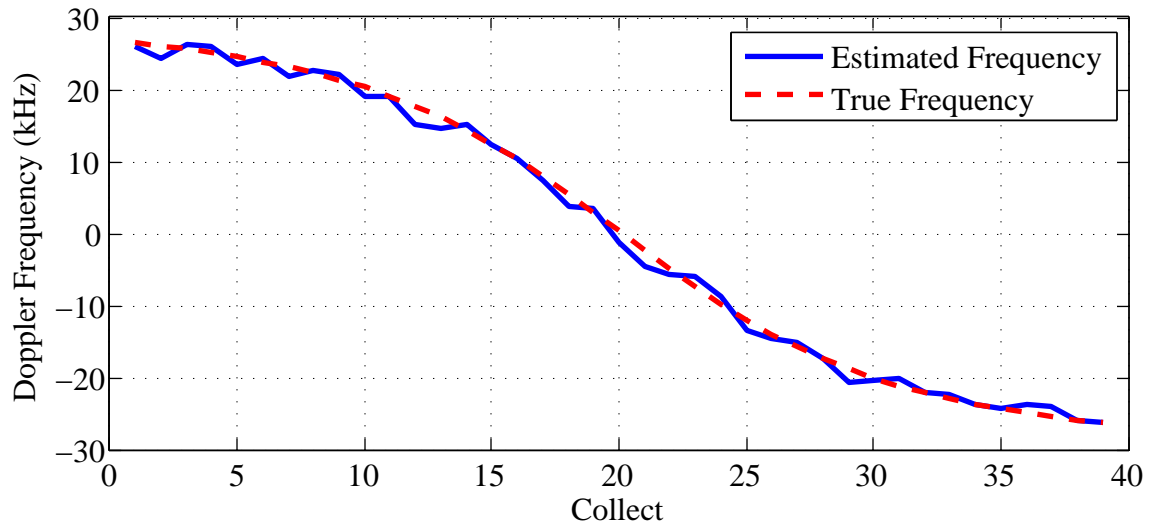
Figure 3.13: Estimated Doppler frequency per signal collect.
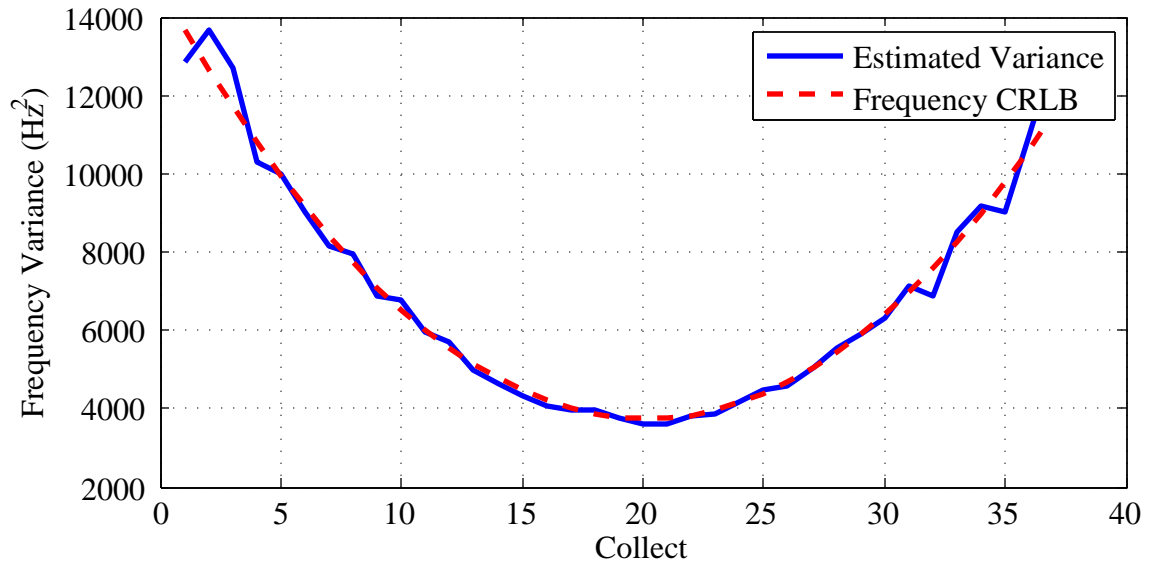
Figure 3.14: Estimated frequency variance per signal collect.
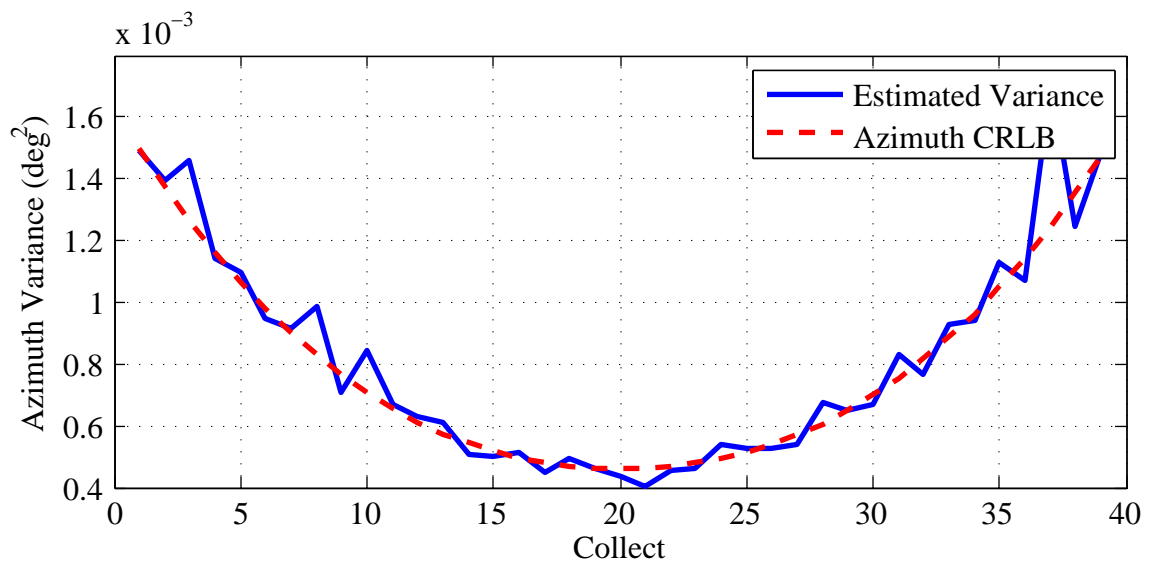
Figure 3.15: Estimated azimuth variance per signal collect.
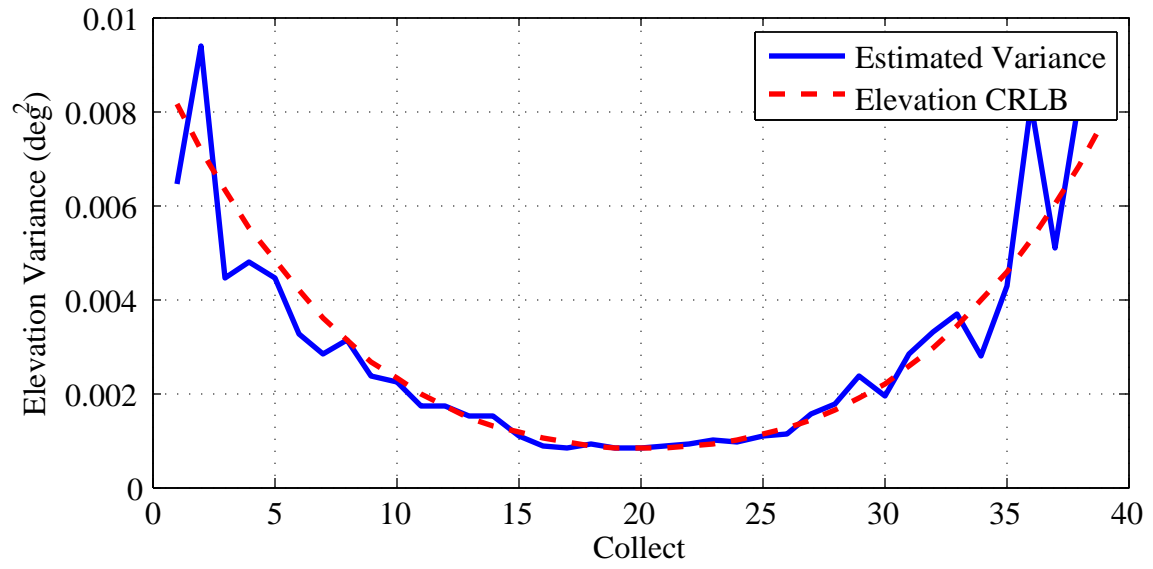
Figure 3.16: Estimated elevation variance per signal collect.

The performance of the 4 geolocation algorithms is assessed by comparing the Root Mean Square Error (RMSE) of independent Monte Carlo Simulation (MCS) trials to the RMSE of the associated CRLB. An example of 200 MCS geolocation estimates per algorithm is shown in Figure 3.17. The RMSE of the CRLB on geolocation estimates is defined as

$$\text{RMSE}_{CRLB} = \sqrt{\text{trace}\{\text{CRLB}(\hat{\mathbf{g}})\}}. \tag{3.69}$$

The error of P MCS trials is defined as

$$\mathbf{e}_{\hat{\mathbf{g}}} = \begin{bmatrix} \|\hat{\mathbf{g}}_1 - \mathbf{g}\| \\ \vdots \\ \|\hat{\mathbf{g}}_P - \mathbf{g}\| \end{bmatrix}_{P \times 1}. \tag{3.70}$$

The sample mean of the MCS trials is

$$\mu_{\mathbf{e}} = \frac{1}{P} \sum_{i=1}^{P} \mathbf{e}_{\hat{\mathbf{g}},i} \tag{3.71}$$

and the sample variance is

$$\sigma_{\mathbf{e}}^2 = \frac{1}{P-1} \sum_{i=1}^{P} \left(\mathbf{e}_{\hat{\mathbf{g}},i} - \mu_{\mathbf{e}}\right)^2. \tag{3.72}$$

The RMSE of the MCS trials is

$$\text{RMSE}_{MCS} = \sqrt{\sigma_{\mathbf{e}}^2 + \mu_{\mathbf{e}}^2}. \tag{3.73}$$

3.5.3 Geolocation Simulation Parameters and Emitter Types.

This section defines the parameters of the geolocation simulation. The transmitter frequency (f_c = 1,315 MHz), number of antenna elements ($M = 4$), and UCA radius ($r = \lambda_c/4$) parameters are held constant throughout the simulations. The simulation parameters listed in Table 3.4 are varied to conduct the sensitivity analysis shown in Section 4.2 to assess parameter impact on the accuracy of the geolocation algorithms. The geometry of the analysis scenario is varied through the 11 orbital passes shown in Figure 3.10 where the distance from transmitter to receiver, relative velocity, angles,

64
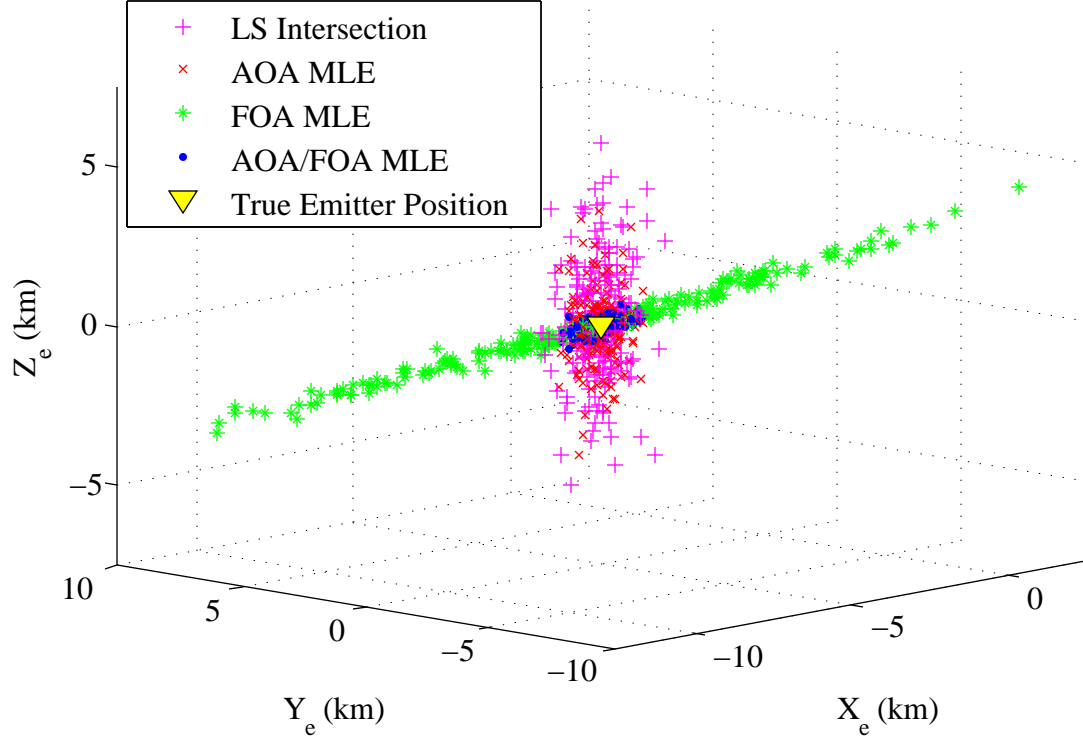
Figure 3.17: An example of 800 MCS geolocation estimates (200 per algorithm) of the position of a RF SOI. The RMSE of the MCS estimates is compared to the associated CRLB.

frequencies, and total pass duration are unique for each pass. The number of signal collects parameter L is varied to simulate a limited number of signal collects during a pass where the collects occur sequentially. For example, if $L = 10$ out of 40 possible signal collects, the signal is received during the first 25% of the pass. The number of samples per collect parameter N is varied to simulate different signal durations and sampling rates. The SNR at the first signal collect parameter η_1 is varied to simulate different transmitted signal and receiver characteristics. The attitude knowledge error parameter $\sigma^2_{\text{attitude}}$ is varied to simulate the error from the CubeSat ADCS subsystem. The position knowledge error $\sigma^2_{\text{position}}$ and velocity knowledge error $\sigma^2_{\text{velocity}}$ parameters are varied to simulate the

error from the CubeSat GPS subsystem. The frequency knowledge error parameter $\sigma^2_{\text{frequency}}$ is varied to simulate local frequency oscillator drift and carrier frequency offset errors.

Table 3.4: Geolocation simulation parameters.

Orbital pass	**p, v**
Number of signal collects	L
Number of samples per collect	N
SNR at the first signal collect	η_1
Attitude knowledge error	$\sigma^2_{\text{attitude}}$
Position knowledge error	$\sigma^2_{\text{position}}$
Velocity knowledge error	$\sigma^2_{\text{velocity}}$
Frequency knowledge error	$\sigma^2_{\text{frequency}}$

Three types of RF SOI emitters are simulated by varying the total number of collects per pass, the timing between collects, the number of samples per collect and the received SNR. A high power spinning radar is simulated as signal collects occurring every 10 seconds with a relatively high SNR and a relatively low number of samples per collect. A moderate power burst communications emitter is simulated as signal collects occurring every 30 seconds with a relatively moderate SNR and a relatively moderate number of samples per collect. A low power continuous communications emitter is simulated as signal collects occurring every second during the pass with a relatively low SNR and a relatively high number of samples per collect. The 3 emitter types are summarized in Table 3.5 and the performance of the geolocation algorithms as a function of emitter type is compared in Section 4.2.

Table 3.5: Simulation parameters for three emitter types.

Emitter type	Time between signal collects	Received SNR	Number of samples
Spinning radar	10 s	High	Low
Burst communications	30 s	Moderate	Moderate
Continuous communications	1 s	Low	High

IV.   Results and Analysis

This chapter reports the statistical performance of the single sinusoidal signal parameter estimators and the geolocation algorithms used in this thesis. Section 4.1 reports the performance of the angle, frequency, and amplitude estimators in terms of the SNR and number of samples, and defines the performance threshold where the estimator variance achieves the respective CRLB. Section 4.2 reports the impact of varying the system parameters on the geolocation accuracy of the geolocation algorithms through a parameter sensitivity analysis.

4.1   Single Sinusoidal Signal Parameter Estimator Performance

This section evaluates the performance of the angle (MUSIC), frequency (MLE), and amplitude (MLE) parameter estimators used in this thesis as compared to the respective CRLBs. The threshold where the estimator variances achieve the CRLB was determined in terms of the SNR η and number of samples N of the received signal. Since it is assumed that there is only a single emitter present with no co-channel interference, the received signal is modeled as a single complex exponential signal consisting of N samples with normalized frequency f at a SNR of $\eta = \sigma_s^2$ such that

$$s[n] = \sigma_s \exp[j2\pi f n].$$

(4.1)

The signal is phase shifted according to (2.10) with a simulated 4 element UCA with radius $r = \lambda_r/4$ and true angles of $\theta = \pi/4$ and $\phi = \pi/4$

$$\mathbf{a}(\theta, \phi) = \begin{bmatrix} \exp\left(j\frac{\pi}{2}\sin(\theta)\cos\left(\phi - \frac{\pi}{4}\right)\right) \\ \exp\left(j\frac{\pi}{2}\sin(\theta)\cos\left(\phi - \frac{3\pi}{4}\right)\right) \\ \exp\left(j\frac{\pi}{2}\sin(\theta)\cos\left(\phi - \frac{5\pi}{4}\right)\right) \\ \exp\left(j\frac{\pi}{2}\sin(\theta)\cos\left(\phi - \frac{7\pi}{4}\right)\right) \end{bmatrix}_{4\times1}.$$

(4.2)

Each of the 4 phase shifted received signals is corrupted with independent unit power ($\sigma_w^2 = 1$) complex AWGN such that

$$x_m[n] = a_m(\theta, \phi)s[n] + w_m[n] \tag{4.3}$$

and the $4 \times N$ samples of the simulated received signals are contained in

$$\mathbf{X} = \mathbf{a}\,(\theta, \phi)\,\mathbf{s} + \mathbf{W}. \tag{4.4}$$

The AOA of the received signals are estimated from the estimated spatial covariance matrix $\hat{\mathbf{R}}_{xx} = \frac{1}{N}\mathbf{X}\mathbf{X}^H$ and a 2D angle grid search over the MUSIC spectrum

$$\left[\hat{\theta}, \hat{\phi}\right] = \arg\max_{\theta,\phi} \left\{ \frac{1}{\mathbf{a}^H(\theta, \phi)\,\hat{\mathbf{Q}}_w\hat{\mathbf{Q}}_w^H\mathbf{a}\,(\theta, \phi)} \right\}. \tag{4.5}$$

The location of the peaks of the MUSIC spectrum are taken as the AOA estimates of the received signal. The normalized frequency and amplitude are estimated from the DFT of the first received signal and the SNR is estimated as $\hat{\eta} = \hat{\sigma}_s^2$

$$\hat{f} = \arg\max_{f} \left| \frac{1}{N}\mathrm{DFT}\,[\mathbf{x}_1] \right|^2 \tag{4.6}$$

$$\hat{\sigma}_s^2 = \left| \frac{1}{N}\mathrm{DFT}\,[\mathbf{x}_1] \right|^2_{f=\hat{f}}. \tag{4.7}$$

The associated angle, frequency, and SNR CRLBs as a function of the SNR and number of samples of the received signals are

$$\mathrm{CRLB}\left(\hat{\phi}\right) = \frac{\eta^{-1} + 4}{\eta N 4^2(\pi/2)^2\sin^2(\pi/4)(\pi/180)^2} \tag{4.8}$$

$$\mathrm{CRLB}\left(\hat{f}\right) = \frac{6}{\eta\left(N^3 - N\right)(2\pi)^2} \tag{4.9}$$

$$\mathrm{CRLB}\left(\hat{\eta}\right) = \frac{1}{2N}. \tag{4.10}$$

The following figures report the variance of the angle, frequency, and SNR estimators of noisy signals over a range of N and η values. Each variance is calculated from 3,000 independent MCS trials per N and η value, where N ranges from 10 to 1,000 samples and

η ranges from -20 to 30 dB. At each grid point, the associated CRLB is calculated for performance comparison.

The surface plot shown in Figure 4.1 reports the performance of the frequency MLE compared to the frequency CRLB over the range of N and η values. At low values of N and η, the MLE variance approaches a value of $1^2/12 = 8.33 \times 10^{-2}$, which is the variance of a uniform random variable ranging from 0 to 1. The values of N and η where the variance of the frequency MLE approaches the CRLB is defined as the frequency estimator performance threshold. Cross sections of Figure 4.1 at constant values of $N = 170$ samples and $\eta = -4$ dB are shown in Figures 4.2 and 4.3 respectively.
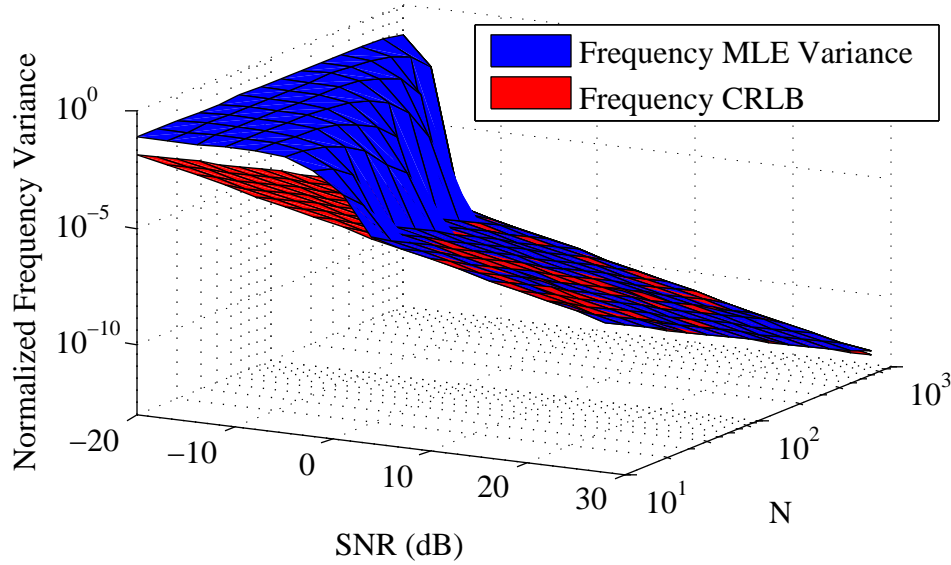
Figure 4.1: Performance of the frequency MLE compared to the frequency CRLB as a function of SNR and N.
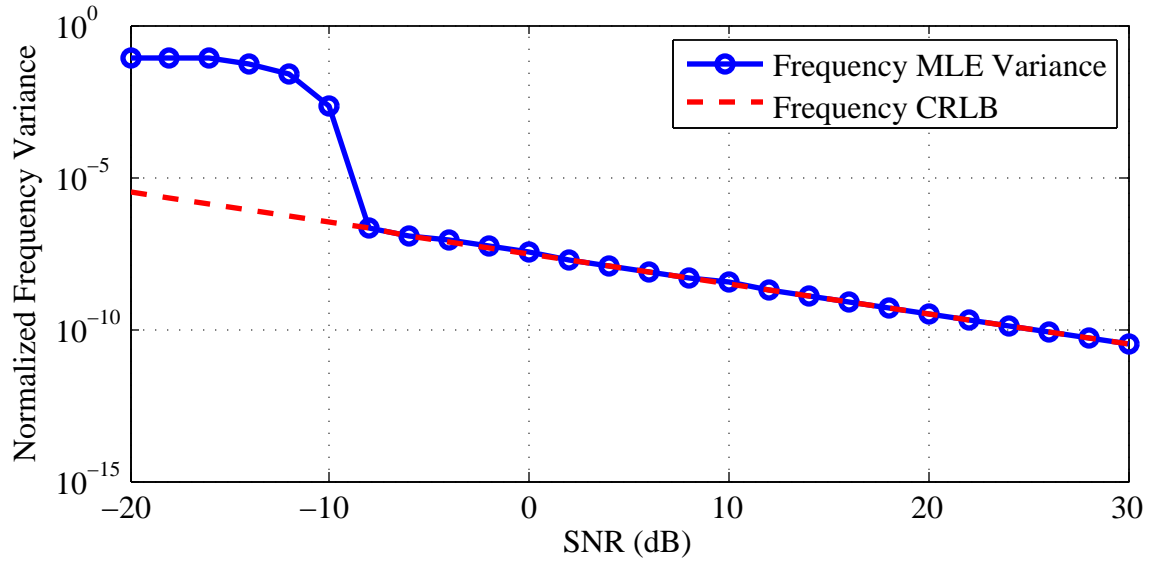
Figure 4.2: Performance of the frequency MLE compared to the frequency CRLB as a function of SNR with constant $N = 170$ samples.
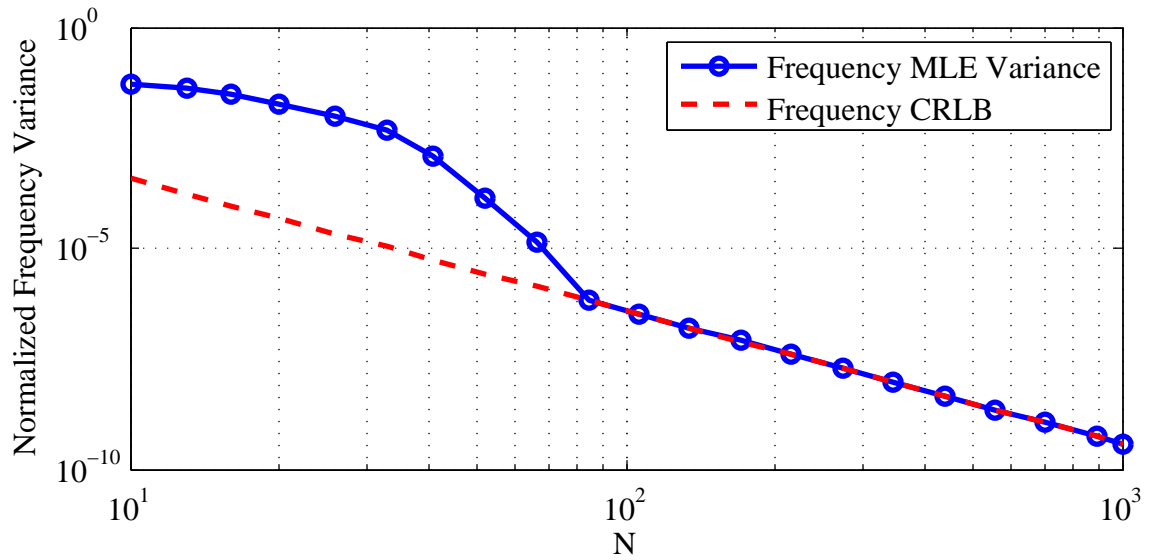
Figure 4.3: Performance of the frequency MLE compared to the frequency CRLB as a function of N with constant SNR $= -4$ dB.

71

The surface plot shown in Figure 4.4 reports the performance of the azimuth angle MUSIC estimator compared to the azimuth angle CRLB over the range of N and η values. At low values of N and η, the MUSIC variance approaches a value of $360^2/12 = 1.08 \times 10^4$, which is the variance of a uniform random variable ranging from 0 to 360. The MUSIC variance is less than the angle CRLB at low values of N and η because the angle CRLB assumes a Gaussian distribution rather than the uniform distribution. The values of N and η where the variance of the MUSIC angle estimator approaches the CRLB is defined as the angle estimator performance threshold. Cross sections of Figure 4.4 at constant values of $N = 20$ samples and $\eta = -10$ dB are shown in Figures 4.5 and 4.6 respectively.
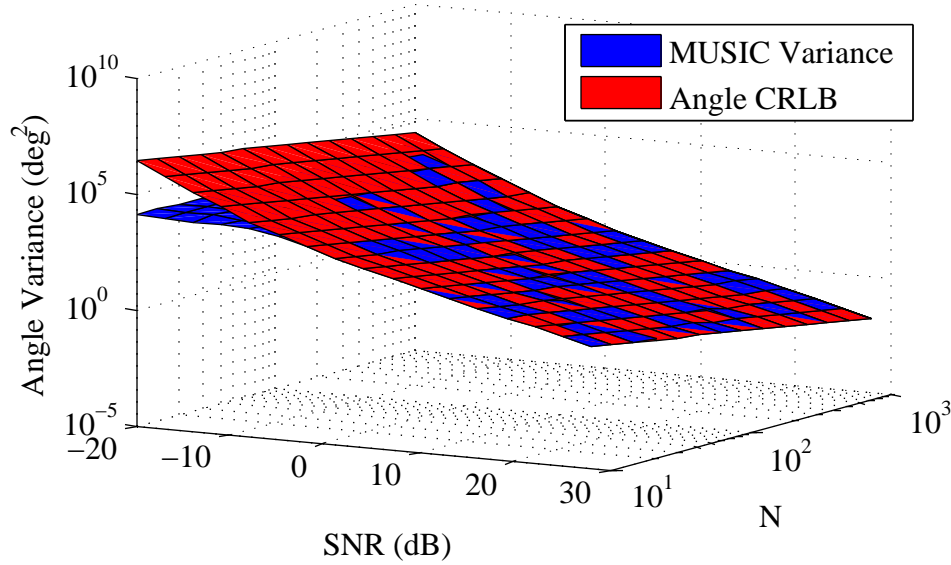
Figure 4.4: Performance of the MUSIC azimuth angle estimator compared to the azimuth angle CRLB as a function of SNR and N.
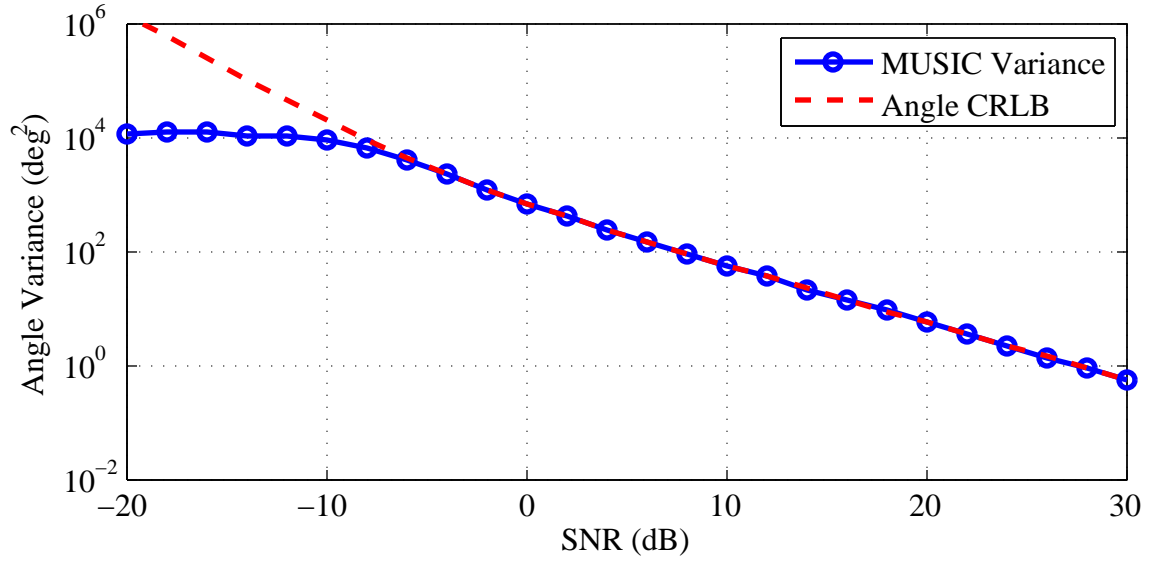
Figure 4.5: Performance of the MUSIC azimuth angle estimator compared to the azimuth angle CRLB as a function of SNR with constant $N = 20$ samples.
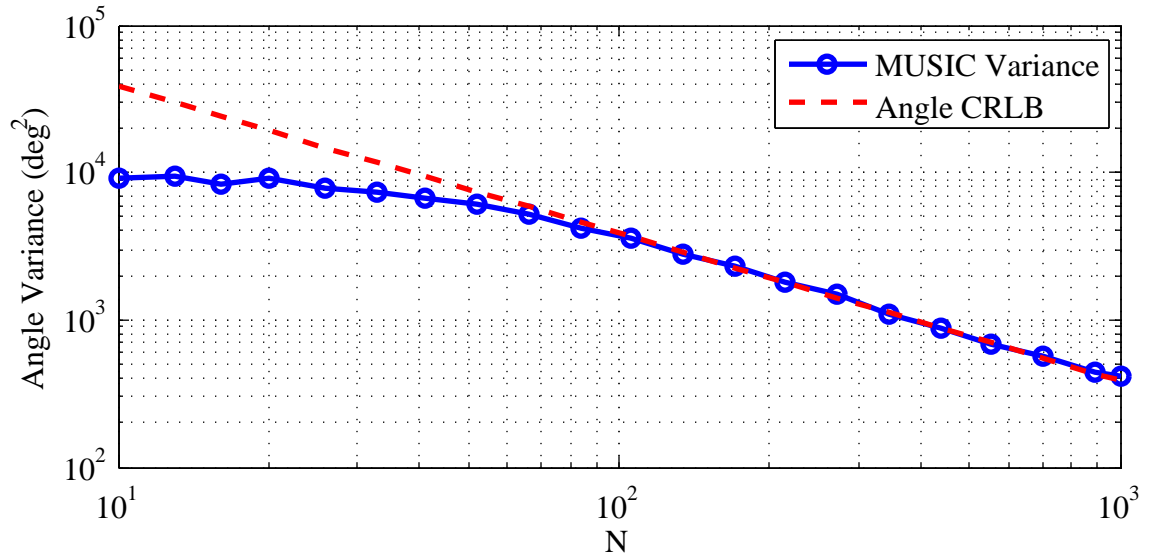
Figure 4.6: Performance of the MUSIC azimuth angle estimator compared to the azimuth angle CRLB as a function of N with constant SNR = -10 dB.

The surface plot shown in Figure 4.7 reports the performance of the SNR MLE compared to the SNR CRLB over the range of N and η values. The SNR MLE variance is less than the SNR CRLB at low values of N and η because the SNR CRLB is only valid for unbiased estimates. The values of N and η where the variance of the SNR MLE approaches the CRLB is defined as the SNR estimator performance threshold. Cross sections of Figure 4.7 at constant values of $N = 170$ samples and $\eta = -10$ dB are shown in Figures 4.8 and 4.9 respectively.
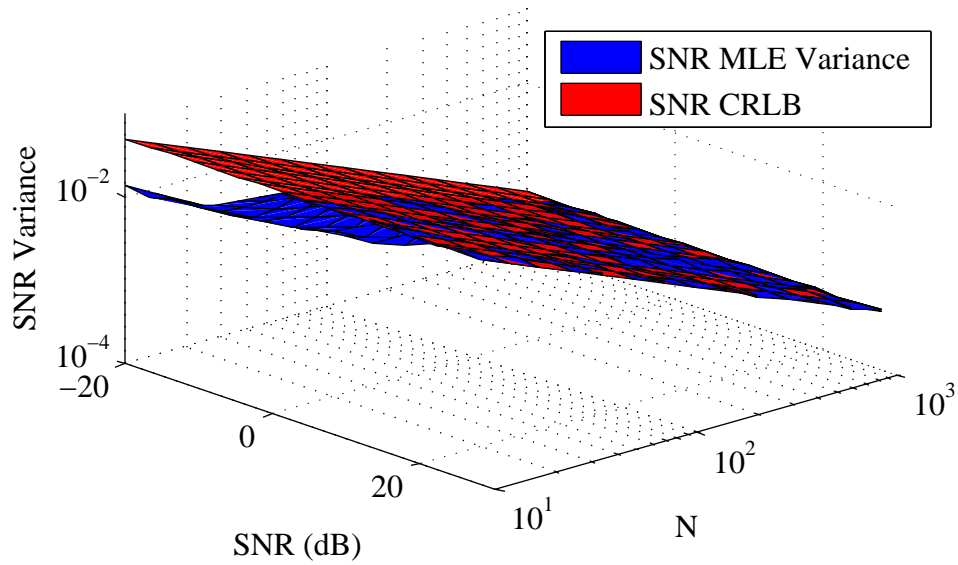
Figure 4.7: Performance of the SNR MLE compared to the SNR CRLB as a function of SNR and N.
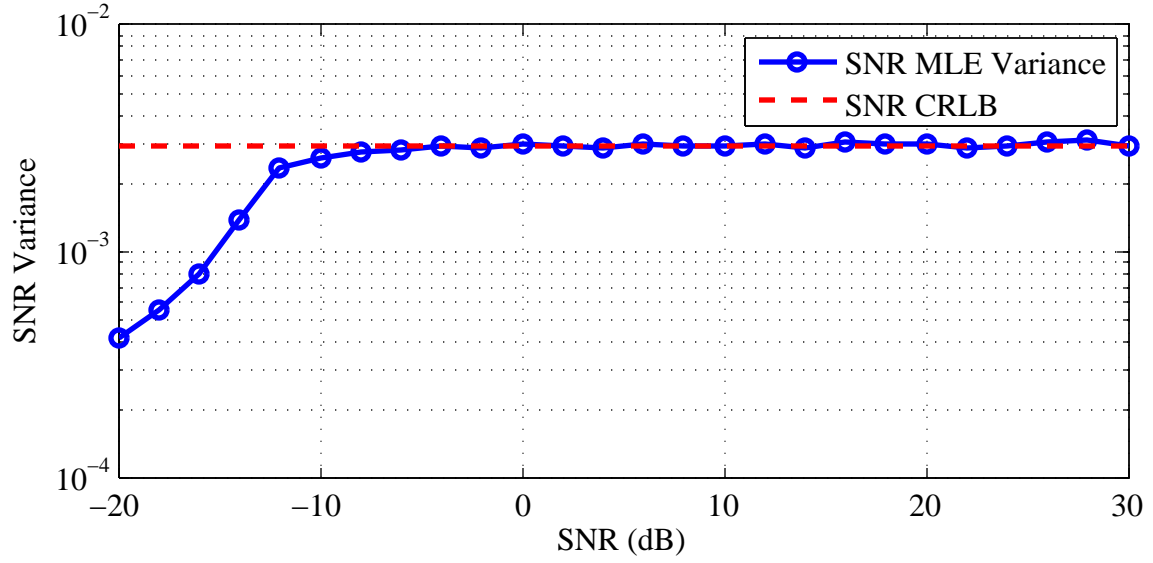
Figure 4.8: Performance of the SNR MLE compared to the SNR CRLB as a function of SNR with constant $N = 170$ samples.
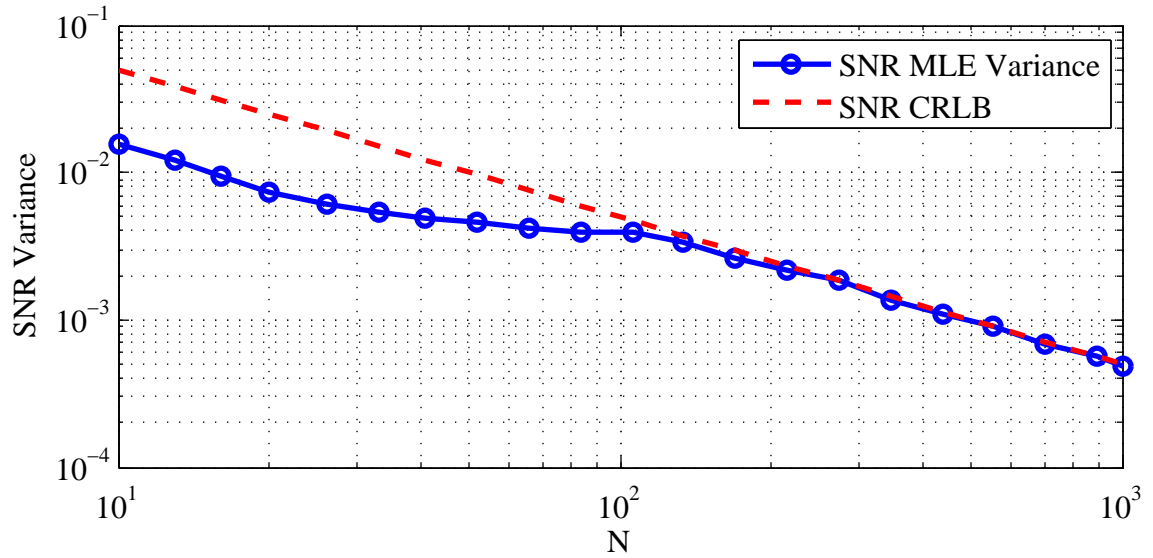
Figure 4.9: Performance of the SNR MLE compared to the SNR CRLB as a function of N with constant SNR $= -10$ dB.

The ratios of the estimator variances to the corresponding CRLBs of Figures 4.1, 4.4, and 4.7 are expressed in dB ($10\log_{10}$ [variance/CRLB]) and are shown in Figures 4.10 through 4.12 for the frequency, angle, and SNR estimators performance, respectively. The ±1 dB contours of the ratio plots are shown in Figure 4.13 where the value of the estimator variance is within 1 dB of the associated CRLB. The frequency contour plot is similar to [41]. As long as the values of N and η are within the region to the right of the frequency 1 dB threshold contour, the use of Gaussian distributed signal parameter estimates in the geolocation algorithm simulation with the variances defined by the associated CRLB as described in Section 3.5.2 is justified.
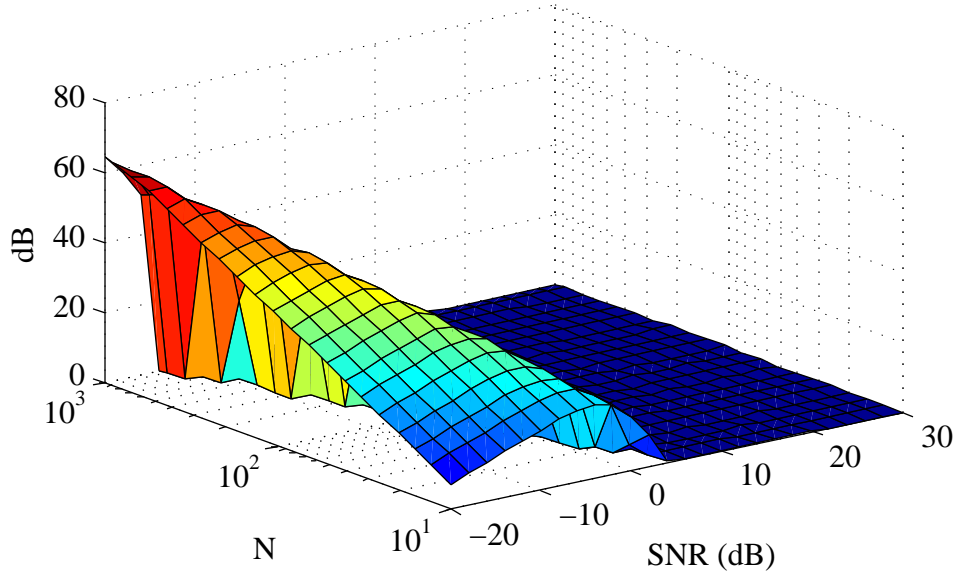
Figure 4.10: Ratio of the frequency MLE variance to the frequency CRLB, expressed in dB, over the range of N and SNR.
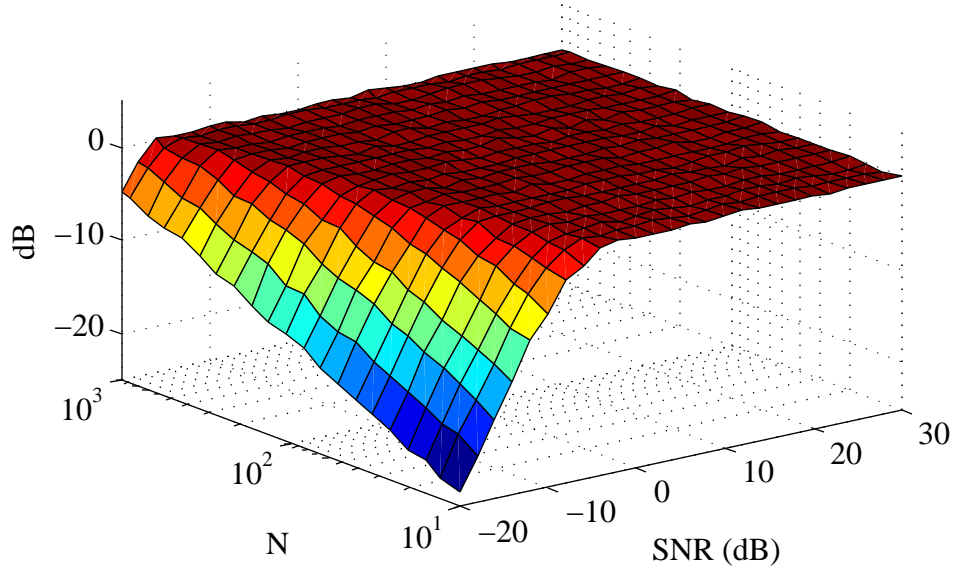
Figure 4.11: Ratio of the MUSIC azimuth angle estimator variance to the angle CRLB, expressed in dB, over the range of N and SNR.
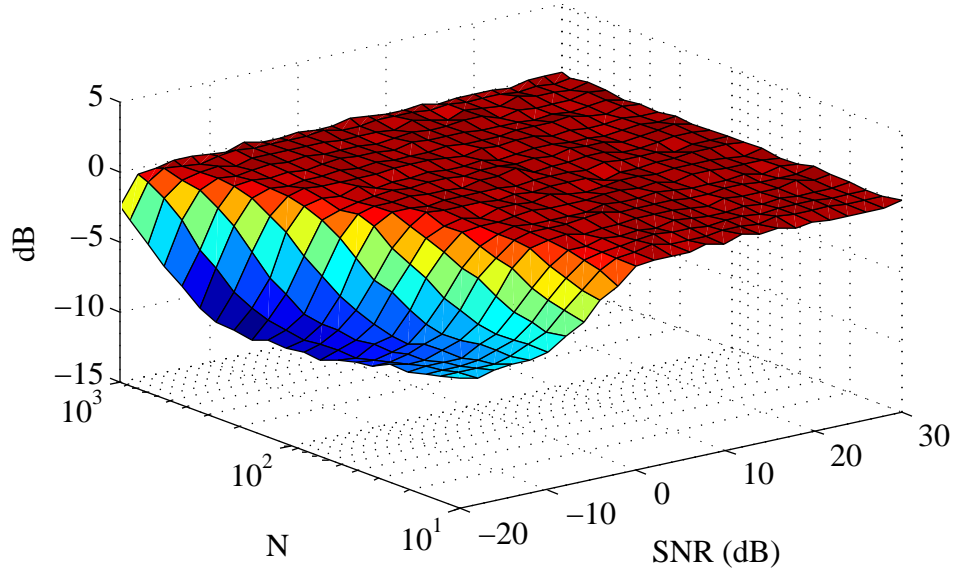
Figure 4.12: Ratio of the SNR MLE variance to the SNR CRLB, expressed in dB, over the range of N and SNR.
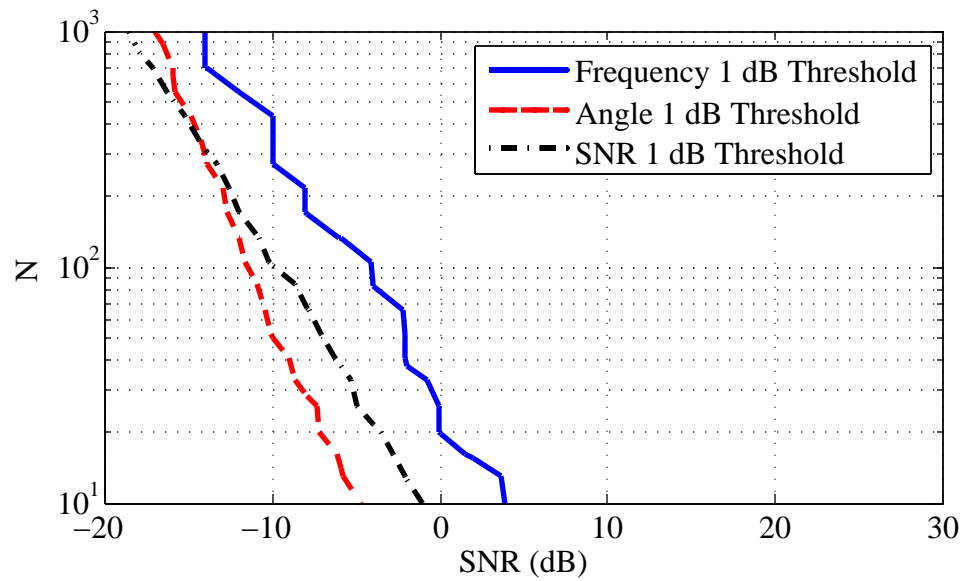
Figure 4.13: Contour plot of the frequency, angle, and SNR estimator performance ratios showing the ±1 dB thresholds.

4.2 Geolocation Algorithm Performance Sensitivity Analysis

This section reports the impact of various system parameter values on the RMSE of the 4 geolocation algorithms used in this thesis. The system parameters include: the orbital pass used in the analysis scenario, number of signal collects during the pass, number of samples per signal collect, SNR at the first signal collect, frequency knowledge error, attitude knowledge error, position knowledge error, and velocity knowledge error. The spinning radar, burst communications, and continuous communications emitter types are used for the sensitivity analysis which is implemented as the geolocation simulation described in Section 3.5.2. The following default system parameters are used for all 3 emitter types: pass number 7, 5 Hz frequency knowledge error, 0.2 deg attitude knowledge error, 10 m position knowledge error, and 1 m/s velocity knowledge error. A sampling frequency of 400 kHz (T_s = 2.5 µs) is used for the simulated frequency estimates. The system parameter under consideration is varied while the others are held fixed for each scenario. The RMSE of the 4 geolocation algorithms is calculated from 3,000 independent MCS trials per point and compared to the corresponding CRLB.

The spinning radar emitter considered in Section 4.2.1 is implemented with the following parameters: 20 dB SNR at the first signal collect, 100 samples per signal collect, and 10 seconds between signal collects.

The burst communications emitter considered in Section 4.2.2 is implemented with the following parameters: 10 dB SNR at the first signal collect, 400 samples per signal collect, and 30 seconds between signal collects.

The continuous communications emitter considered in Section 4.2.3 is implemented with the following parameters: 0 dB SNR at the first signal collect, 800 samples per signal collect, and 1 second between signal collects.

The geolocation performance of the AOA/FOA geolocation MLE for the 3 emitter types is compared in Section 4.2.4.

4.2.1 Spinning Radar Emitter Sensitivity Analysis.

Figure 4.14 reports the RMSE of the 4 geolocation algorithms and associated CRLBs for the 11 orbital passes in the analysis scenario. The orbital pass impacts the position, velocity, and total number of signal collects used by the geolocation algorithms. The AOA LS intersection has similar performance to the AOA MLE for passes 1-4 due to similar valued angle measurement variances and relatively low number of total signal collects. As the number of signal collects increases with a wider range of estimate variances for weighting of the angle measurements, the AOA MLE has lower RMSE than the AOA LS. The AOA/FOA MLE geolocation algorithm has a lower RMSE than the other 3 algorithms for all passes.
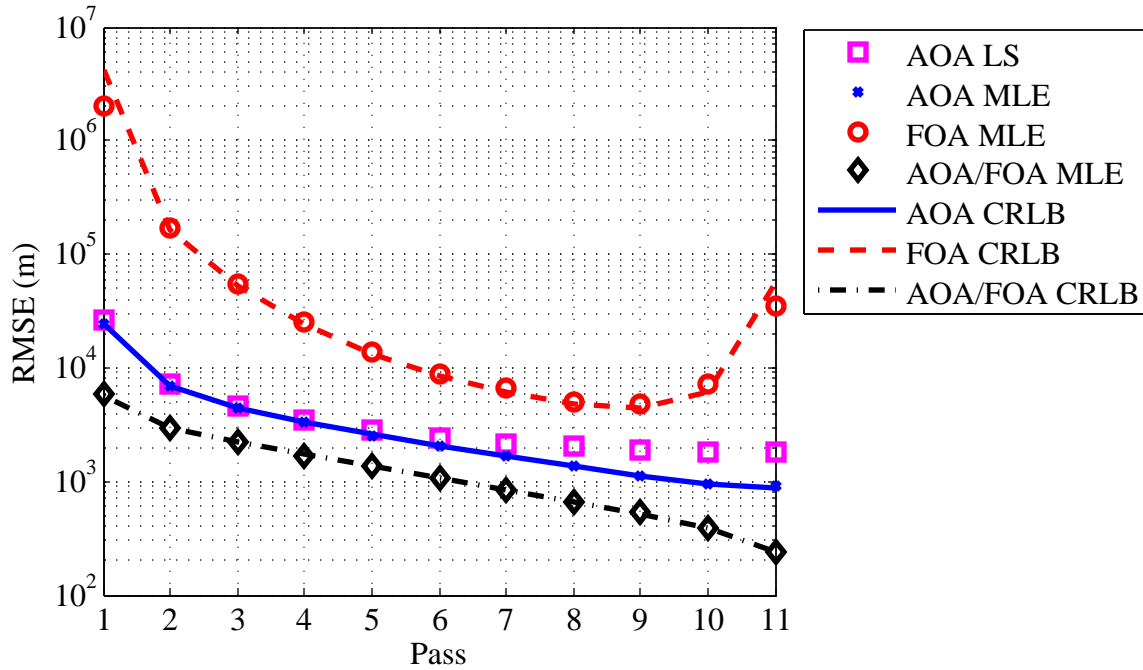
Figure 4.14: Sensitivity analysis of varying the orbital passes with the spinning radar emitter.

Figure 4.15 reports the RMSE as the total number of signal collects out of a possible 39 total signal collects for pass number 7 is varied. The RMSE of all 4 algorithms decreases as the number of signal collects increases and begins to level out around 25/39 signal collects. The AOA/FOA MLE geolocation algorithm has the lowest RMSE throughout.
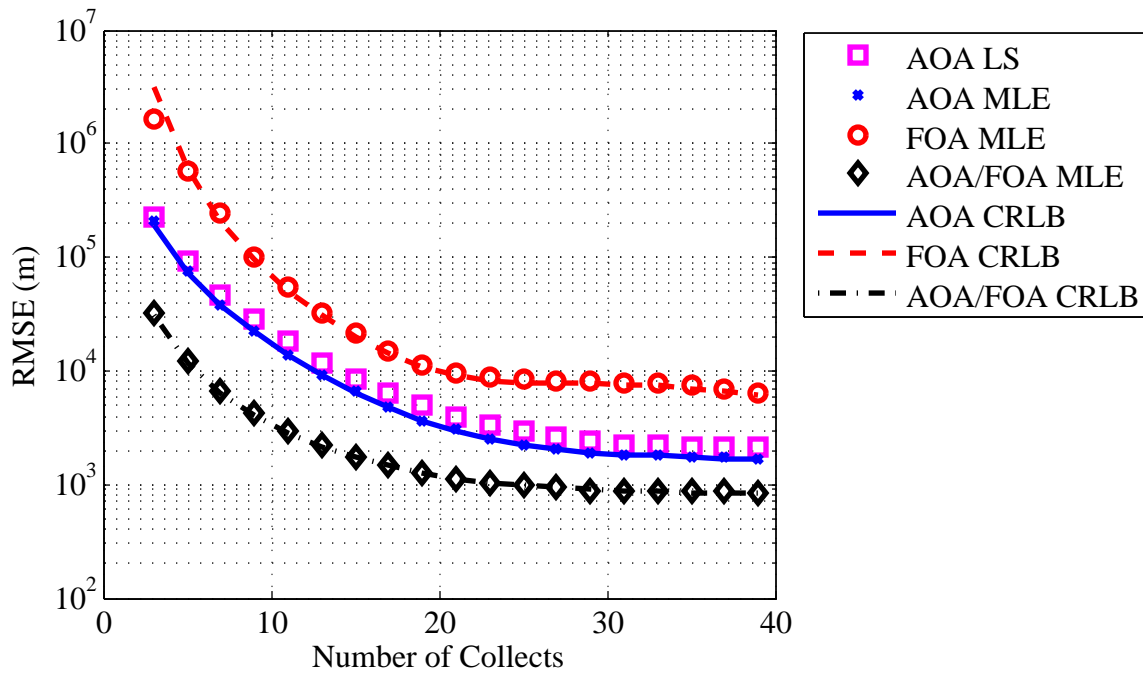
Figure 4.15: Sensitivity analysis of varying the number of collects with the spinning radar emitter.

Figure 4.16 reports the RMSE as the number of samples per signal collect is varied. The RMSE decreases as the number of samples per signal collect increases until the frequency, attitude, position, and velocity knowledge errors determine the performance of the algorithms, at which point the RMSE begins to level out. The RMSE of the FOA MLE geolocation algorithm decreases at a greater rate due to the $1/N^3$ term in frequency CRLB. The AOA/FOA MLE geolocation algorithm has the lowest RMSE throughout.
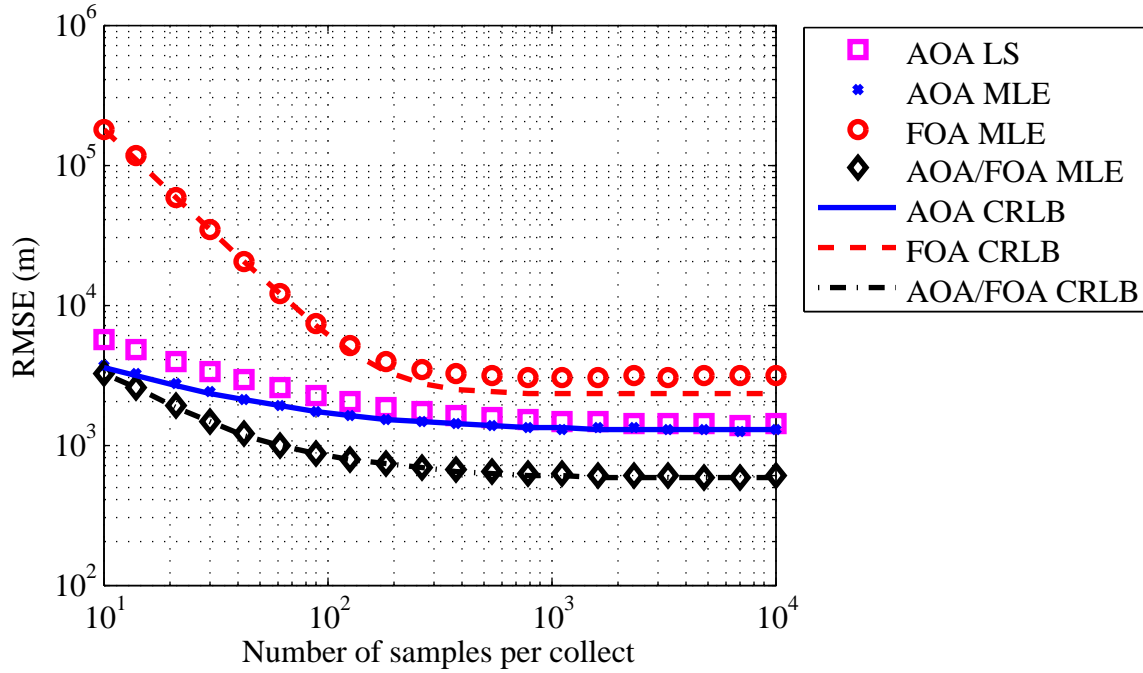
Figure 4.16: Sensitivity analysis of varying the number of samples per signal collect with the spinning radar emitter.

Figure 4.17 reports the RMSE as the SNR at the first signal collect is varied. The RMSE decreases as the SNR increases until the frequency, attitude, position, and velocity knowledge errors determine the performance of the algorithms, at which point the RMSE begins to level out. The AOA/FOA MLE geolocation algorithm has the lowest RMSE throughout.
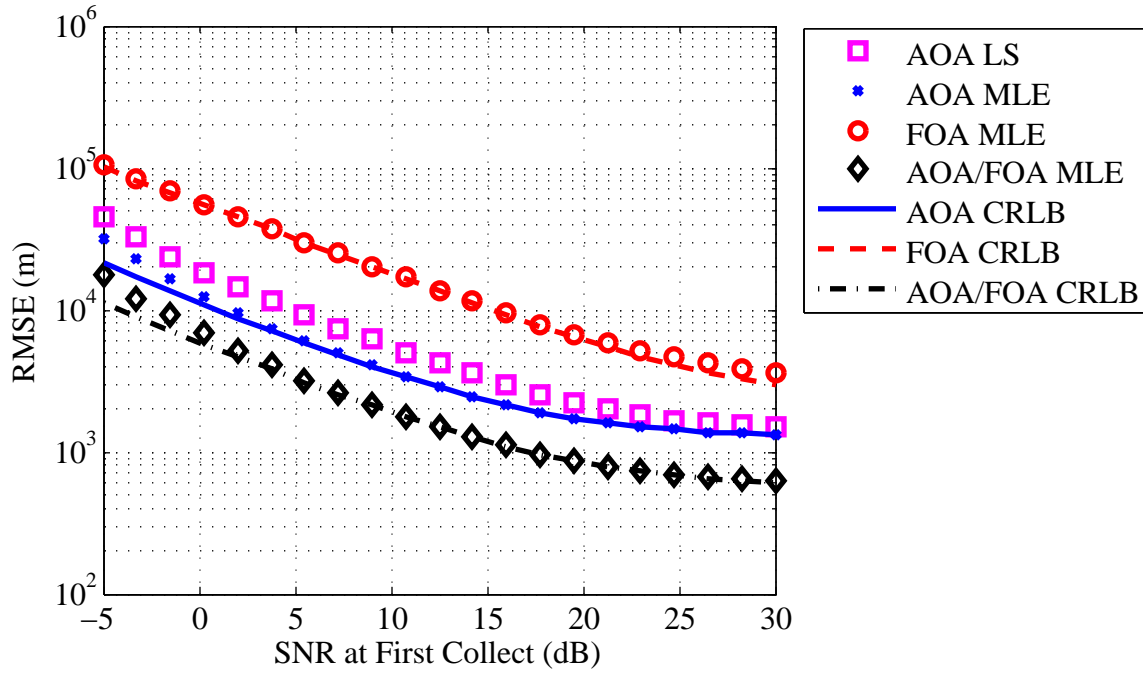
Figure 4.17: Sensitivity analysis of varying the SNR at the first signal collect with the spinning radar emitter.

Figure 4.18 reports the RMSE as the frequency knowledge error standard deviation is varied. The RMSE of the AOA LS and AOA MLE are constant since frequency estimates are not included in those algorithms, while the RMSE increases for the FOA MLE and AOA/FOA MLE algorithms. The AOA/FOA MLE RMSE converges to the AOA MLE RMSE since the variances on the angle estimates are lower than the variances on the frequency estimates.
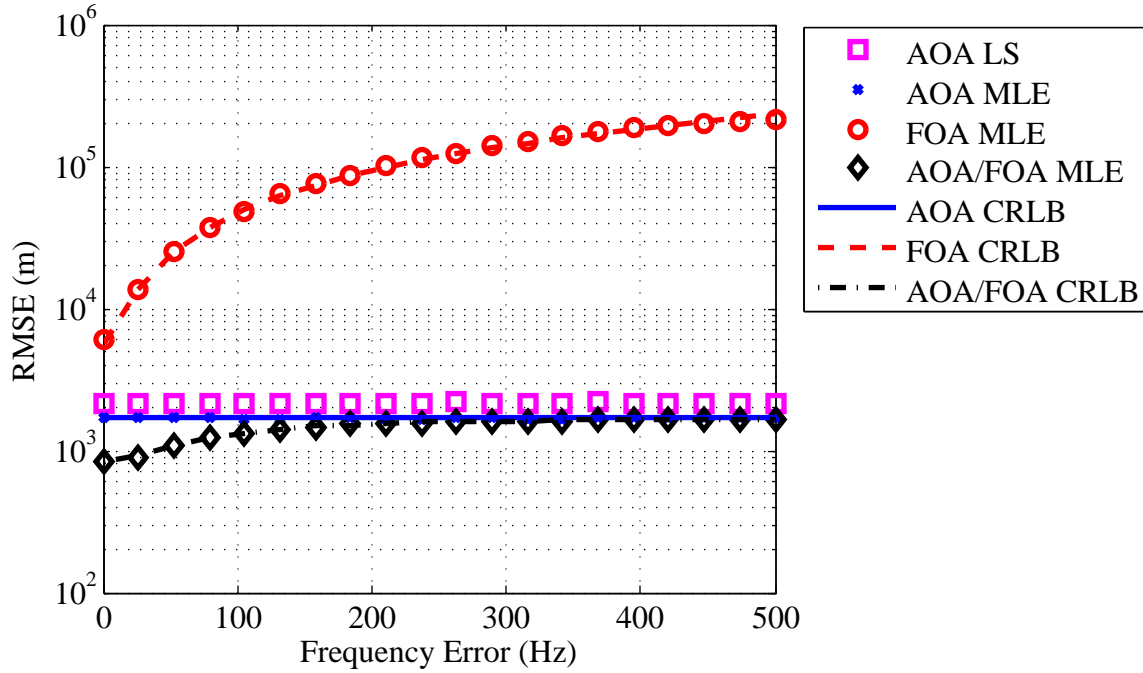
Figure 4.18: Sensitivity analysis of varying the frequency knowledge error standard deviation with the spinning radar emitter.

Figure 4.19 reports the RMSE as the attitude knowledge error standard deviation is varied. The RMSE of the FOA MLE is constant since angle estimates are not included in that algorithm, while the RMSE increases for the AOA LS, AOA MLE, and AOA/FOA algorithms. The AOA/FOA MLE RMSE converges to FOA MLE RMSE since the variance on the frequency estimates are lower than the variance on the angle estimates.
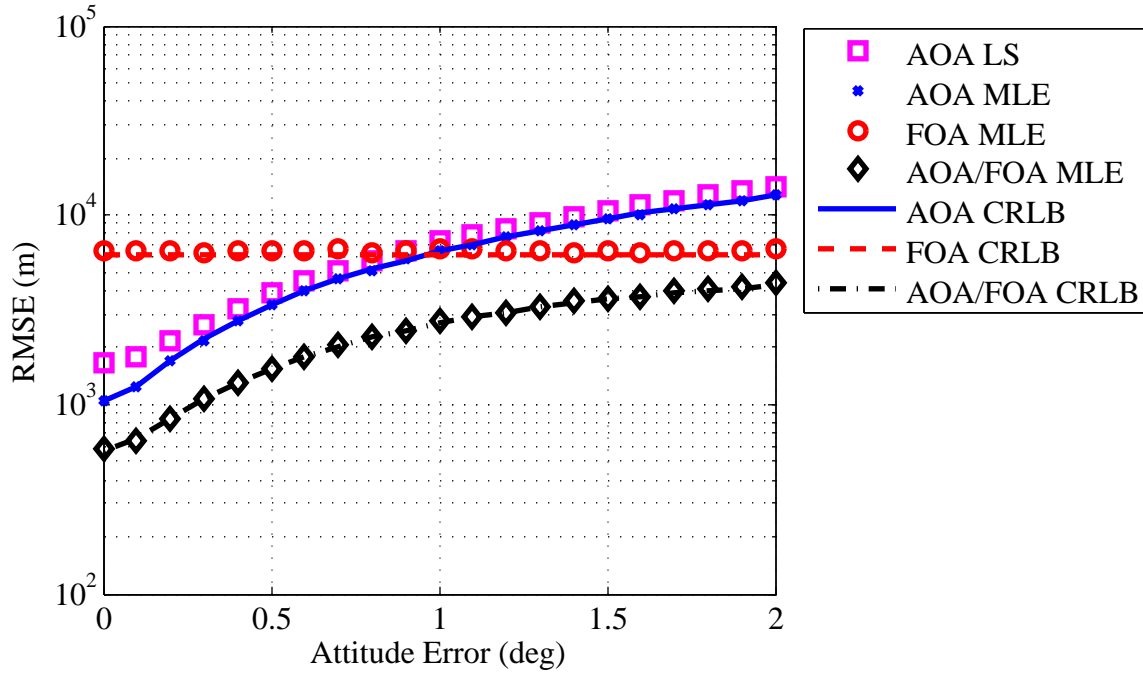
Figure 4.19: Sensitivity analysis of varying the attitude knowledge error standard deviation with the spinning radar emitter.

Figure 4.20 reports the RMSE as the position knowledge error standard deviation is varied. The RMSE is relatively unaffected for all 4 algorithms until 200 m position error, then the RMSE of the FOA MLE begins to increase. The CRLBs used do not include position errors and remain constant. The AOA/FOA MLE geolocation algorithm has the lowest RMSE throughout.
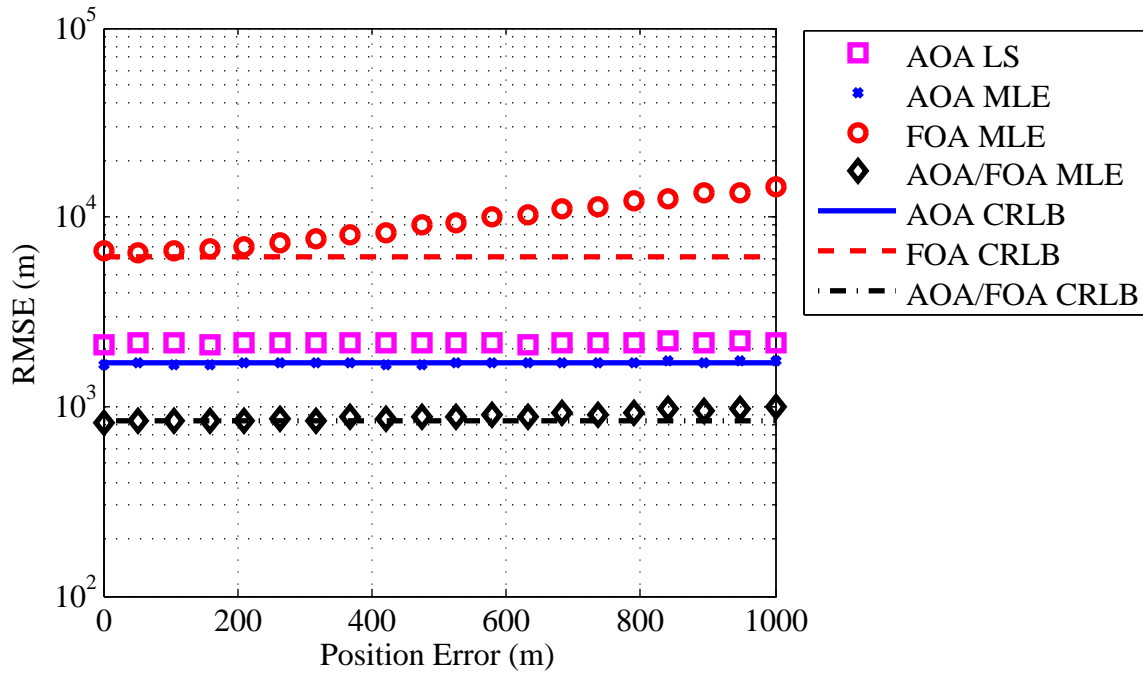
Figure 4.20: Sensitivity analysis of varying the position knowledge error standard deviation with the spinning radar emitter.

Figure 4.21 reports the RMSE as the velocity knowledge error standard deviation is varied. The RMSE increases sharply for the FOA MLE and AOA/FOA MLE algorithms. The RMSE of the AOA LS and AOA MLE algorithms is constant since they do not depend on the velocity of the CubeSat. The CRLBs used do not include velocity errors and remain constant. In the case of relatively large velocity knowledge errors, the AOA LS and AOA MLE algorithms have lower RMSE than the FOA MLE and AOA/FOA MLE algorithms.
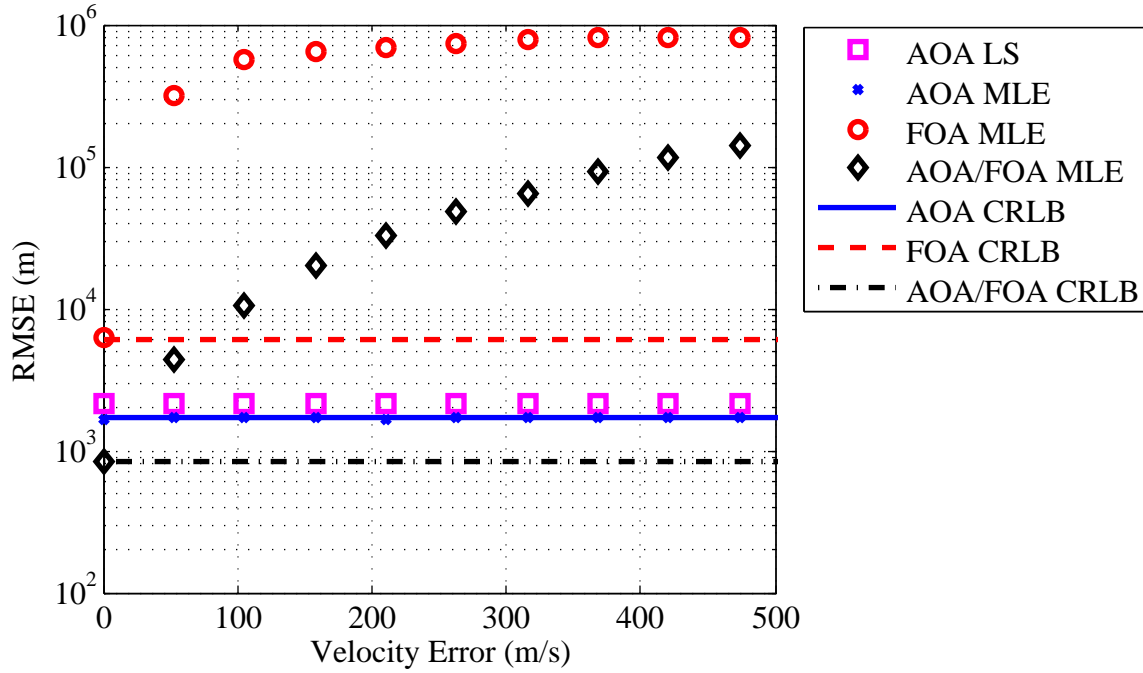
Figure 4.21: Sensitivity analysis of varying the velocity knowledge error standard deviation with the spinning radar emitter.

87

4.2.2 Burst Communications Emitter Sensitivity Analysis.

Simulation results of the sensitivity analysis with the burst communications emitter are reported in Figures 4.22 through 4.29. The parameter sensitivities observed with the burst communications emitter are similar to the spinning radar emitter. The AOA/FOA MLE geolocation algorithm consistently has a lower RMSE than the other 3 geolocation algorithms with the exception of high velocity knowledge errors.
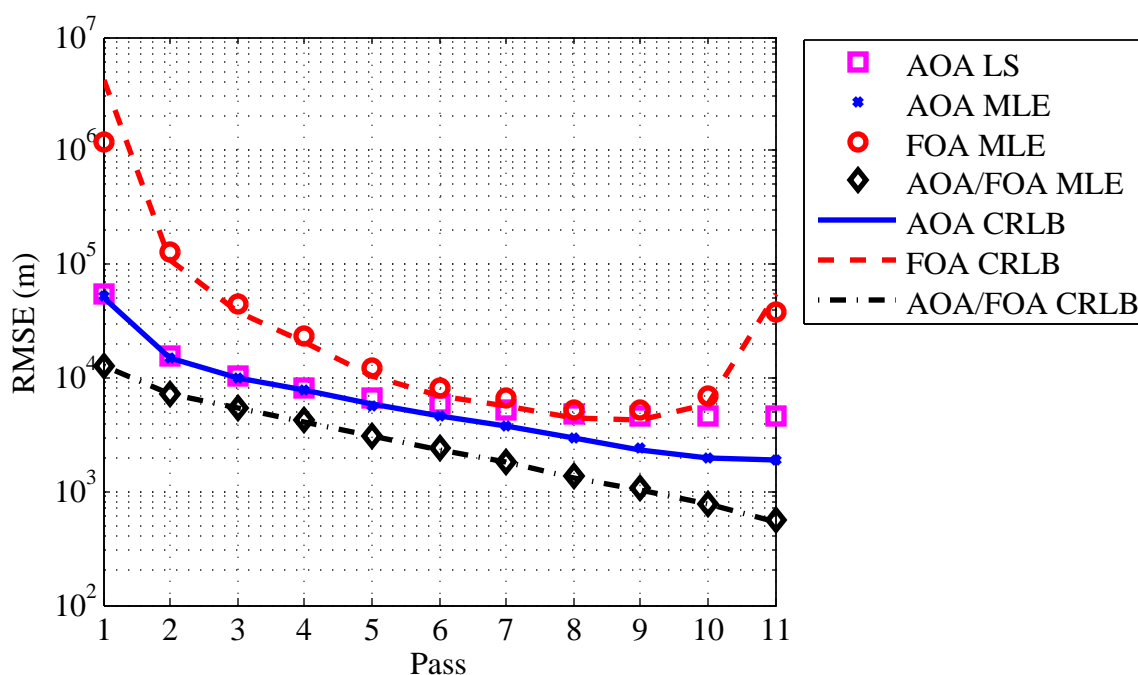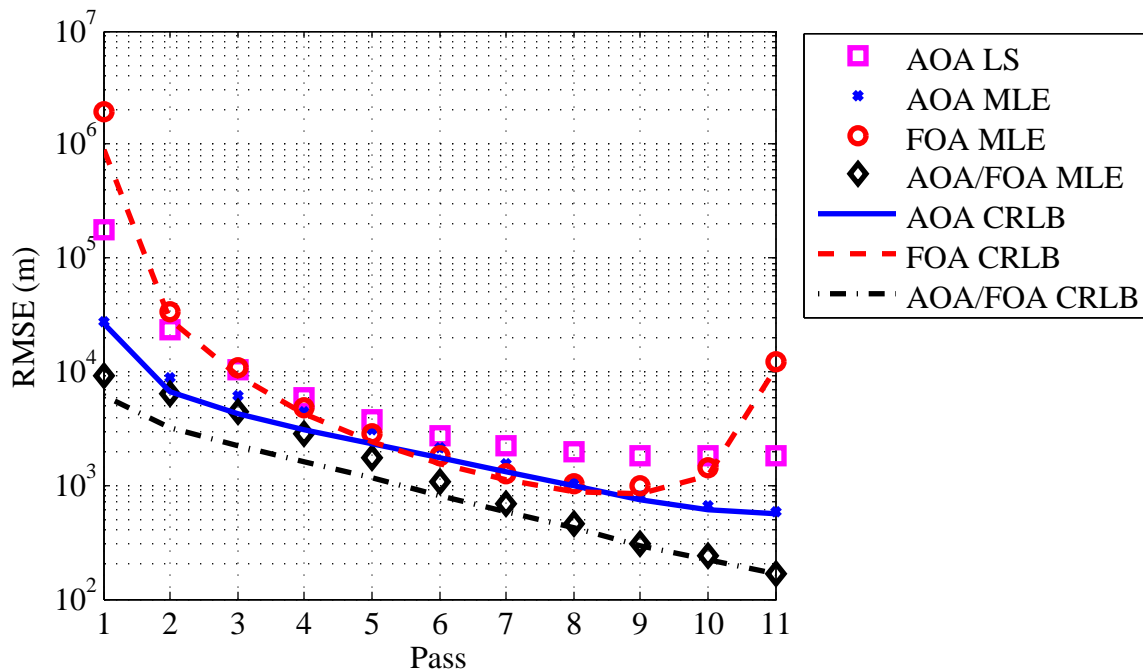

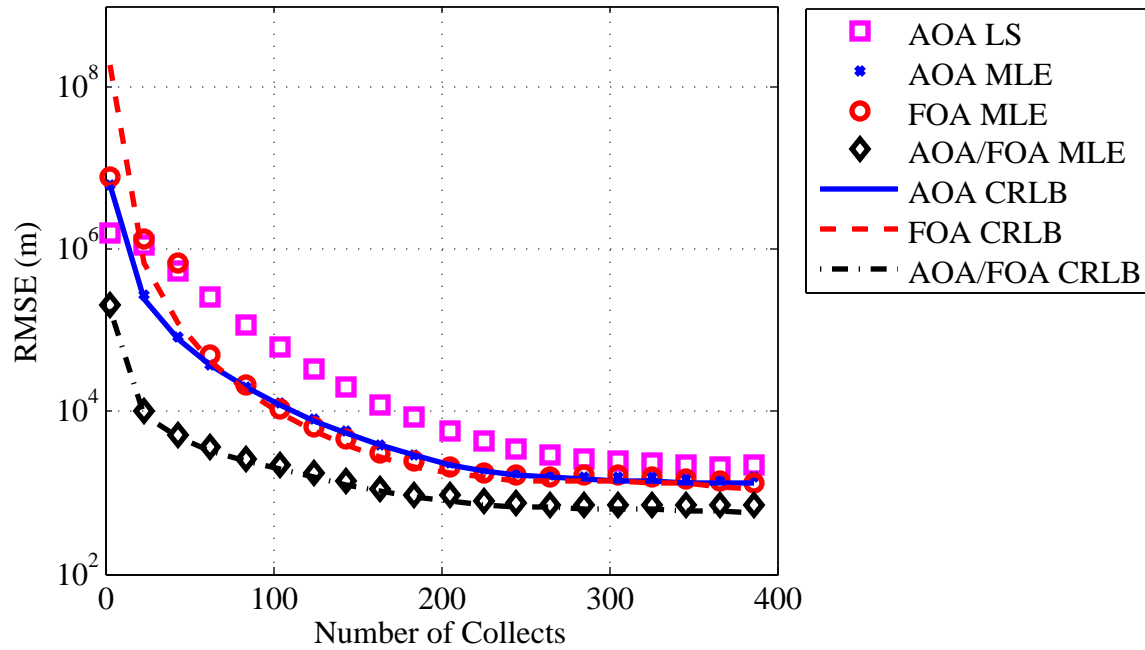Figure 4.22: Orbital pass variation with the burst emitter.
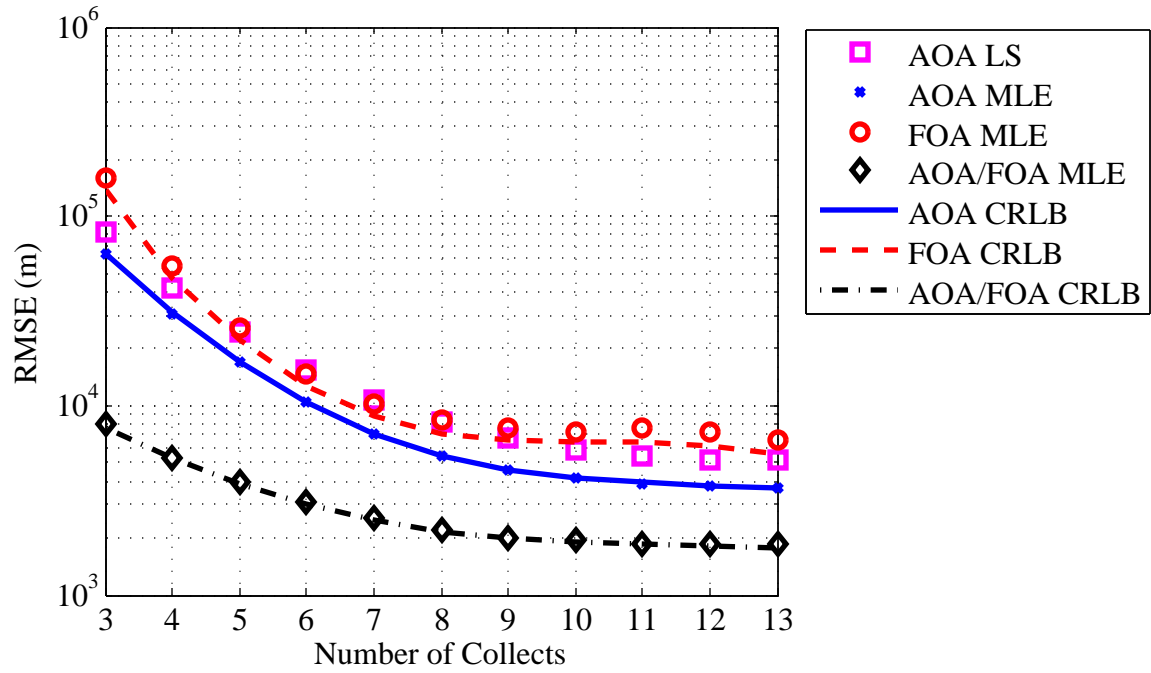
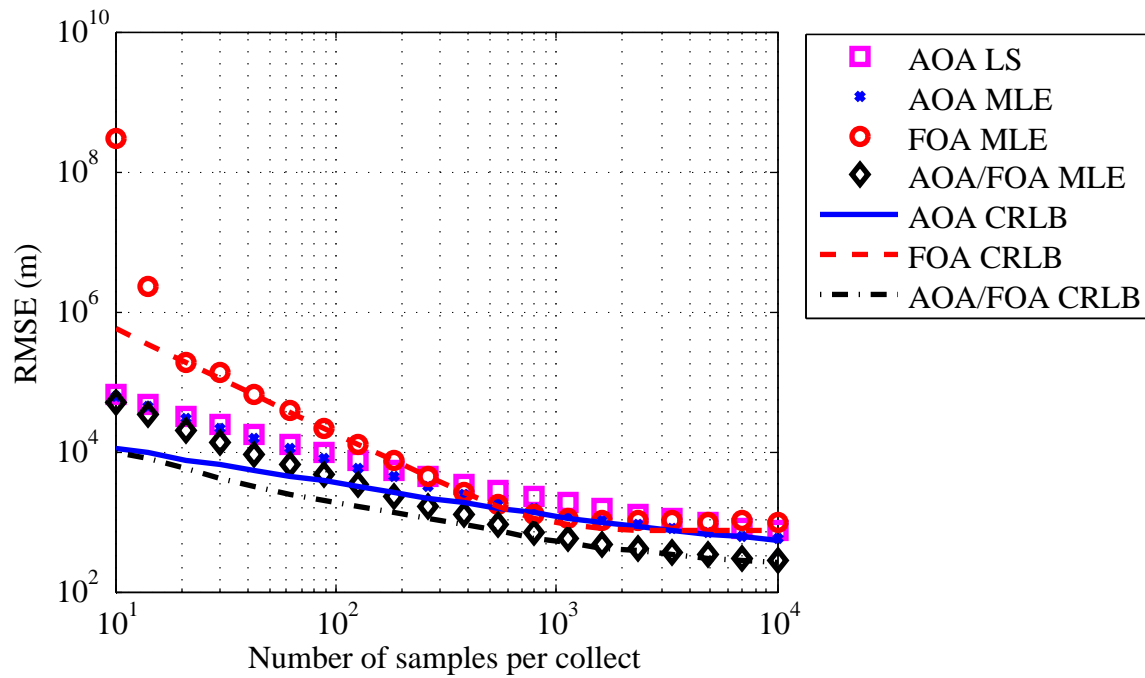Figure 4.23: Number of collects variation with the burst emitter.
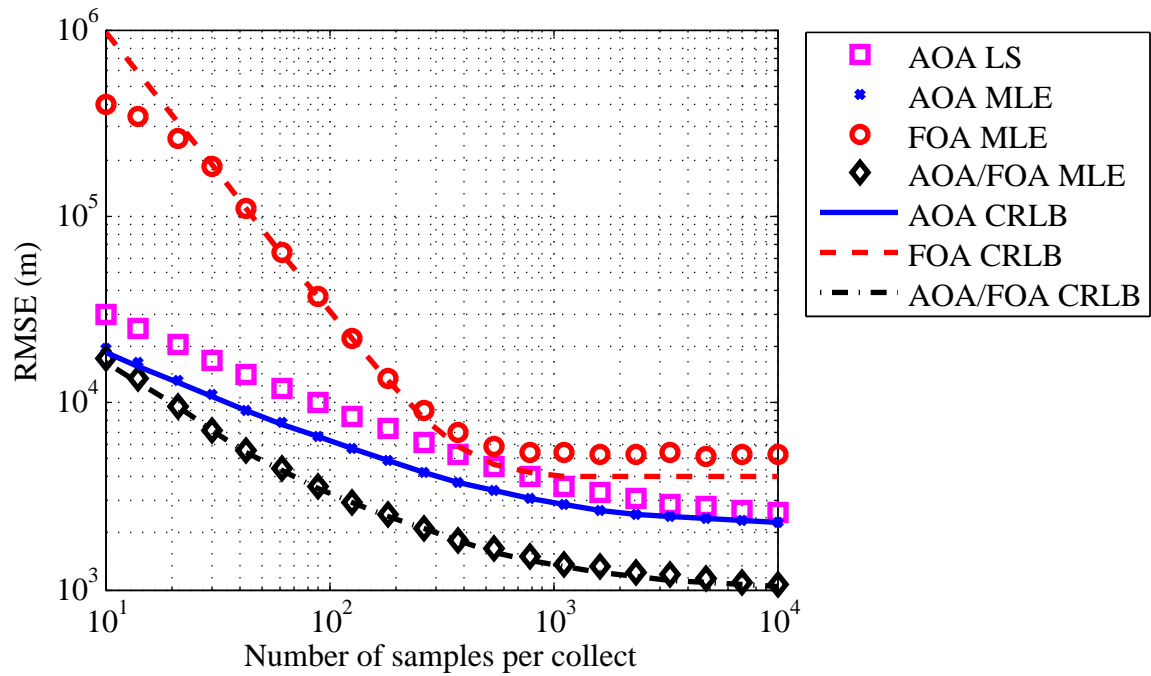
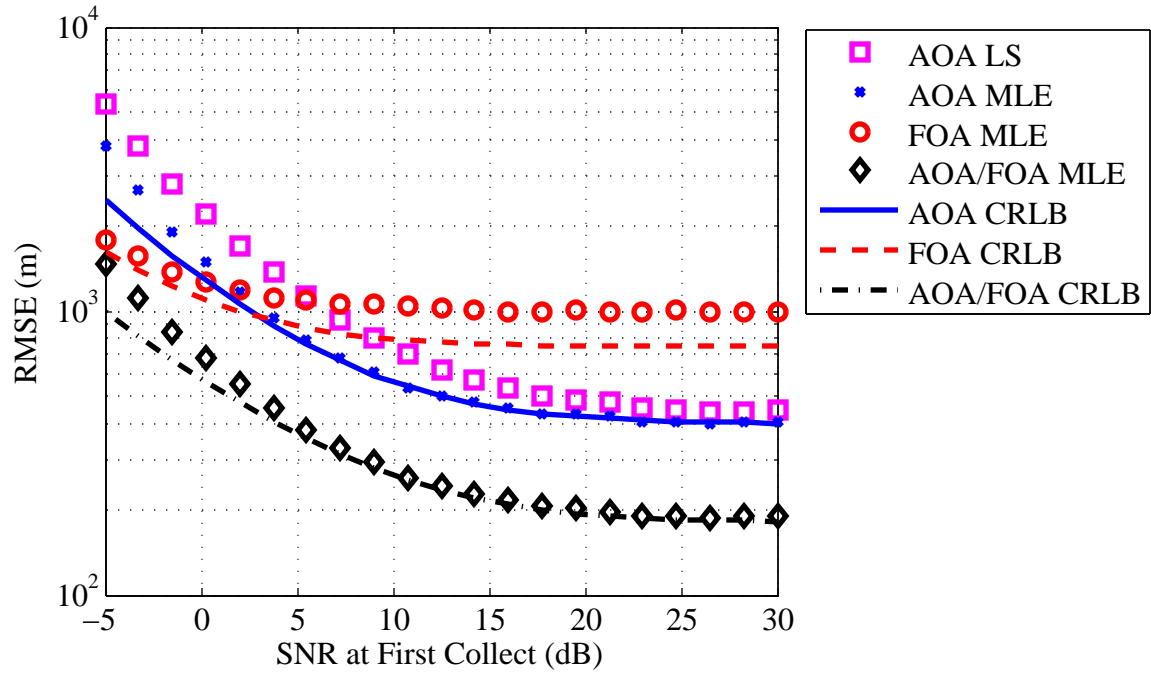Figure 4.24: Number of samples per collect variation with the burst emitter.
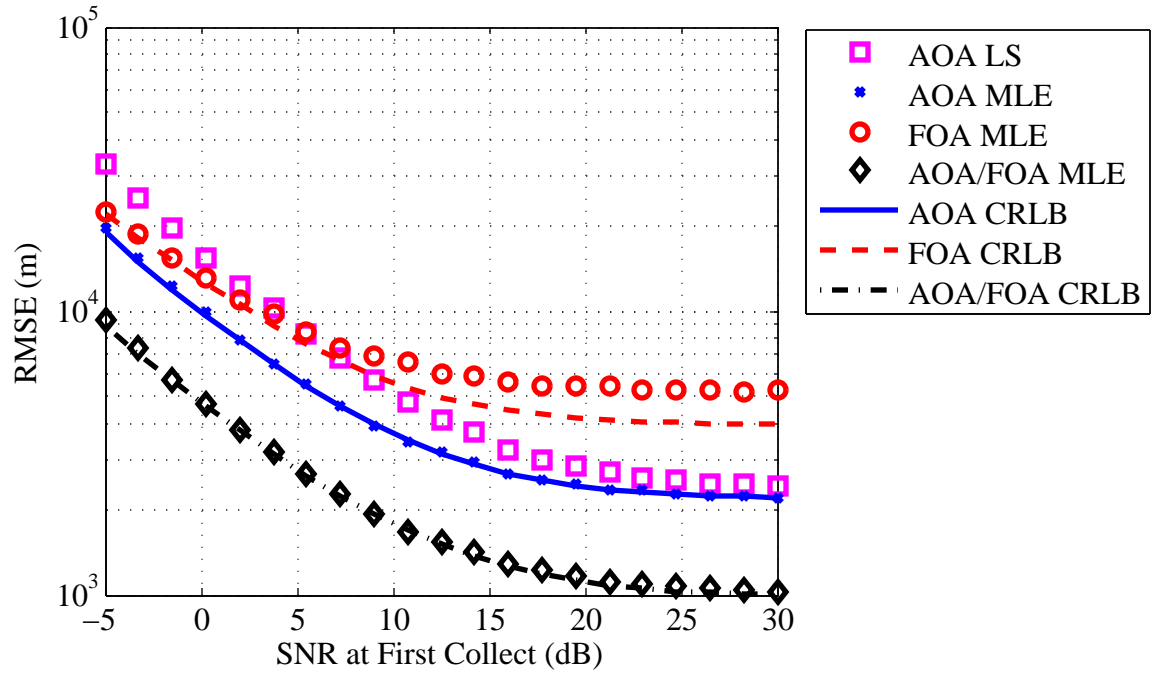
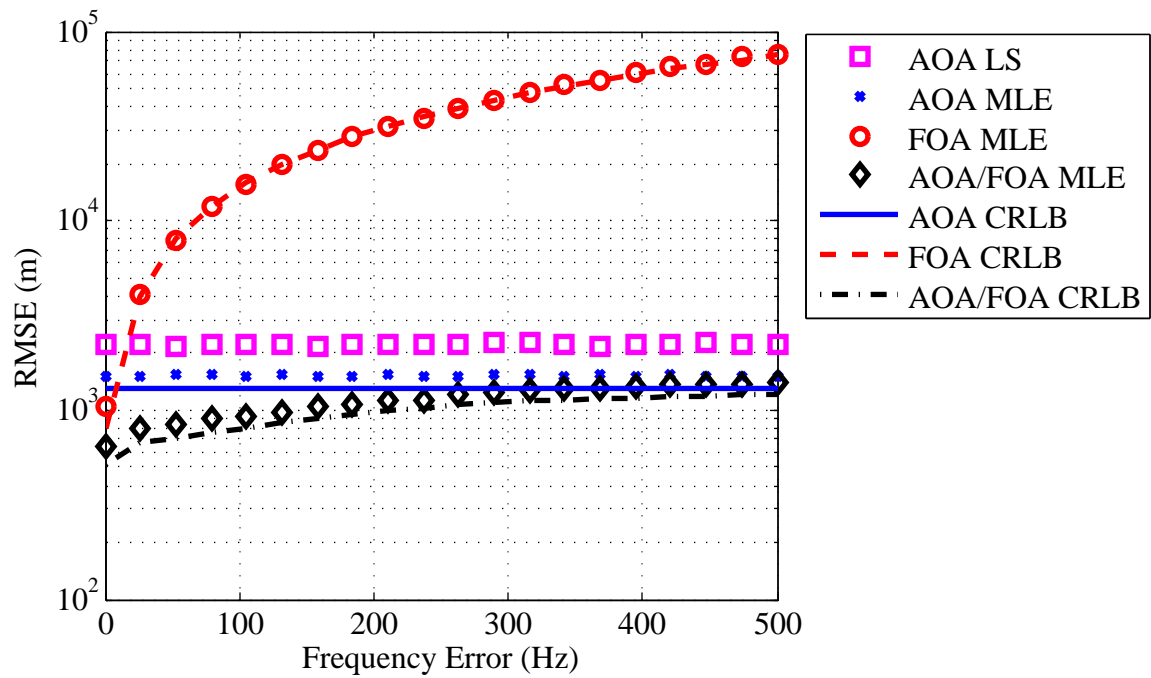Figure 4.25: SNR at the first signal collect variation with the burst emitter.
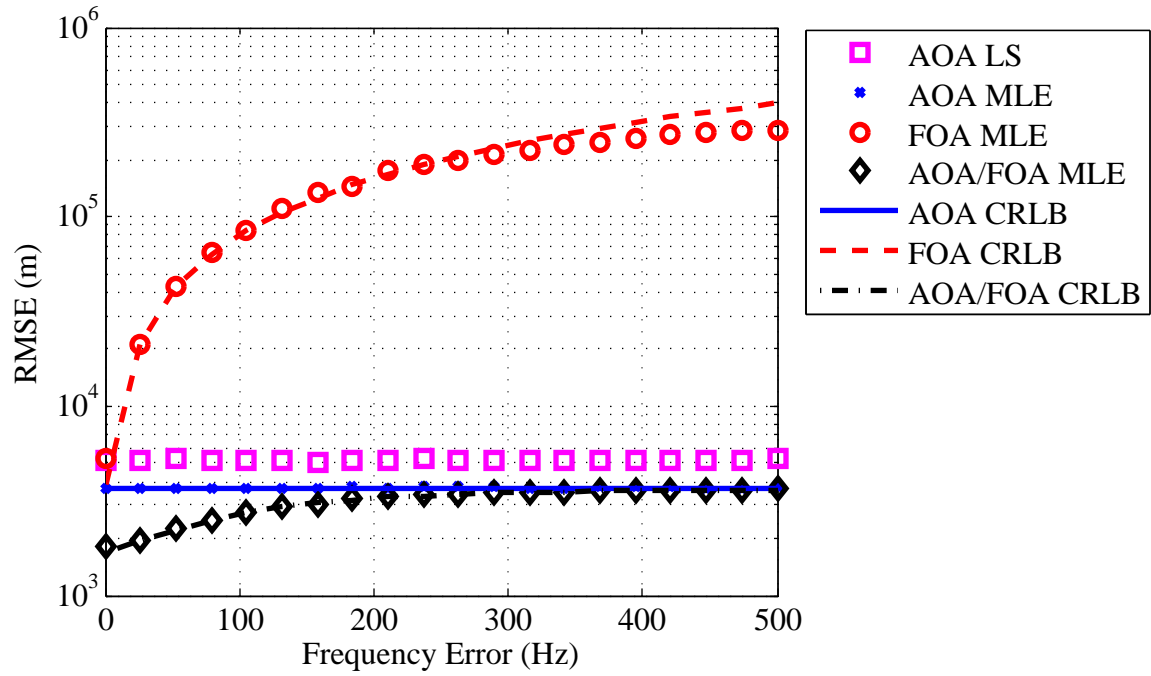
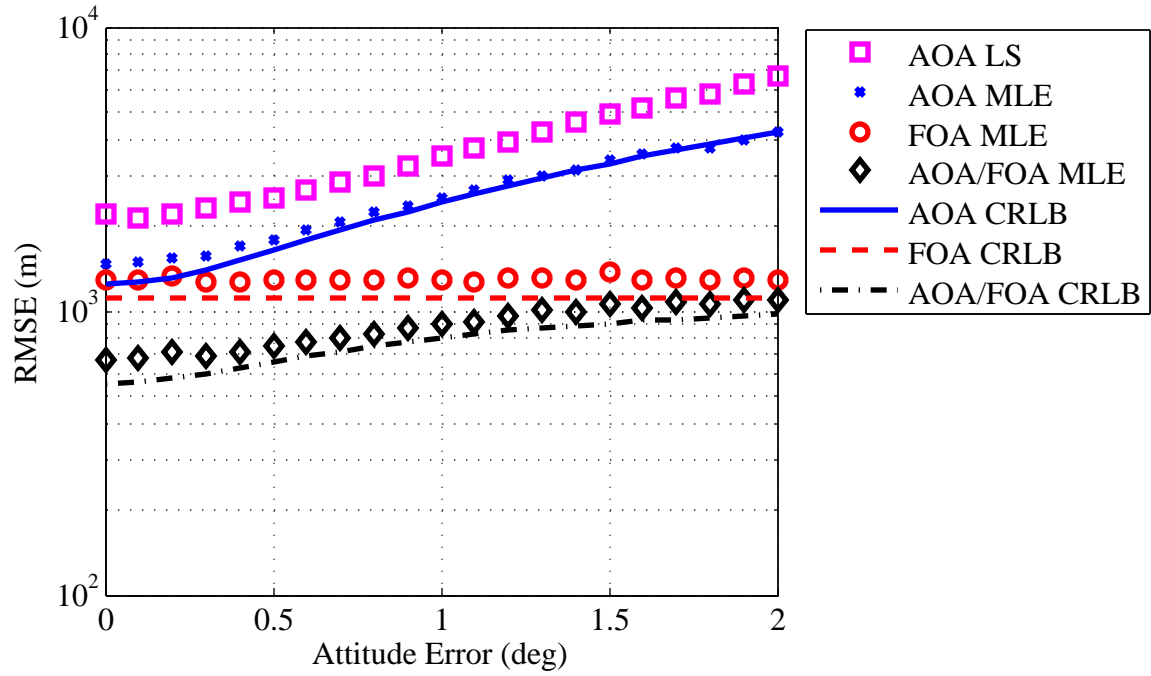Figure 4.26: Frequency knowledge error variation with the burst emitter.
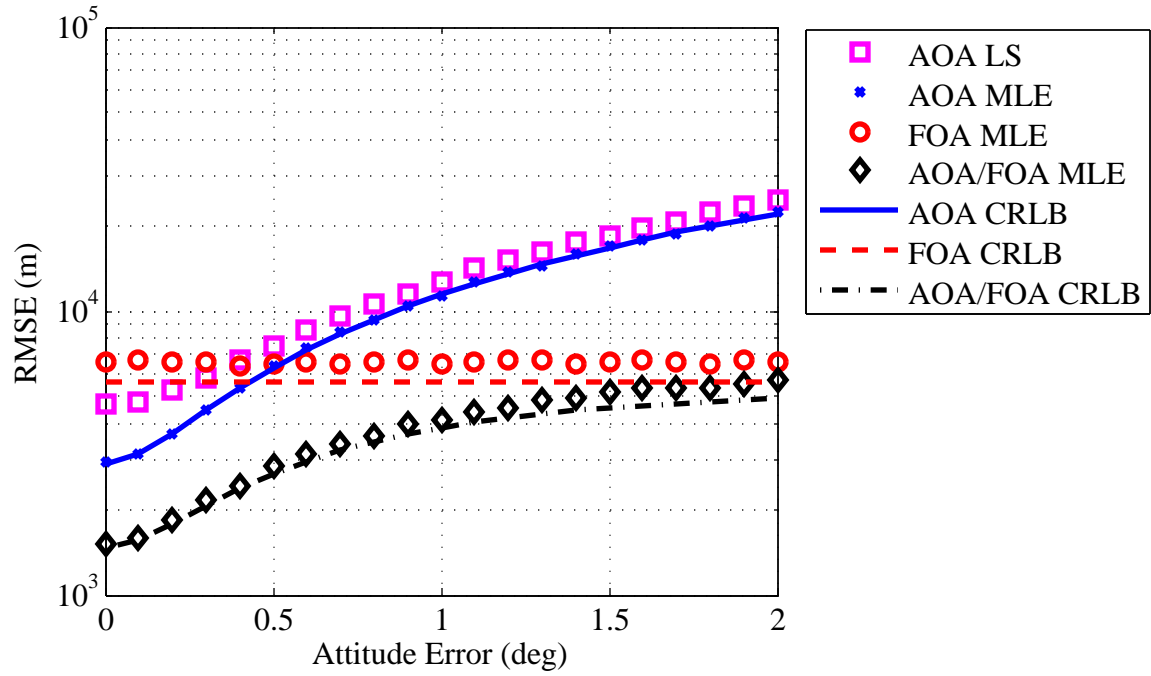
Figure 4.27: Attitude knowledge error variation with the burst emitter.
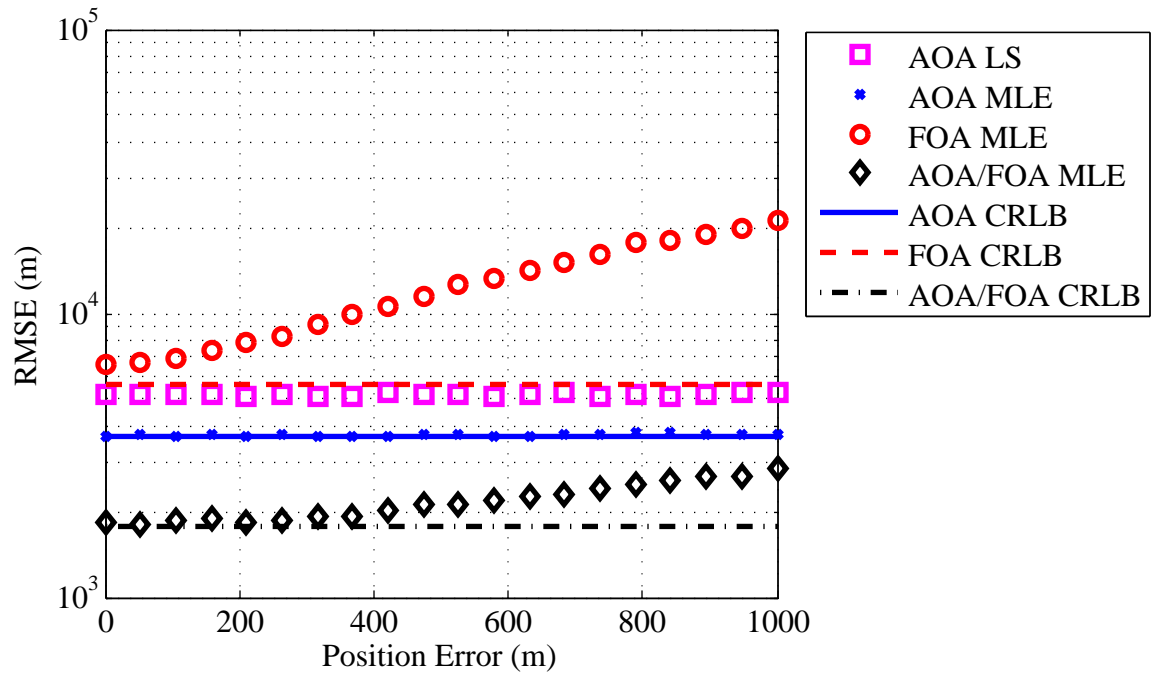
Figure 4.28: Position knowledge error variation with the burst emitter.
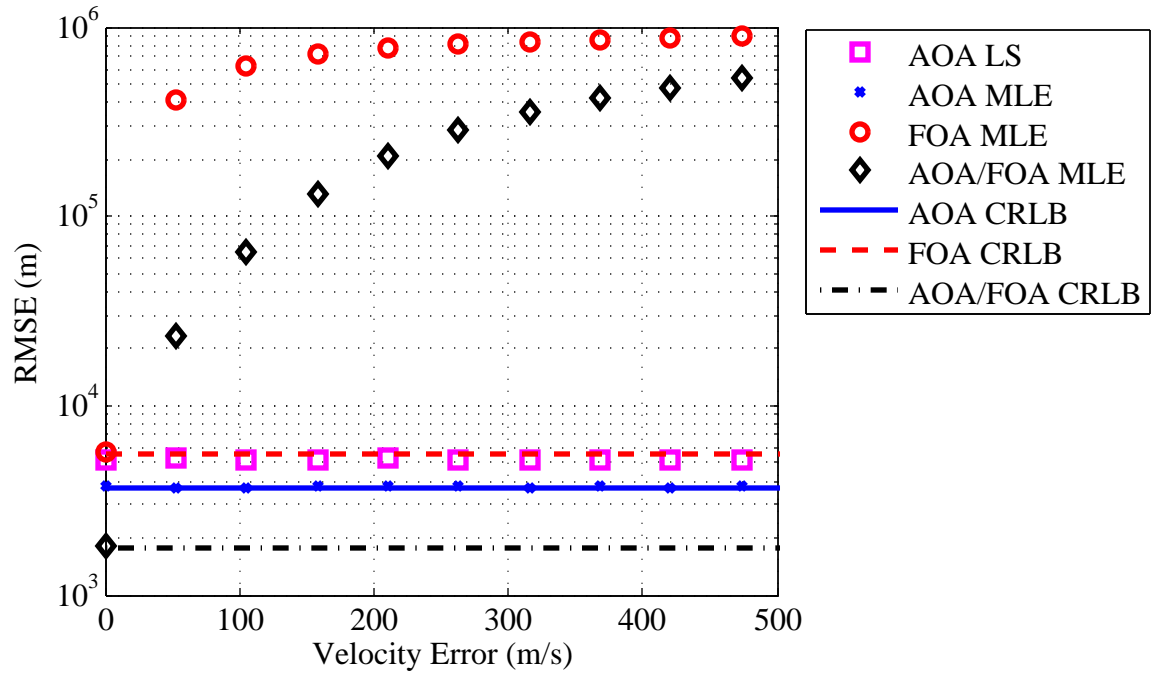
Figure 4.29: Velocity knowledge error variation with the burst emitter.

4.2.3 *Continuous Communications Emitter Sensitivity Analysis.*

Simulation results of the sensitivity analysis with the continuous communications emitter are reported in Figures 4.30 through 4.37. The parameter sensitivities observed with the continuous communications emitter are similar to the spinning radar and burst communications emitters. The AOA/FOA MLE geolocation algorithm consistently has a lower RMSE than the other 3 geolocation algorithms with the exception of high velocity knowledge errors.

Figure 4.30: Orbital pass variation with the continuous emitter.

Figure 4.31: Number of collects variation with the continuous emitter.

Figure 4.32: Number of samples per collect variation with the continuous emitter.

Figure 4.33: SNR at the first signal collect variation with the continuous emitter.

Figure 4.34: Frequency knowledge error variation with the continuous emitter.

Figure 4.35: Attitude knowledge error variation with the continuous emitter.
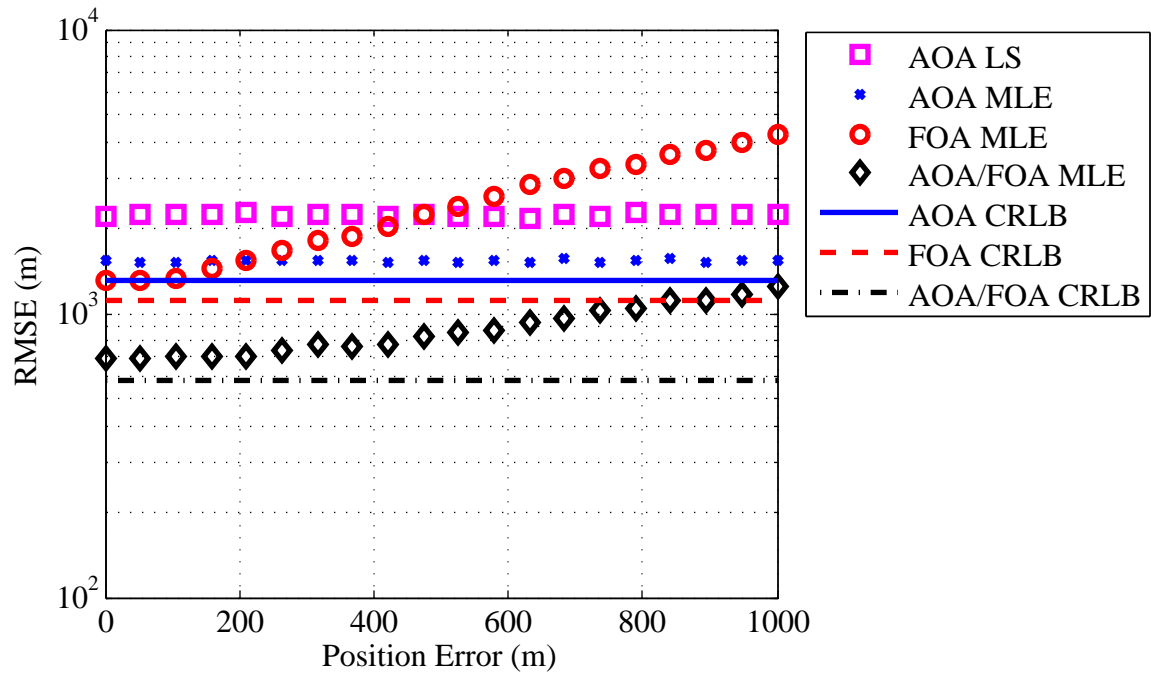

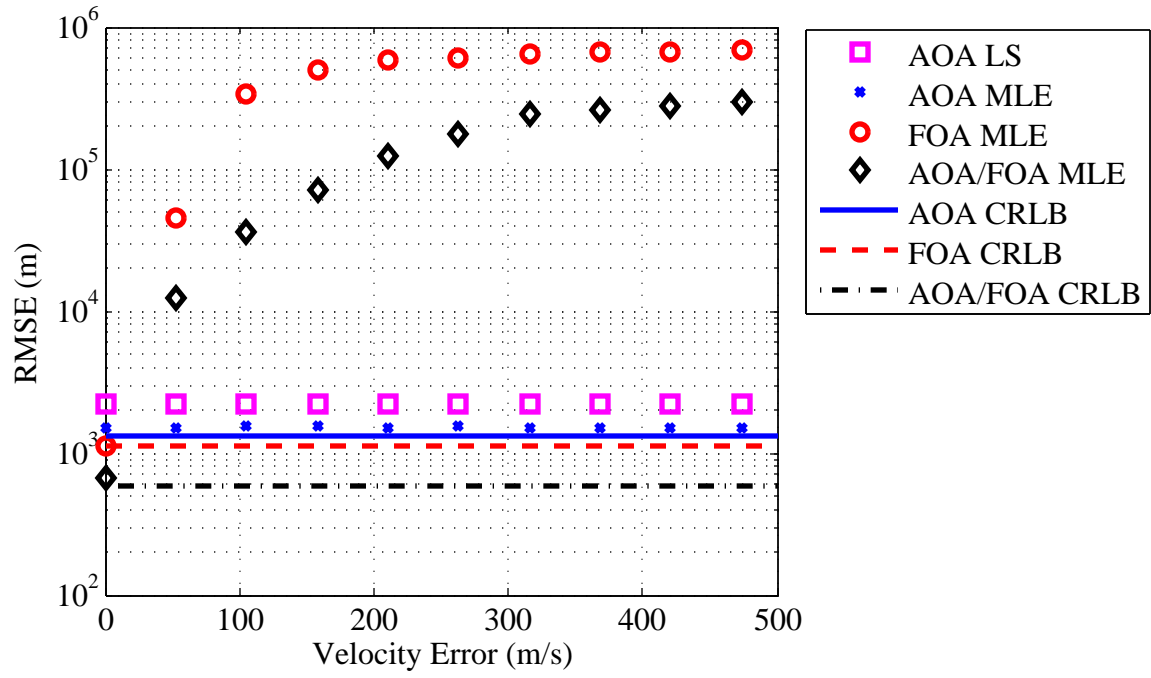Figure 4.36: Position knowledge error variation with the continuous emitter.

96

Figure 4.37: Velocity knowledge error variation with the continuous emitter.

4.2.4 Geolocation Accuracy Comparison of Emitter Types.

Since the AOA/FOA MLE geolocation algorithm has been shown to consistently have the lowest RMSE of the 4 geolocation algorithms, the performance of the AOA/FOA MLE for the 3 emitter types is compared in Figures 4.38 through 4.45.
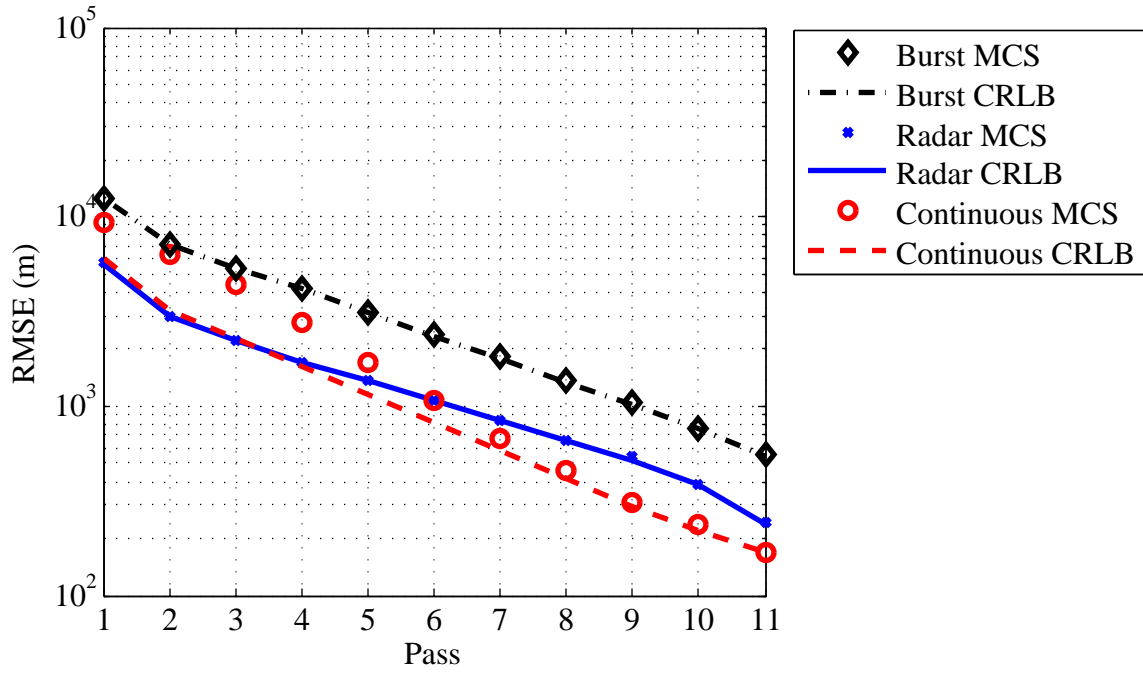
Figure 4.38: AOA/FOA MLE emitter comparison for orbital pass variation.
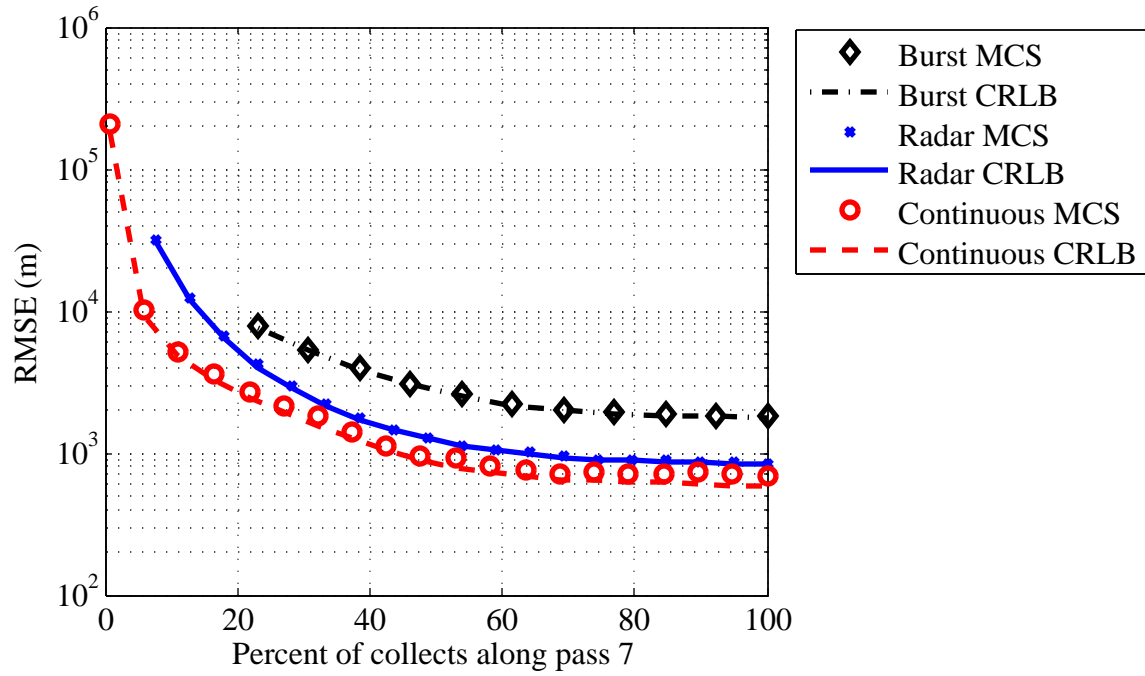
Figure 4.39: AOA/FOA MLE emitter comparison for the percent of collects along pass 7.
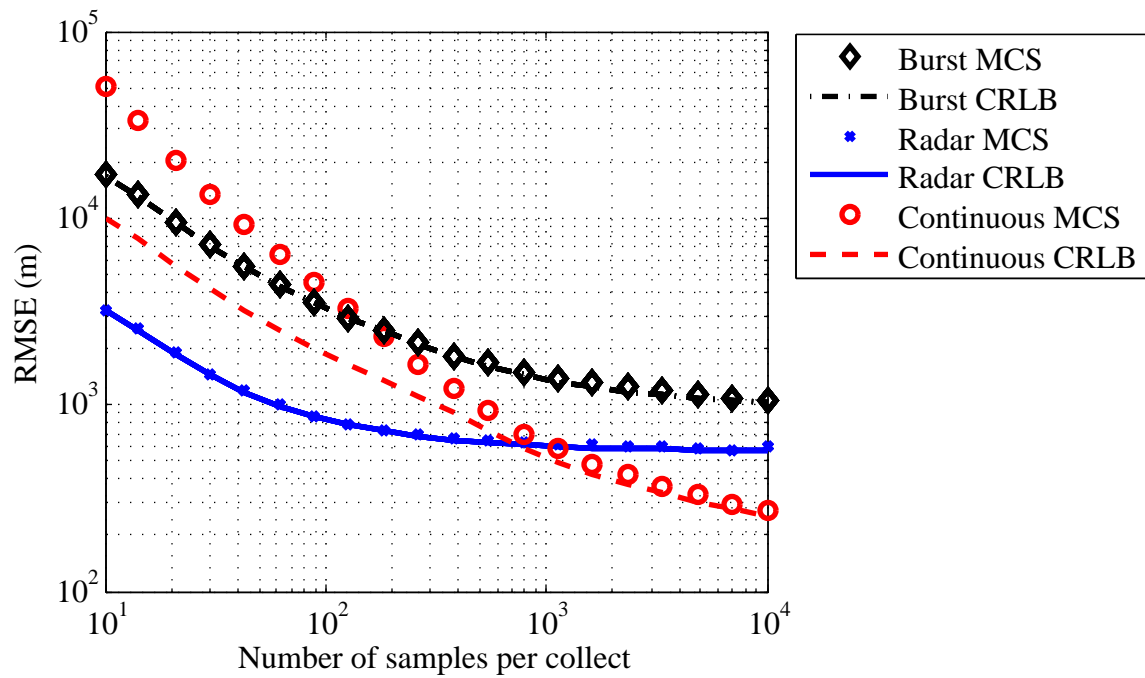

Figure 4.40: AOA/FOA MLE emitter comparison for samples per collect variation.
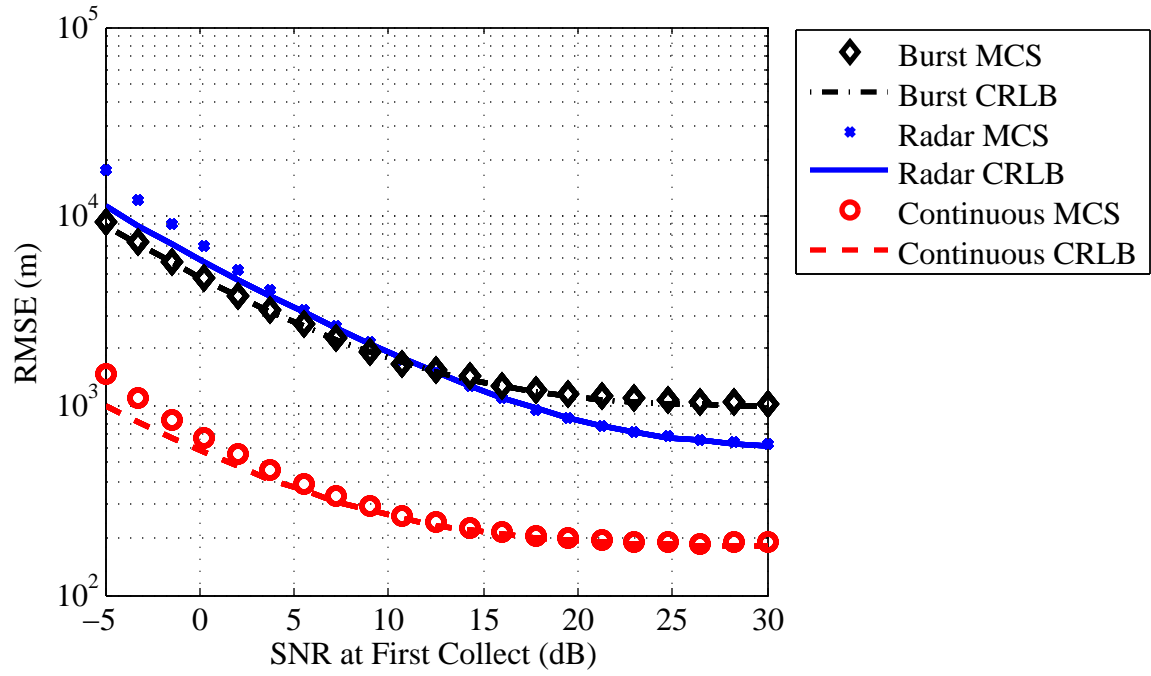
Figure 4.41: AOA/FOA MLE emitter comparison for SNR at first collect variation.
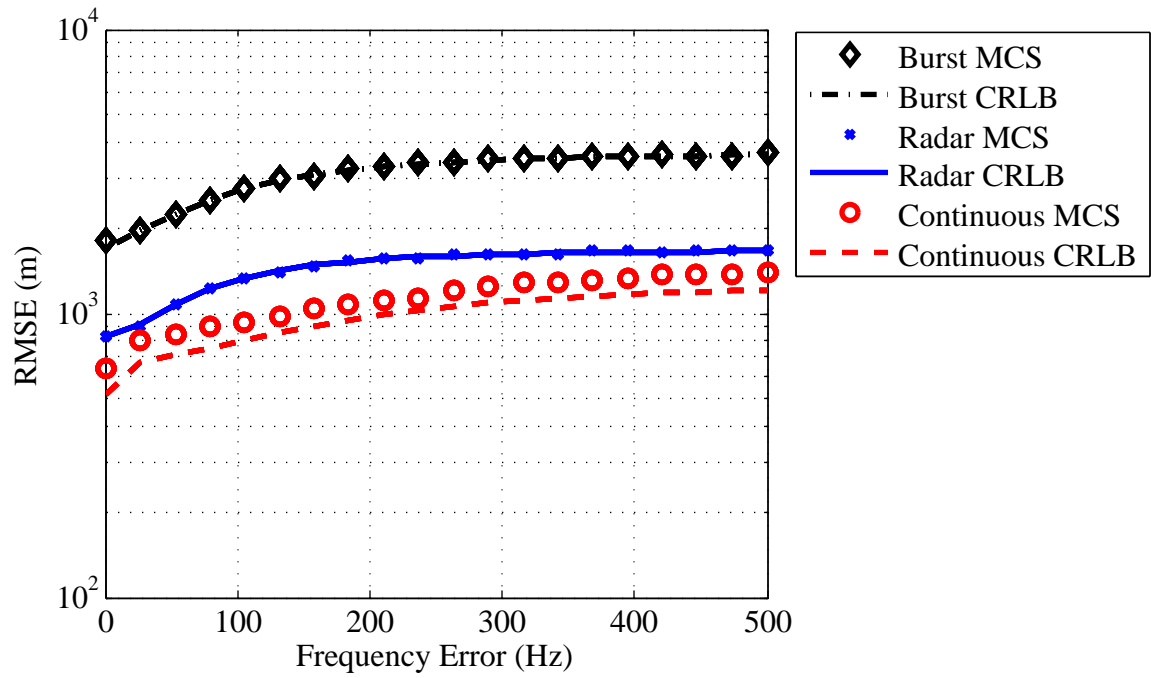

Figure 4.42: AOA/FOA MLE emitter comparison for frequency knowledge error variation.
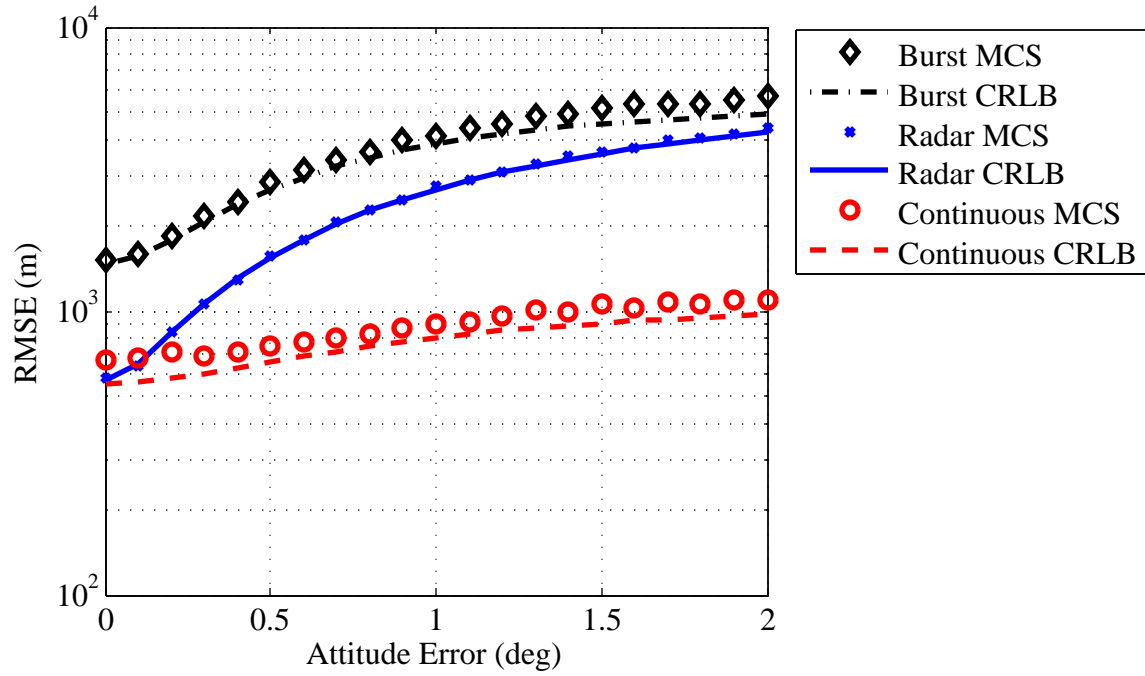
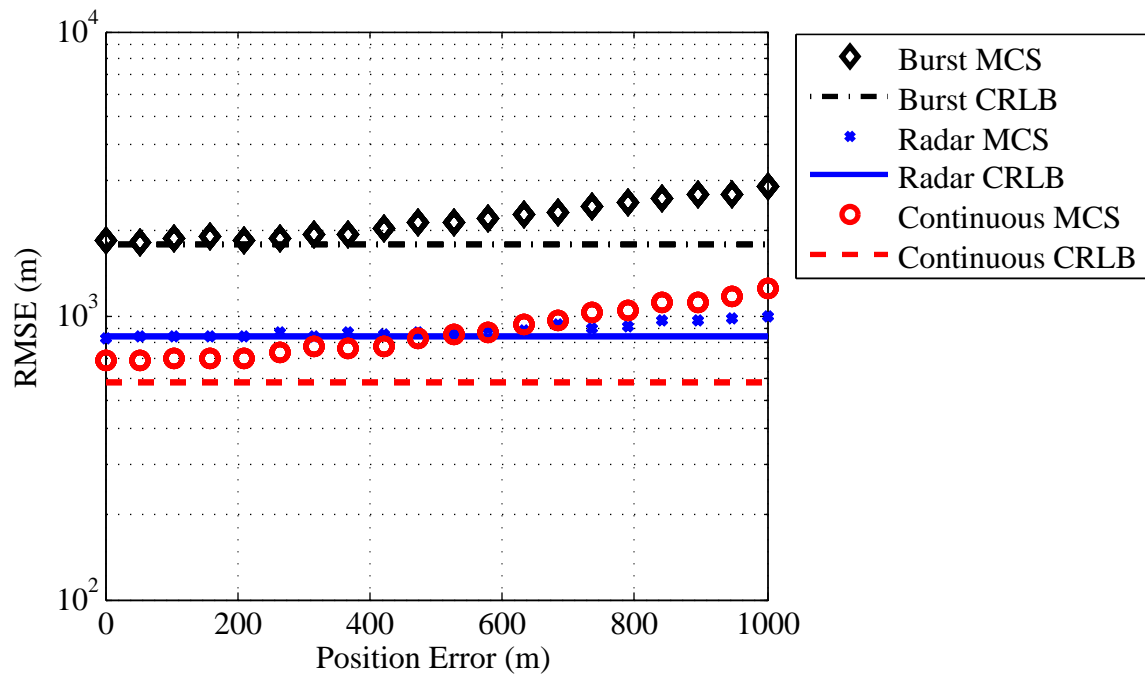Figure 4.43: AOA/FOA MLE emitter comparison for attitude knowledge error variation.

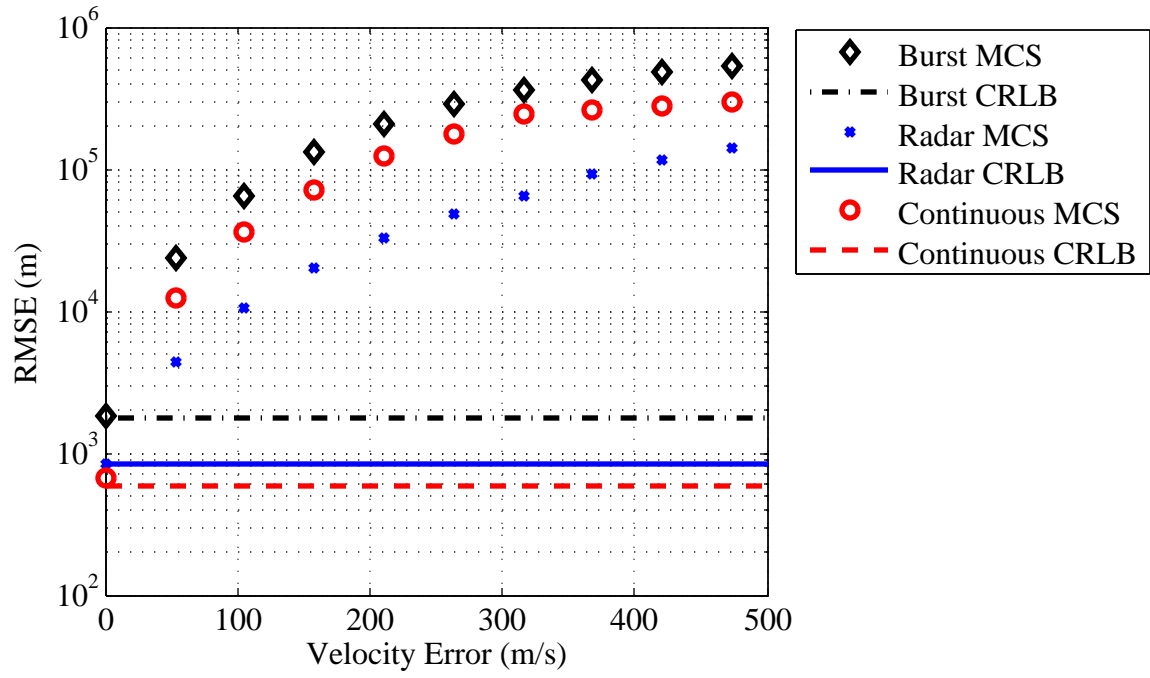Figure 4.44: AOA/FOA MLE emitter comparison for position knowledge error variation.

Figure 4.45: AOA/FOA MLE emitter comparison for velocity knowledge error variation.

V. Conclusion

This thesis presented four geolocation methods (LS, AOA, FOA, and AOA/FOA) to estimate the position of a stationary RF emitter from AOA and/or FOA measurements at a single moving receiver platform. A single emitter with no co-channel interference was assumed to simplify the analysis. The MUSIC algorithm was used for AOA measurements and the frequency MLE was used for FOA measurements. The analysis scenario considered consisted of a single 6U CubeSat receiver platform in LEO receiving RF signals from a terrestrial emitter. A simulation framework was developed to validate the statistical performance of the geolocation algorithms against the respective CRLBs and to conduct a system parameter sensitivity analysis.

5.1 Overall Research Conclusions

From the system parameter sensitivity analysis results reported in Chapter IV, the AOA/FOA MLE geolocation algorithm consistently has the lowest RMSE of the four geolocation algorithms analyzed in this thesis. The increased performance of the AOA/FOA algorithm is attributed to the greater number of measurements available per signal collect (angles and frequency estimates) and the intersection of the AOA and FOA covariance ellipsoids. As observed in Figures 3.9 and 3.17, the AOA/FOA covariance ellipsoid is the intersection of the AOA and FOA covariance ellipsoids. If an AOA payload is present on a single moving receiver platform, the implementation cost of incorporating FOA measurements is relatively low for an increase in geolocation accuracy.

Conducting the system parameter sensitivity analysis in terms of the SNR and number of samples, rather than a specific received signal, and parameter knowledge error provides intuition on the dependence of the geolocation algorithms performance on the various system parameters. In general, the geolocation accuracy increases as the SNR, number of

collects, and number of samples per collect increase. The geolocation accuracy decreases as the amount of frequency, attitude, position, and velocity knowledge error increases. At high values of SNR and number of samples per collect, the geolocation accuracy of all four algorithms is determined by the parameter knowledge errors. At high values of attitude and frequency knowledge error, the AOA/FOA algorithm accuracy approaches the AOA or FOA accuracy due to using the individual measurement variances as weighting factors in the MLE geolocation algorithms.

5.2   Recommendations for Future Work

Incorporating multiple receiver platforms into the simulation framework would allow for the analysis of additional geolocation algorithms such as time difference of arrival, frequency difference of arrival, and direct position determination. The geolocation CRLBs and MLEs can be revised to include the position and velocity knowledge errors. Additional analysis fidelity can be added by incorporating implementation specific considerations such as: mutual coupling effects and variable gain pattern of the receiver antenna array; variable gain pattern of the transmit antenna; phase coherence and noise characteristics of the RF receivers; and characteristics of a specific RF emitter. Methods for the data association and segregation of multiple emitters was not addressed in this thesis and the co-channel interference will decrease the performance of signal parameter estimates. Consideration of a moving emitter encourages time varying, target tracking, and motion analysis. Incorporation of a surface of the Earth constraint with terrain data is also recommended for future research.

Bibliography

[1] L. R. Paradowski, "Microwave emitter position location: present and future," in *12th International Conference on Microwaves and Radar*, Krakow, Poland, 20-22 May 1998, vol. 4, pp. 97–116.

[2] R. G. Stansfield, "Statistical theory of D.F. fixing," *Journal of the Institution of Electrical Engineers - Part IIIA: Radiocommunication*, vol. 94, no. 15, pp. 762–770, Apr. 1947.

[3] D. J. Torrieri, "Statistical theory of passive location systems," *IEEE Transactions on Aerospace and Electronic Systems*, vol. AES-20, no. 2, pp. 183–198, Mar. 1984.

[4] A. J. Weiss, "Direct position determination of narrowband radio frequency transmitters," *IEEE Signal Processing Letters*, vol. 11, no. 5, pp. 513–516, 2004.

[5] D. J. Nelson and J. B. McMahon, "Target location from the estimated instantaneous received frequency," in *Proceedings of SPIE Airborne Intelligence, Surveillance, Reconnaissance (ISR) Systems and Applications VIII*, Jul. 2011, vol. 8020, pp. 80200Q1–80200Q8.

[6] R. Hevner et al., "An advanced standard for cubesats," in *25th Annual AIAA/USU Conference on Small Satellites*, Logan, UT, Aug. 2011, pp. 1–12.

[7] M. Tandy (2010, Feb. 18), *ECEF ENU Longitude Latitude relationships*, [Online]. Available: http://commons.wikimedia.org/wiki/File: ECEF_ENU_Longitude_Latitude_relationships.svg.

[8] "Department of defense world geodetic system 1984," Tech. Rep. 8350.2 3rd Ed., National Imagery and Mapping Agency, Jan. 2000. Available: http://earth-info.nga.mil/GandG/publications/tr8350.2/tr8350_2.html.

[9] J. Foutz et al., *Narrowband Direction of Arrival Estimation for Antenna Arrays*, Synthesis Lectures on Antennas. Morgan and Claypool, 2008.

[10] J. R. Wertz et al., Ed., *Space Mission Engineering: The New SMAD*, Hawthorne, CA: Microcosm Press, 2011.

[11] B. Sklar, *Digital Communications: Fundamentals and Applications*, 2nd ed. Upper Saddle River, NJ: Prentice Hall PTR, 2001.

[12] C. P. Mathews and M. D. Zoltowski, "Eigenstructure techniques for 2-D angle estimation with uniform circular arrays," *IEEE Transactions on Signal Processing*, vol. 42, no. 9, pp. 2395–2407, Sep. 1994.

[13] C. P. Mathews and M. D. Zoltowski, "Signal subspace techniques for source localization with circular sensor arrays," Tech. Rep. TR-EE 94-03, Dept. Elect. and Comput. Eng., Purdue University, West Lafayette, IN, Jan. 1994. Available: http://docs.lib.purdue.edu/ecetr/172/.

[14] Y. Albagory and A. Ashour, "MUSIC 2D-DOA estimation using split vertical linear and circular arrays," *International Journal of Computer Network and Information Security*, vol. 5, no. 8, pp. 12–18, Jun. 2013.

[15] X. Lan et al., "A novel DOA estimation algorithm using array rotation technique," *Future Internet*, vol. 6, no. 1, pp. 155–170, Mar. 2014.

[16] J. Xie et al., "2D DOA estimation with sparse uniform circular arrays in the presence of mutual coupling," *EURASIP Journal on Advances in Signal Processing*, vol. 1, no. 127, pp. 1–18, Dec. 2011.

[17] Y. Wu and H. C. So, "Simple and accurate two-dimensional angle estimation for a single source with uniform circular array," *IEEE Antennas and Wireless Propagation Letters*, vol. 7, pp. 78–80, Apr. 2008.

[18] P. Tan et al., "Study of 2D DOA estimation for uniform circular array in wireless location system," *International Journal of Computer Network and Information Security*, vol. 2, no. 2, pp. 54–60, Dec. 2010.

[19] R. O. Schmidt, "Multiple emitter location and signal parameter estimation," *IEEE Transactions on Antennas and Propagation*, vol. 34, no. 3, pp. 276–280, Mar. 1986.

[20] Z. I. Khan et al., "Analysis of performance for multiple signal classification (MUSIC) in estimating direction of arrival," in *IEEE International RF and Microwave Conference Proceedings*, Dec. 2008, pp. 524–529.

[21] G. Strang, *Linear Algebra and Its Applications*, 4th ed. Belmont, CA: Thomson Brooks/Cole, 2006.

[22] E. Tuncer and B. Friedlander, Eds., *Classical and Modern Direction-of-Arrival Estimation*, Burlington, MA: Elsevier, 2009.

[23] P. Stoica et al., "The stochastic CRB for array processing: a textbook derivation," *IEEE Signal Processing Letters*, vol. 8, no. 5, pp. 148–150, May 2001.

[24] L. Burchett et al., "Angle of arrival geolocation using non-linear optimization," in *Proceedings of IEEE International Geoscience and Remote Sensing Symposium*, Munich, Germany, Jul. 2012, pp. 4533–4536.

[25] J. P. Basel, "Analysis of geolocation approaches using satellites," M.S. thesis, Air Force Institute of Technology, Wright-Patterson AFB, OH, Mar. 2014.

[26] A. J. Small, "Radio frequency emitter geolocation using cubesats," M.S. thesis, Air Force Institute of Technology, Wright-Patterson AFB, OH, Mar. 2014.

[27] S. D. Hartzell, "Non-linear optimization applied to angle-of-arrival satellite-based geolocation," M.S. thesis, Air Force Institute of Technology, Wright-Patterson AFB, OH, Mar. 2014.

[28] S. M. Kay, *Fundamentals of Statistical Signal Processing: Estimation Theory*, Upper Saddle River, NJ: Prentice Hall PTR, 1993.

[29] M. Fowler (2014, Jan. 29), *EECE 522 Estimation Theory Lecture Notes*, [Online]. Available: http://www.ws.binghamton.edu/fowler/fowler%20personal%20page/EE522.htm.

[30] D. C. Rife and R. R. Boorstyn, "Single tone parameter estimation from discrete-time observations," *IEEE Transactions on Information Theory*, vol. 20, no. 5, pp. 591–598, Sep. 1974.

[31] P. Stoica and R. Moses, *Spectral Analysis of Signals*, Upper Saddle River, NJ: Prentice Hall, 2005.

[32] L. R. Paradowski, "Uncertainty ellipses and their application to interval estimation of emitter position," *IEEE Transactions on Aerospace and Electronic Systems*, vol. 33, no. 1, pp. 126–133, Jan. 1997.

[33] S. Miller and D. Childers, *Probability and Random Processes: With Applications to Signal Processing and Communications*, 2nd ed. Waltham, MA: Academic Press, 2012.

[34] A. Noureldin et al., *Fundamentals of Inertial Navigation, Satellite-based Positioning and their Integration*, Springer, 2013.

[35] A. Amar and A.J. Weiss, "Localization of narrowband radio emitters based on doppler frequency shifts," *IEEE Transactions on Signal Processing*, vol. 56, no. 11, pp. 5500–5508, Nov. 2008.

[36] M. L. Fowler, "Analysis of single-platform passive emitter location with terrain data," *IEEE Transactions on Aerospace and Electronic Systems*, vol. 37, no. 2, pp. 495–507, Apr. 2001.

[37] K. Becker, "An efficient method of passive emitter location," *IEEE Transactions on Aerospace and Electronic Systems*, vol. 28, no. 4, pp. 1091–1104, Oct. 1992.

[38] K. Becker, "Three-dimensional target motion analysis using angle and frequency measurements," *IEEE Transactions on Aerospace and Electronic Systems*, vol. 41, no. 1, pp. 284–301, Jan. 2005.

[39] M. Oispuu and M. Schikora, "Multiple emitter localization using a realistic airborne array sensor," in *Proceedings of the 14th International Conference on Information Fusion*, Chicago, IL, Jul. 2011, pp. 1–8.

[40] B. W. Parkinson and J. J. Spilker, Eds., *Global Positioning System: Theory and Applications*, vol. I, Washington DC: American Institute of Aeronautics and Astronautics, 1996.

[41] V. Clarkson, "Efficient single frequency estimators," in *The International Symposium on Signal Processing and its Applications*, 1992.

REPORT DOCUMENTATION PAGE

1. REPORT DATE *(DD–MM–YYYY)*	2. REPORT TYPE	3. DATES COVERED *(From — To)*
26–03–2015	Master's Thesis	Sep 2013–Mar 2015

4. TITLE AND SUBTITLE

Single Platform Geolocation of Radio Frequency Emitters

5a. CONTRACT NUMBER

5b. GRANT NUMBER

5c. PROGRAM ELEMENT NUMBER

6. AUTHOR(S)

Bailey, Eric J., Captain, USAF

5d. PROJECT NUMBER

N/A

5e. TASK NUMBER

5f. WORK UNIT NUMBER

7. PERFORMING ORGANIZATION NAME(S) AND ADDRESS(ES)

Air Force Institute of Technology
Graduate School of Engineering and Management (AFIT/EN)
2950 Hobson Way
WPAFB, OH 45433-7765

8. PERFORMING ORGANIZATION REPORT NUMBER

AFIT-ENG-MS-15-M-028

9. SPONSORING / MONITORING AGENCY NAME(S) AND ADDRESS(ES)

Air Force Research Laboratory, Space Vehicles Directorate
Attn: Dr. Alan Lovell, AFRL/RVSV
3550 Aberdeen Ave SE
Kirtland AFB, NM 87117-5776
505-853-4132 (DSN: 263-4132) thomas.lovell@kirtland.af.mil

10. SPONSOR/MONITOR'S ACRONYM(S)

AFRL/RVSV

11. SPONSOR/MONITOR'S REPORT NUMBER(S)

12. DISTRIBUTION / AVAILABILITY STATEMENT

DISTRIBUTION STATEMENT A:
APPROVED FOR PUBLIC RELEASE; DISTRIBUTION UNLIMITED

13. SUPPLEMENTARY NOTES

This work is declared a work of the U.S. Government and is not subject to copyright protection in the United States.

14. ABSTRACT

The focus of this research is on single platform geolocation methods where the position of a single stationary radio frequency emitter is estimated from multiple simulated angle and frequency of arrival measurements taken from a single moving receiver platform. The analysis scenario considered consists of a single 6U CubeSat in low earth orbit receiving radio frequency signals from a stationary emitter located on the surface of the Earth. A multiple element receive antenna array and the multiple signal classification algorithm are used to estimate the angles of arrival of an impinging signal. The maximum likelihood estimator is used to estimate the frequency of arrival of the received signal. Four geolocation algorithms are developed and the accuracy performance is compared to the Cramer-Rao lower bounds through Monte Carlo simulations. Results from a system parameter sensitivity analysis show the combined angle and frequency of arrival geolocation maximum likelihood estimator consistently outperforms the other three geolocation algorithms.

15. SUBJECT TERMS

Geolocation, CubeSat, Angle of Arrival, Frequency of Arrival, Maximum Likelihood Estimation

16. SECURITY CLASSIFICATION OF:			17. LIMITATION OF ABSTRACT	18. NUMBER OF PAGES	19a. NAME OF RESPONSIBLE PERSON
a. REPORT	b. ABSTRACT	c. THIS PAGE			Richard Martin (ENG)
U	U	U	UU	125	19b. TELEPHONE NUMBER *(include area code)* (937) 255-3636 x4625 richard.martin@afit.edu